Alma Mater Studiorum – Università di Bologna

DOTTORATO DI RICERCA IN

CHIMICA

Ciclo XXIX

Settore Concorsuale di afferenza: 03/B1

Settore Scientifico disciplinare: CHIM/03

"Functionalized Calcium Phosphates with anti-resorptive, anti-angiogenetic and anti-bacteric properties"

Presentata da: Lucia Forte

Coordinatore Dottorato	**Relatore**
Chiar.mo Prof. Aldo Roda	**Chiar.ma Prof.ssa Adriana Bigi**
	Correlatore
	Dott.ssa Elisa Boanini

Esame finale anno 2017

Contents

SUMMARY

The increased life expectancy in developed countries has led to a considerable increase in the number of pathologies related to the skeletal system with consequent increase in the demand for materials able to repair and / or replace damaged tissues. Due to their similarity with the mineral phase of bone tissue, calcium phosphates are characterized by excellent biocompatibility and bioactivity and consequently are widely used for the preparation of biomaterials able to repair / replace the bone tissue. The response of the biological tissue to synthetic material can be further improved through the functionalization of calcium phosphates with ions and biologically active molecules.

This PhD thesis was addressed to study the interaction between calcium phosphates and several functionalizing agents, in order to develop new materials with enhanced biological performance, suitable for biomedical applications in the orthopaedic field. The functionalizing molecules taken into consideration include several bisphosphonates, namely risedronate, zoledronate, and alendronate, and a molecule from the large group of flavonoids, quercetin (3, 3’, 4’, 5, 7-pentahydroxy-flavone). Functionalization of several calcium phosphates, namely hydroxyapatite, octacalcium phosphate and anhydrous dicalcium phosphate (monetite), was performed following different strategies: direct synthesis and adsorption from solution. Characterization of the obtained products allowed to verify the amount of the functionalizing agent incorporated into the calcium phosphate, as well as the possible morphological and structural modifications induced on the inorganic phase. In particular, the study carried out on risedronate adsorption on four hydroxyapatites with different composition provided useful information on the influence of the characteristics of the supports on the mechanisms of adsorption and release of the bisphosphonate. The materials developed during these three years include also octacalcium phosphate at different content of alendronate, as well as octacalcium phosphate at different content of zoledronate, and coatings of mixed composition, octacalcium phosphate – calcium alendronate, which were deposited on titanium substrates using Maple Assisted Pulsed Laser Evaporation.

Quercetin functionalized hydroxyapatite was obtained thanks to a modified method of synthesis, which implies phase transformation from monetite, as well as through adsorption from solution. Adsorption from solution was successfully applied also to load the flavonoid on alendronate functionalized hydroxyapatite, monetite and monetite with a partial substitution of strontium to calcium ion. The results of the radical

scavenging activity test indicated that quercetin maintained its anti-oxidant properties also when incorporated on the calcium phosphates.

Finally polydopamine coating of octacalcium phosphate and α-tricalcium phosphate was utilized to induce reduction of silver ions and decorate the calcium phosphates with silver nanoparticles, thus obtaining new composite materials with antimicrobial properties.

Most of the materials developed in this PhD thesis have been submitted to biological in vitro tests, which generally indicated that the peculiar characteristics of the functionalized agents are maintained when incorporated into the calcium phosphates, so that they display both the beneficial properties (anti-osteoporotic and/or anti-inflammatory and/or anti-tumoral and/or anti-microbic) of the functionalizing agent(s) and the excellent bioactivity of the inorganic phase.

1. Introduction

1.1 Biomimetic Materials

Biomimetics is the application of biological methods and systems, found in Nature, to the study and design of engineering systems and modern technology. Since ancient times, Nature has offered a lot of different materials to make tools and weapons but specially, Nature has provided ideas. Looking at how Nature solved problems, inventors were able to answer several issues related to everyday life. In modern terms, this mankind's propensity to mimic Nature can be called "Biomimetic Science" that is a multidisciplinary field encompassing various research areas including: materials science, materials engineering, biology, biochemistry and medicinal chemistry.

Mimic biological materials is a powerful approach for the synthesis of advanced materials with complex shape, hierarchical organization and controlled size, shape and polymorphism under ambient conditions in aqueous environments. In particular the use of a hierarchical structure, a special arrangement of structural elements, allows to modulate the mechanical and structural properties that can change from one length scale to another. Bone, nacre, tooth enamel, antler, sea sponge spicules, diatoms, are a few examples of materials employing inferior components and structural hierarchy to achieve remarkable collections of properties and functionalities.

This wide variety of materials, which constitute the exo and endo skeletons, as well as other functional materials, are built up by Nature through a process called *biomineralization.*

In the study of these materials, the main aim is not to simply emulate a particular biological architecture or system, but to abstract the guiding principles and ideas in order to exploit them for the preparation of new synthetic materials and devices. These ideas promped a rapidly developing research field, which can be summarized as bio-inspired or biomimetic materials chemistry.

At the nanometer scale, *biomineralization* implies the molecular building of specific and self-assembled supramolecular organic systems (micelles, vesicles, *etc.*) which act as a previously arranged environment to control the formation of finely divided inorganic materials, of around 1–100 nm in size. The production of consolidated biominerals, such as bones and teeth, also requires the presence of previously arranged organic structures, at a higher length scale (micrometers).

In this context, the controlled synthesis of inorganic materials with specific morphology is an important aspect in the development of new materials for application in many fields such as catalysis, electronics, nanocomposites, and of course biomaterials.

1.2 Calcium Phosphates for Hard Tissue Repair

The past half century has seen explosive growth in the use of medical implants for hard tissue repair. Orthopedic, oral and maxillofacial surgeons are only few examples of medical specialists treating millions of patients each year by implanting devices.

In addition, an aging population and increasing life expectancy in the developed world mean that our tissues and organs are pressed into service longer than they may be able to independently withstand. In this context, calcium phosphates are the best candidates to develop new materials thanks to their bioactive and biocompatible properties. In particular hydroxyapatite (HA), which resembles the main mineral constituent of human hard tissues, has been successfully used clinically for repair of bone defects and augmentation of osseous tissues.

Besides HA, tricalcium phosphates (TCP) (in two different crystallographic phases, α-TCP and β-TCP), octacalcium phosphates (OCP), and amorphous calcium phosphates (ACP) are also used. On the other hand, calcium phosphates alone have poor mechanical properties, furthermore they hardly fit into a geometrically complex defect. To enhance their mechanical properties, calcium phosphates are paired with polymers like poly(methyl-methacrylate) (PMMA)[1], poly(lactic acid) (PLA), poly(glycolic acid) (PGA), and their copolymers [2,3]; as well as natural polymers, such as collagen, fibrin and chitosan.

Moreover, to improve the bioactivity, synthetic drugs and biomolecules can be adsorbed or covalently attached to an implant surfaces, or embedded inside for a slow release after the implantation.

Typically osteogenic cells and/or osteoinductive growth factors are coupled with bioactive scaffolds [4, 5]. Some studies have investigated the bone forming capacities of growth factors loaded synthetic bone substitutes. In terms of growth factors, most research has focused on the use of the bone morphogenetic proteins (BMPs) [6]. They are signaling molecules which can induce *de novo* bone formation at orthotopic and heterotropic sites [7]. Current examination of alternatives to grafting techniques suggests three possible new approaches to inducing new bone formation: implantation of certain cytokines such as BMPs in combination with appropriate delivery systems at the target site [8]; transduction of genes encoding cytokines with osteogenic capacity into cells at repair sites; and transplantation of cultured osteogenic cells derived from host bone marrow [9].

In literature a wide range of molecules are reported that are used to functionalize calcium phosphates like anticancer drugs [10]; insulin [11]; analgesic drugs [12], and antibiotics [13].

Unfortunately, even with all this kind of molecules and strategies, we still really know very little about the mechanism used by organisms to form their superior materials. In addition, all therapies which are based on complex biomolecules are costly and difficult to regulate. Better biomaterials for bone substitution and are not still developed, and this fact makes this research field exciting and still in progress.

1.2.1 Bone tissue

Skeleton, and consequently bone, has a primary function which is that of structural support of the mammalian body and constantly remodeling in response to the applied stresses.

In addition to this structural function, bone is also important for internal organ protection, muscle support and regulation of the calcium ions concentration through the ongoing resorption and formation of new mineral, regulated by two kinds of cells: osteoblast and osteoclast.

Bone is a dynamic, highly vascularized tissue that is formed from a composite of 70% mineral (mostly nanoscale HA crystals) and 30% organics (including collagen, glycoproteins, proteoglycans, and sialoproteins) by dry weight [14].

The mineral and the organic part are arranged in a complex architecture with several hierarchical levels, from nanometer to macroscopic scale, which provides bone unique structure and properties.

The basic building block of bone, for subsequent higher order architectures, is the mineralized collagen fibril. It is composed of the fibrous protein collagen which constitutes the main component of a three-dimensional matrix into which, and in some cases onto which, the mineral forms. The mineral in this family of materials is dahllite, also known as carbonated apatite (Ca_5 (PO_4, CO_3)$_3$ (OH)) [15]. The third major component is water [16].

Table1 Organic components of bone [15]

NAME	FUNCTION IN BONE MINERALIZATION
Collagen	Structural protein found in many tissues.
Bone sialoprotein (BSP), Osteonectin (ON), Chondroitin sulfate (ChS) and Keratan sulfate	Acid protein with poly(glutamic acid) run and RGD binds calcium glycoproteins that may either nucleate or block HA mineralization large molecular weight, sulfated glycosaminoglycans that are found in cartilage and bone tissues.
Osteocalcin(OC), Biglycan and Decorin	Inhibits bone formation; does not appear to affect HA mineralization proteoglycans that bind to type I collagen and are involved in assembly of bone matrix; Decorin specifically interacts with d and e bands of collagen; Biglycans consist of leucine-rich repeats and two glycosaminoglycans; these protein also interact with thrombospondin and fibronectin.
Thrombospondin and Fibronectin	Matrix glycoproteinsthat bind to integrins and ECM components (collagen, fibrin, etc.)

The first level of hierarchy consists of the molecular components: water, HA, collagen, and other proteins. The crystals of HA are plate-shaped and are among the smallest known biological crystals (30-50 nm long, 20-25 nm wide, and 1.5-4 nm thick). Non-collagenous proteins (NCPs) are also present but make up 10% or less of the total protein content in the bone matrix. The specific functions of the NCPs are still not completely understood, but some studies report that they influence crystal nucleation and growth and they also play roles in cell signaling and ion homeostasis [17].

The second level is formed by the mineralization of collagen fibrils. This platelet-reinforced fibril composite is described as containing parallel plate-like HA crystals [16] with their *c*-axis aligned with the long axis of the fibril [18].

The third level of hierarchy is composed of arrays of these mineralized collagen fibrils. These fibrils are rarely found isolated but rather almost always associated as bundles or in other arrangements, often aligned along their long axis.

The fourth level is the patterns of arrays that are formed. These include parallel arrays, woven arrangements, plywoodlike structures, and radial arrays.

Cylindrical structures called osteons make up the fifth level. Osteons are formed by a significant cellular activity and remodeling; osteoclasts resorb bone and form a tunnel, and osteoblasts subsequently lay down lamellae in stacked layers until only a small channel (Haversian canal) is left behind. These channels serve as a conduit for nerves and blood supply to the bone cells. The metabolic substances can be transported by the intercommunicating systems of canaliculi, lacunae, and Volkman's canals, which are connected with the marrow cavity. The various interconnecting systems are filled with body fluids and their volume can be as high as 19%.

The sixth level of bone organization is the classification of osseous tissue as either spongy (trabecular or cancellous) or compact (cortical). Cancellous bone (also called trabecular or spongy bone) is extremely porous (75-95% porosity), providing space for marrow and blood vessels, but has much lower compressive strength. Cortical bone is the dense outer layer (5-10% porosity) that allows most of the support functions of bone. The seventh level is simply the whole bone on the macroscopic scale, incorporating all of the lower levels of hierarchy.

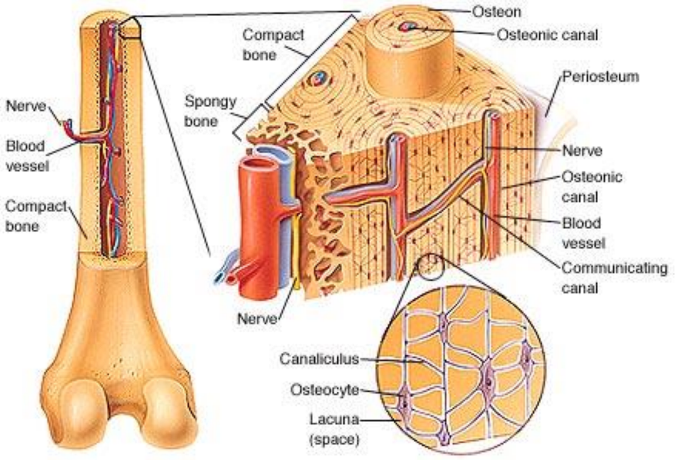

Figure1 Structure of the bone, on the right a focus on osteon structure (www.mhhe.com)

The inorganic component is a nanocrystalline solid with apatite structure and the chemical composition of a carbonated, basic calcium phosphate, hence it can be termed a carbonate-hydroxy-apatite. The benefits of the inorganic component are toughness and the ability to withstand pressure.

Besides the main ions Ca^{2+}, PO_4^{3-} and OH^-, the composition of biological apatites always includes CO_3^{2-} at ~4.5%, and also a series of minority ions, including Mg^{2+}, Na^+ , K^+ , Cl^- and F^- .

The apatite structure can hosts carbonate in two positions: the OH^- sub-lattice producing so-called type A carbonate apatites or the $[PO_4]^{3-}$ sub-lattice called type B apatites.

Small dimensions and low crystallinity are two distinct features of biological apatites which, combined with their non-stoichiometric composition, inner crystalline disorder and presence of carbonate ions in the crystal lattice, explain their special behavior. In fact a younger, less crystalline tissue can develop and grow faster, while storing other elements that the body needs during its growth. Biological apatites are calcium-deficient; hence their Ca/P ratio is always <1,67, the value characteristic of stoichiometric apatite.

As shown before, bone maintains a dynamic state, through a process termed remodelling due to the coordinated actions of bone resorption and synthesis, mediated by osteoclasts and osteoblasts, respectively. In any case, the activity of bone cells is highly regulated and stimulated by hormones and cytokines. Steroid hormones act on various cell types to regulate development, cell proliferation and cell differentiation.

Osteoblasts are mononuclear cells of mesenchymal origin that are responsible for formation of the osteoid, the organic portion of the bone tissue. In addition to osteoid secretion, osteoblasts are also involved in the mineralization process. These cells are believed to regulate the local calcium and phosphate concentrations to promote apatite mineralization. [19, 20]

As osteoblasts become trapped in the secreted matrix, they terminally differentiate into osteocytes [21], mature and interconnected cells which are responsible to be signaling for matrix resorption or formation in response to mechanical stress [22].

Osteoclasts remove bone tissue by a process known as “bone resorption” [23, 24]. The actin cytoskeleton of the osteoclast reorganizes into a ring known as the “sealing zone”; the cell membrane forms a “ruffled border” at the contact with the bone tissue to facilitate dissolution of the apatite mineral followed by hydrolysis of the collagen-rich organic matrix [23]. Vacuolar proton pumps cause demineralization of the bone matrix by acidification to a pH of~4.5 [24].The organic portion of the matrix is further broken down by lysosomal cysteine proteases [25] and matrix metalloproteases (MMP) [23]. Finally, the degraded extracellular materials are removed from the resorptive lacuna, shuttled into the extracellular space and ultimately into the blood [23].

1.2.2 Calcium Phosphates of biological interest

Calcium phosphates exhibit a wide range of possible applications, which span from their use as catalysts, as starting materials in the preparation of phosphatic fertilizers, as columns in chromatographic separation and as stabilizers for plastics, up to the biomedical field.

The biological interest is due to the fact that calcium phosphates are the main constituent of bone and teeth and consequently, being biocompatible and bioactive, they are widely used as biomaterials for the repair and replacement of bone tissue. The interest is not only for hydroxyapatite, which for composition and structure is often equated to biological apatite, but even for other more resorbable calcium phosphates, like amorphous calcium phosphate (ACP), α-tricalcium phosphate (α-TCP), β-tricalcium phosphate (β-TCP), octacalcium phosphate (OCP), dicalcium phosphate dihydrate (DCPD), dicalcium phosphate anhydrous (DCPA), that can be easily converted into nanocrystalline apatite [26].

Table 2 Calcium Ortophosphates

COMPOUND	*FORMULA*	*SPACE GROUP*	*Ca/P*
DCPD	$CaHPO_4*H_2O$	Monoclinic Ia	1.00
DCPA	$CaHPO_4$	Triclinic P-1	1.00
OCP	$Ca_8(HPO_4)_2(PO4)_4*5H_2O$	Triclinic P-1	1.33
α-TCP	α-$Ca_3(PO_4)_2$	Monoclinic $P2_1/a$	1.50
β-TCP	β-$Ca_3(PO_4)_2$	Rhombohedral R3Ch	1.50
HA	$Ca_{10}(PO_4)_6(OH)_2$	Hexagonal $P6_3/m$	1.67

Most calcium orthophosphates are sparingly soluble in water, but all dissolve in acids; in particular, the lower is the Ca/P ratio the more acid and soluble is the calcium phosphate phase.

Further, the presence of organic molecules can affect the crystallization process, complicating the detection of intermediate phases [27].

Hydroxyapatite (HA) is the most thermodynamically stable and less soluble phase and it is preferentially formed under neutral or basic conditions. In more acidic solutions, phases such as brushite (DCPD) and octacalcium phosphate (OCP) are often encountered.

In biological tissues, DCPD and OCP are usually detected only during pathological calcification, where the pH is often relatively low. In normal *in vivo* calcifications, these phases have not been found, suggesting the involvement of other precursors or the formation of an initial amorphous calcium phosphate phase (ACP), followed by transformation to apatite [28].

The stability of calcium phosphate (CaP) phases in contact with aqueous solutions can be understood in terms of a typical solubility phase diagram in which solubility isotherms are expressed as plots of (log *T*ca*T*p) as a function of pH (Figure 2). Here, *T*ca and *T*p are the total molar concentrations of calcium and phosphate, respectively. Figure 2 has been constructed on the assumption that the solution contains equal total molar concentrations of calcium and phosphate ions at an ionic strength of 0.1 M. The position of the curves and the singular points in Figure 2 will change if the ionic strength of the background electrolyte is varied. It can be seen that, at pH above 4.0, HA is the most stable phase, followed by TCP and OCP. At pH values lower than 4.0, DCPD is more stable than HA. The variations in solubility with pH imply that a phase exposed to acidic conditions may be covered by a surface coating consisting of a more acidic calcium phosphate phase [29].

Moreover, the kinetic factors are fundamental for determining which crystalline phases will be formed, with respect to the others in a supersaturated solution. In fact, HA formation evolves through the formation of intermediate products which are thermodynamically metastable but kinetically favoured.

The influence of pH on the formation of calcium phosphates is linked to the properties of phosphate containing solutions. Due to the triprotic equilibria in these systems, variations in pH alter the relative concentrations of the four protonated forms of phosphoric acid and thus both the chemical composition and the amount of the CaP that forms by direct precipitation. This complex equilibrium makes the control and prediction of CaP precipitation very difficult [30].

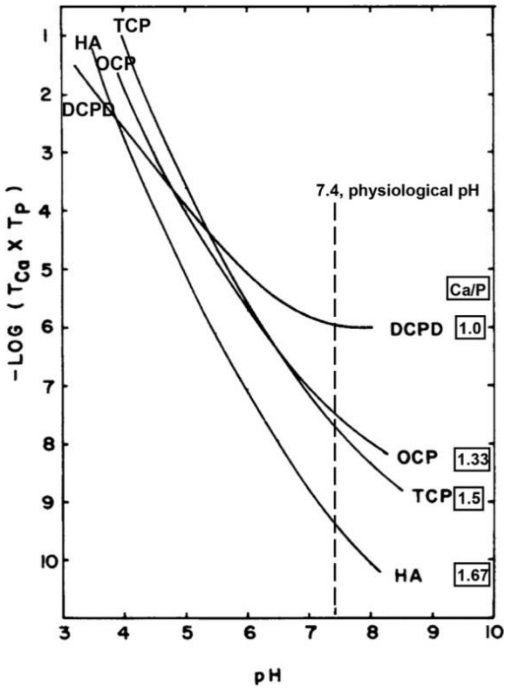

Figure2 Solubility phase diagram of various calcium phosphates and relative Ca/P ratio [31]

1.2.2.1 Hydroxyapatite

The name apatite is given to a class of inorganic compounds whose general formula can be written as $M_{10}(XO_4)_6Y_2$: where M is generally a bivalent cation like Ca^{2+}, Sr^{2+}, Ba^{2+}, Cd^{2+} o Pb^{2+}, but even monovalent (Na^+, K^+) and trivalent (Al^{3+}) cations can be hosted in the structure. The term XO_4 indicates trivalent anions like PO_4^{3-}, VO_4^{3-} o AsO_4^{3-}, even if anions with different charge (SiO_4^{4-}, CO_3^{2-} e SO_4^{2-}) can enter in the elementary cell. Finally Y is referred to a monovalent anion like F^-, Cl^-, Br^- or OH^- .

Hydroxyapatite ($Ca_{10}(PO_4)_6(OH)_2$) is the most stable and insoluble calcium phosphate (CaPs) and is the most similar to the inorganic component of bone from a chemical and structural point of view. The known crystalline forms of hydroxyapatite are two: the monoclinic one, space group $P2_1/b$, and the hexagonal one, space group $P6_3/m$; but only the hexagonal phase have a practical interest because the monoclinic form is destabilized by the presence of even small amounts of foreign ions [31].

The $P6_3/m$ space group has three kinds of vertical symmetry elements: (1) six-fold screw axes passing through the corners of the unit cells which are equivalent to a three-fold rotation axis with a superimposed two-fold screw axes; (2) three-fold rotation axes passing through $^{2}/_{3}$, $^{1}/_{3}$, 0 and $^{1}/_{3}$, $^{2}/_{3}$, 0; and (3) two fold screw axes passing through the mid points of the cell edges and its centre. There are also mirror planes perpendicular to the *c*-axis at $z = ¼$ and ¾, and numerous centres of symmetry.

The basic apatite hexagonal structure exhibits approximate lattice parameters $a = 9.43$ Å and $c = 6.88$ Å $\alpha=\beta=90°$ $\gamma= 120°$ with two formula units per cell [32]. This is the reason why a double formula is often used $[Ca_{10}(PO_4)_6X_2]$. The values often depend on the mode of preparation because of the frequent non-stoichiometry. The hydroxyapatite stoichiometry is characterised by a molar ratio Ca/P equal to 1.67.

The structure can be roughly described as an assembly of tetrahedral phosphate PO_4^{3-}, among which are placed the calcium ions in two independent crystallographic sites, crossed by parallel channels filled by OH^- ions and oriented along the crystallographic *c*-axis (Figure 3).

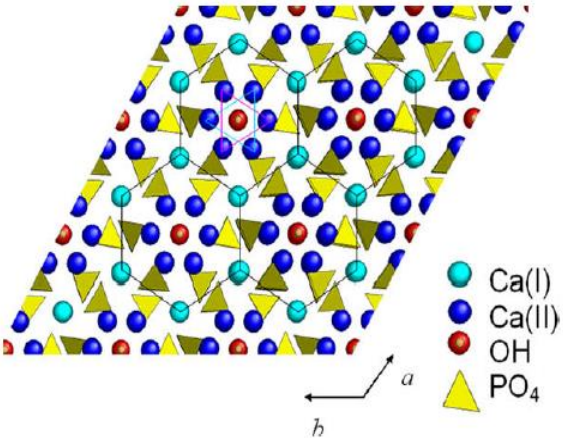

Figure 3 A view of the HA structure along the *c*-axis. Black lines connect Ca(I) columns in hexagonal networks. Cyan and magenta triangles connect staggered Ca(II) atoms lying in the same plane but at different height with respect to the *c*-axis [26].

The first crystallographic site for calcium ions is called *columnar site* and it is indicated as Ca(I). In the columns, Ca^{2+} ions, which account for two-fifths of the Ca^{2+} ions in the structure, are spaced by one-half of the c-axis parameter along the three-fold axes at $^{2}/_{3}$, $^{1}/_{3}$, 0 and $^{1}/_{3}$, $^{2}/_{3}$, 0.

The second crystallographic site for the calcium ions is called *triangular site*. The calcium ions Ca(II) form two triangles rotated by 60° from each other about the *c*-axis; the OH^- ions are located at the center of the triangles.

Among the 10 cations, the 4 Ca(I)s are tightly bonded to 6 oxygens and less strongly to the other 3 oxygens (mean Ca(I)–O distance 0.255 nm), whereas the 6 Ca(II) atoms are surrounded by 7 oxygens (mean Ca(II)–O distance 0.245 nm). Ca(I) atoms are strictly aligned in columns and any small change in the metal–oxygen interactions affects the entire lattice. However, the Ca(II) atoms belonging to consecutive layers are staggered, allowing random local misplacements without compromising the whole structure. As a consequence, cations smaller than Ca or also low concentrations of slightly larger cations are preferably accommodated in site Ca(I) where stronger interactions are present, while larger cations should be accommodated in position Ca(II), even at high concentrations.

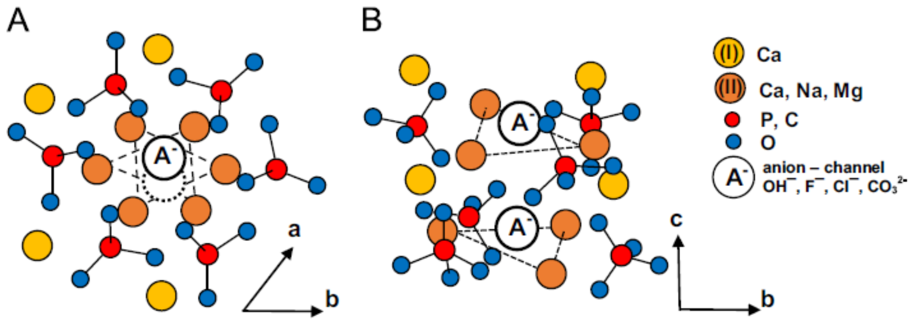

Figure 4 View of the atomic structure of hydroxyapatite as a stand-in for bioapatite. Viewed (A) down the c-axis and (B) perpendicular to the *c*-axis [38].

The literature reports a variety of syntheses of HA that, although differing in terms of the detailed conditions, essentially follow two methods. The first one consists in the stoichiometric titration of a calcium hydroxide slurry with phosphoric acid up to neutrality [33]. In the second one, the precipitation method, a solution of ammonium or sodium monohydrogen phosphate is added dropwise to a calcium solution (generally calcium nitrate or acetate) or vice versa [34,35]. Both methods yield good crystalline products when carried out at 100°C. Lower temperature provokes an increase in the amount of amorphous material and/or decrease in crystallinity. The titration method is performed in a basic environment, whereas the precipitation method often implies addition of ammonia or sodium hydroxide to maintain a basic pH (>9) during precipitation. A further factor that influences crystallinity and crystal dimensions is the reaction time: short reaction times provide nanocrystals and/or amorphous products, whereas crystal dimensions and crystallinity increase with increasing reaction time [26].

1.2.2.2 Octacalcium Phosphate

Octacalcium phosphate (OCP) has a significant biological relevance due to its role as a possible precursor during the formation of carbonated apatite in the hard tissues of vertebrates. Thus understanding the growth of OCP and its hydrolysis provides useful information for understanding the processes of mineralization in bones and teeth.

In addition, OCP has been found as a constituent in dental calculus, in pathological calcifications [36] and in a crystal of calcifying dentine together with apatite [37].

OCP crystallizes in a triclinic structure [39], space group P $\bar{1}$ and unit cell a = 19.692 Å, b = 9.523 Å, c = 6.835 Å, α = 90.15°, β = 92.54° and γ = 108.65°.

OCP has a remarkable structural similarity to HA due to its layered structure involving apatitic and hydrated layers [40-43], parallel to the (100) face. It is generally assumed that, in solutions, the hydrated layer of the (100) face is the most likely exposed to solution [27].

The apatitic layer (1.1 nm thick) consists of phosphate ions inter-dispersed with Ca^{2+} ions resembling the ions positions in the structure of apatite.

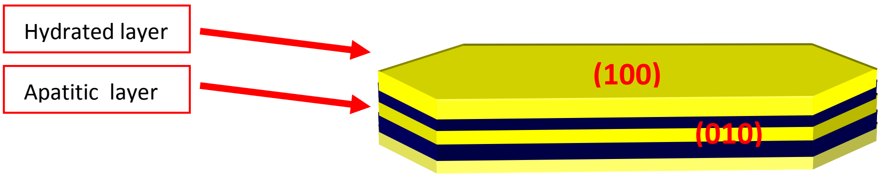

Figure 5 Layered structure of Octacalcium phosphate

The hydrated layer of the OCP unit cell may form an interphase between HA and the surrounding solution [44]. If this occurs, the epitaxial intergrowth of OCP and HA is favored.

The hydrated layer (0.8 nm thick) consists of more widely spaced phosphate and calcium ions with a slightly variable number of water molecules between them. Six of the Ca^{2+} ions and two of the phosphate ions are in the apatitic layer, the other two Ca^{2+} ions and one phosphate ion are in the hydrated layer and the remaining three phosphate ions lie at the junction of the apatitic and hydrated layers. The phosphate ion in the hydrated layer and one at the junction between the layers are protonated.

1.2.2.3 Dicalcium Phosphate Anhydrous

Dicalcium phosphate anhydrous (Monetite or DCPA) at room temperature crystallizes in the triclinic form, space group P-1 with lattice parameters a=6,9160Å,b=6,6190Å,c=6,9460 Å,α=96,18°,β=103,82°, γ= 88,34°. DCPA is less soluble than the hydrated form, DCPD, under all conditions of normal temperature and pressure and thus it might be expected to be of more frequent occurrence. However, its slow rate of crystal growth relative to DCPD [44] might explain why DCPD forms instead of DCPA, even though it is less stable. This observation again underlines the importance of kinetic factors in determining which phase is formed in the $Ca(OH)_2$-H_3P0_4-H_20 system.

There are four formula units per unit cell of DCPA. Double chains of •••Ca $P0_4$Ca $P0_4$ Ca $P0_4$ Ca$P0_4$••• (Figure 6), extending along the a-axis, are linked together in the 6-axis direction by Ca-O bonds to form distorted sheets of atoms approximately in the (001) plane: the centre of symmetry produces another sheet below this in the c-axis direction.

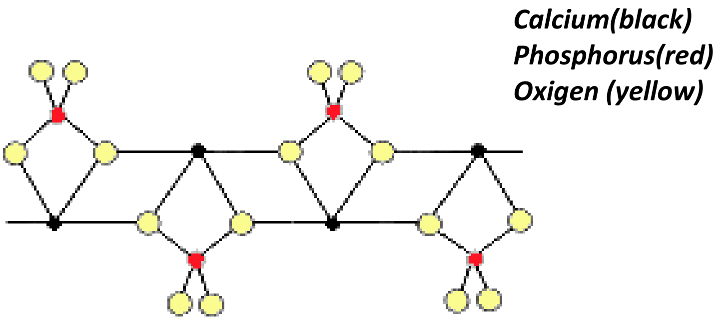

Figure 6 Double chain of Ca^{2+} ions and phosphates ions that characterize the DCPA structure

1.2.2.4 Alpha-Tricalcium Phosphate

Alpha-tricalcium phosphate (α-TCP) is used as the main constituent of calcium phosphate bioactive bone cements and biphasic calcium phosphate ceramics. Its hydrolysis and conversion into apatite phase may play an important role in new bone formation *in vivo*.

Alpha-TCP is highly reactive in aqueous systems and can be easily hydrolysed to a mixture of other calcium phosphates. Alpha-TCP crystallizes in a monoclinic structure, space group $P2_1/a$ and unit cell a = 12.887(2) Å, b = 27.280(4) Å, c = 15.219(2) Å and β = 126.20(1)°, with 24 formula units per unit cell [45]. There is an approximate subcell with a *b*-axis parameter of b/3 (9.09 Å) that contains 8 formula units, which corresponds to the unit cell reported earlier [46].

The structure of α-TCP is constituted of columns of Ca^{2+} and PO_4^{3-} ions which run parallel to the *c*-axis.

The α-TCP approximate subcell *b*-axis parameter of 9.09 Å corresponds to the apatite *a*-axis parameter, whilst half the *c*-axis parameter of α-TCP (7.6 Å) corresponds to the *c*-axis parameter of apatite. The apatite structure can so be derived from α-TCP by replacing the cation-cation columns at the corners of the apatite cell by anion columns (OH^- in hydroxyapatite, F^- in fluoroapatite…).

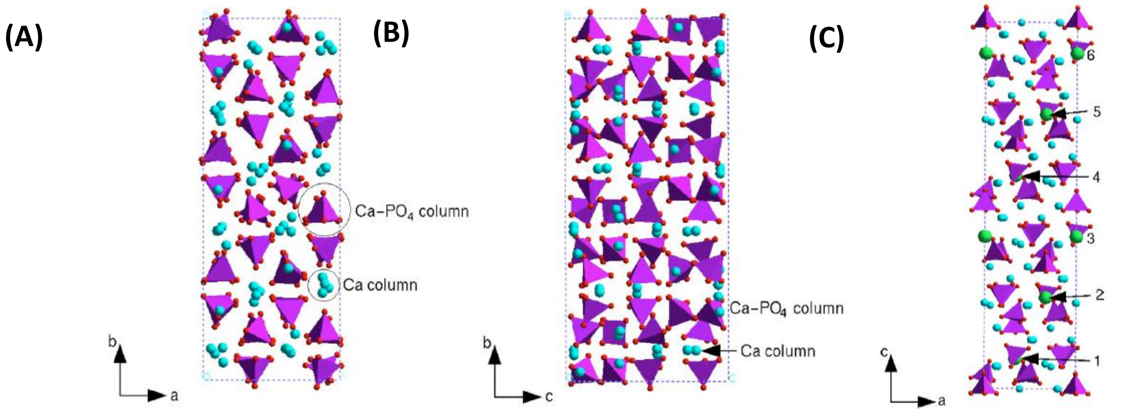

Figure 7 (A) α-TCP unit cell projected on the (*a*,*b*) plane and (B) projected onto the (*b*,*c*) plane. Tetrahedra represent PO_4 groups and light balls denote Ca atoms. (C) β-TCP unit cell projected on the (*a*,*c*) plane. Tetrahedra represent PO_4 groups, small balls designate Ca atoms and big balls are for the Ca's with half occupancy [48].

1.2.2.5 Beta-Tricalcium Phosphate

Beta-Tricalcium Phosphate (*β*-TCP) crystallizes in the rhombohedral space group *R*3*c*, and its unit cell contains 21 [$Ca_3(PO_4)_2$] formula units [47]. There are three types of crystallographically nonequivalent PO_4^{3-} groups located at general points of the crystal, each type with different intra tetrahedral bond lengths and angles.

β-TCP unit cell contains 21 formula units, 273 atoms in total, with one Ca site (multiplicity 6) only half occupied, implying a structure with three Ca vacancies per unit cell [48].

β-TCP can be obtained only at high temperature, by solid-state reaction or by thermal conversion of other phosphates, and it is stable up to 1125 °C (Above 1125°C *β*-TCP converts into α-TCP) [31].

β-TCP has been identified during pathological calcifications, such as dental calculi and renal stones, but it has not been observed in enamel, dentin, or bone [49]. The ideal *β*-TCP structure contains calcium ion vacancies that are too small to accommodate a calcium ion but allow for the inclusion of magnesium ions, which thereby stabilizes the structures [47]. The most common one (whitlockite), formed under physiological conditions, is stabilized by magnesium ions and is not detected physiologically, unless magnesium ions are present [47].

1.3 <u>Functionalization of CaP with bioactive ions and molecules.</u>

The possibility to change the structural and chemical properties of these materials, through ion substitution and/or adsorption of bioactive molecules, can extend the range of potential practical applications as bioceramic, catalyst, liquid-chromatographic column, lighting materials and chemical sensors. In fact, even small amounts of ionic substitution have been shown to have very significant effects on thermal stability, solubility, osteoclastic and osteoblastic response *in vitro*, degradation and bone regeneration *in vivo*. The adsorption of bioactive molecules on CaPs can be used to modify characteristics, such as surface morphology, microstructure, composition, and properties, with the purpose of enhance cellular response and for drug delivery.

1.3.1 Zinc

Zinc is an important metal in the normal growth and development of the skeletal system, where it has been shown to display an inhibitory effect on osteoclast differentiation and a promotion of osteoblast activity [50]. Zn ion is one of the most effective metal ions in inhibiting HA crystal growth [51, 52]. Nonetheless, it can be quantitatively incorporated into HA lattice by direct synthesis under mild conditions [53-55], through hydrothermal technique at 200 °C [56] and by means of a sol–gel process [57].

The lattice parameters of Zn-HA are related to the difference in ionic radius between Zn^{2+} (0.074 nm) and Ca^{2+} (0.099 nm).

Density function theory calculations confirm that Zn prefers the Ca(II) site over the Ca(I) site for the substitution, and favors tetrahedral coordination with significant local structural distortion.

In the tetrahedral coordination, one of the four oxygen atoms bonded to Zn is from the nearest hydroxyl group and three are from the adjacent phosphate groups. This arrangement causes a reduction in the *a* lattice parameters from 0.9488 nm to 0.9319 nm , whereas the Zn-O(OH) distance is 0.202 nm compared to 0.269 nm of ideal distance in HA [58].

The reported substitution limit of Zn in HA varies between 15% and 25% [59,60], and both Ca/P and (Ca+Zn)/P ratios decrease on increasing Zn content and, as a consequence, stoichiometry is no longer maintained [61].

1.3.2 Silver Nanoparticles

Silver nanoparticles find use in many fields; the major applications include their use as catalysts, as optical sensors, in textile engineering, in electronics, in optics, and most importantly in the biomedical field as a bacteriostatic and as a therapeutic agent. The size of these nanoparticles is in the range of 1 and 100 nm. The properties of Ag nanoparticles depend on their mean size, as well as on their structure, shape and size distribution. Generally, specific control of shape, size, and size distribution is often achieved by varying the synthesis methods, reducing agents and stabilizers [62-64].

The stabilization can be obtained in two ways, electrostatic and steric. Electrostatic stabilization is achieved by the coordination of anionic species, such as halides, carboxylates or polyoxoanions, to metal particles.

This results in the formation of an electrical double layer (really a diffuse electrical multilayer), which causes coulombic repulsion between the nanoparticles. Steric stabilization is achieved by the presence of bulky, typically organic materials (polymers) that, due to their bulk, hinder nanoparticles aggregation.

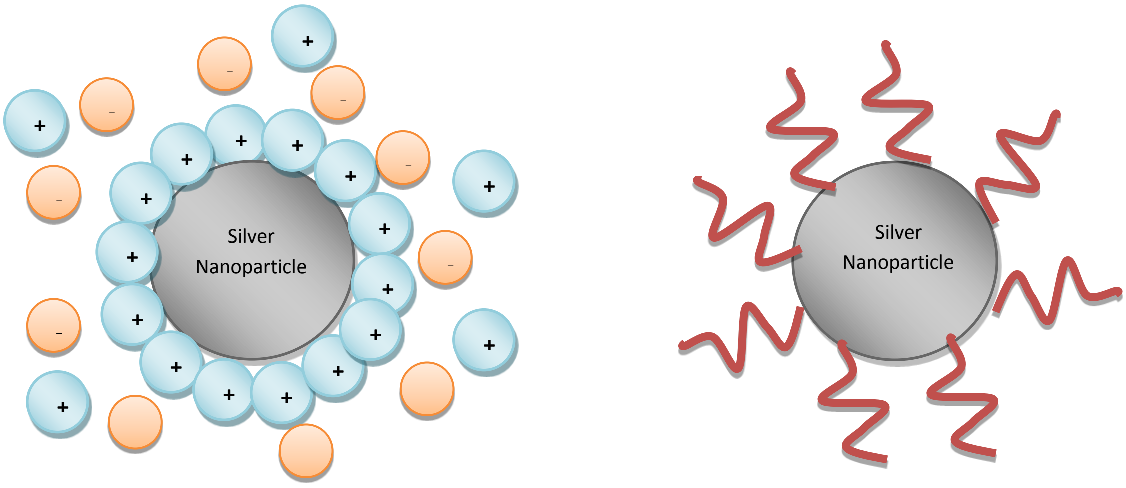

Figure 8 Electrostatic and steric stabilization of nanoparticles.

Currently, many methods have been reported for the synthesis of Ag-NPs by using chemical, physical, photochemical and biological routes [65].

The most widely accepted mechanism of silver biosynthesis is the presence of the nitrate reductase enzyme, that might be responsible for the bioreduction of silver ions and the subsequent formation of silver nanoparticles to metallic silver (Ag+ to Ag0) [66].

The physical approach utilizes several methods such as evaporation/condensation [67,68] and laser ablation [69-71].

In the chemical approach the metal ions in solution are reduced in conditions favoring the subsequent formation of small metal clusters or aggregates [72-74]. Chemical reduction is the most frequently applied method for the preparation of AgNPs as stable, colloidal dispersions in water or organic solvents. Commonly used reductants are borohydride, citrate, ascorbate and elemental hydrogen [75, 76]. The reduction of silver ions (Ag^+) in aqueous solution generally yields colloidal silver with particle diameters of several nanometers. Initially, the reduction of various complexes with Ag+ ions leads to the formation of silver atoms (Ag^0), which is followed by agglomeration into oligomeric clusters. These clusters eventually lead to the formation of colloidal Ag particles.

1.3.3 Flavonoids

Flavonoids are a ubiquitous group of polyphenolic substances which are present in most plants, concentrated in the seeds, fruit skin or peel, bark and flowers [77]. More than 4000 different flavonoids have been identified to date, making them the largest group of plant chemicals. Many fruits and vegetables, especially buckwheat, apple and onion, contain flavonoids [78].

Quercetin is the most biologically active and common dietary flavonoid, and is generally used as a dietary supplement.

The carbon atoms in flavonoid molecules are assembled in two aromatic rings, commonly denoted as A and B, which are connected by a three-carbon “bridge”: C6–C3–C6, thus forming a diphenyl-propane structure with the central unit being a benzo-α-pyrone (chromone). Multiple hydroxyl groups, sugar, oxygen, or methyl groups are attached to this core structure.

Depending on the oxidation state and on the position of the heterocyclic ring, flavonoids are classified as (Figure 9):

– ring B in position 2: flavanones, flavones , flavonols , antocianine;

– ring B in position 3: isoflavones.

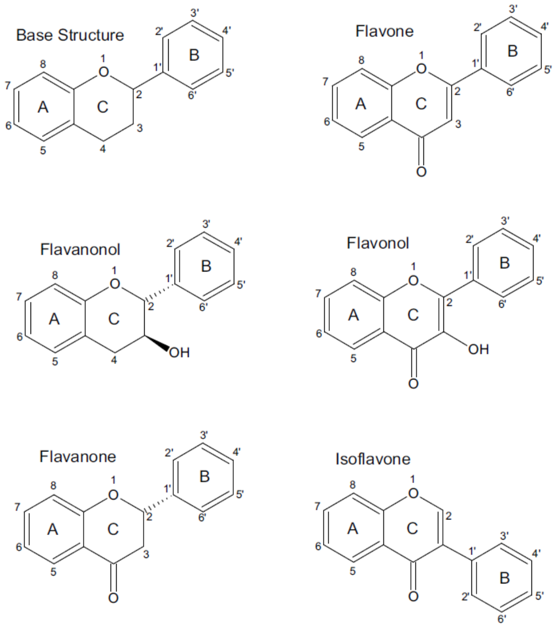

Figure 9 Classification of flavonoids based on the position of B ring [88]

Scientific studies conducted in the last few years generated a growing interest in the potentially important role of flavonoids in maintaining human health. The pharmacological effects are related to the anti-oxidant activity of flavonoids, arising from their ability to scavenge free radicals. Radical scavenging by flavonoids occurs *via* electron donation from the free hydroxyls on the flavonoid nucleus with the formation of a less reactive flavonoid aroxyl radical, which is stabilized by resonance and therefore plays only a moderate role in the propagation of radical- induced damage in biological systems.

In particulary, quercetin has been reported to exhibit antibacterial activity [79] and to reduce bone resorption in vitro via the direct targeting of the mature osteoclasts by a mechanism involving estrogen receptors (ERs) [80,81].

Moreover, it inhibits mRNA expression of osteoclast related genes [82] and osteoclast differentiation [83, 84].

Being pigments responsible for the color of leaves, herbs and petals, flavonoids strongly absorb ultraviolet (UV) radiation. Therefore UV–Vis spectroscopy remains the main tool for structural analysis of flavonoids. Typically, the major absorption maxima observed in the UV–Vis spectrum. are two: the absorption maximum observed in the range 240–285 nm is referred to as the band II and the one between 300–400 nm as the band I. In general terms, absorption band II may be considered as originating from $\pi \rightarrow \pi^*$ transitions in the A ring, a benzene system, whereas the absorption band I is attributed to transitions in the B ring, a cinnamoyl system (Figure 10). The position of band I in flavones is between 304–350 nm, while flavonols absorb in the range 352–385 nm. Highly oxygenated flavones and flavonols tend to absorb at longer wavelengths than those with fewer oxygen substituents. Methylation or glycosylation of the hydroxyl groups on the flavonoid nucleus usually results in hypsochromic shifts, predominantly of band I [85].

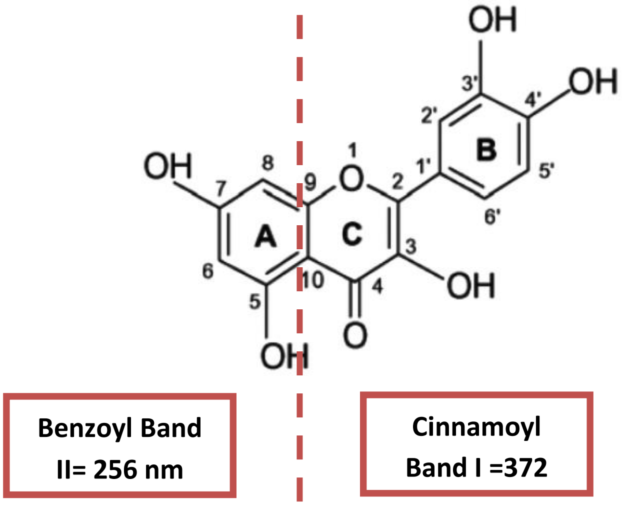

Figure10 Benzoyl and cinnamoyl group of quercetin and relative Uv-Vis absorbance values

Due to their specific chemical structure, flavonoids easily chelate metal ions and create complex compounds. There are three domains that can likely interact with metal ions, the 3',4'-dihydroxy group located on the B ring, the 3-hydroxy or 5-hydroxy and the 4-carbonyl groups in the C ring. Generally, the chelating properties of flavonoids toward metal ions have been attributed to the presence of the 3- or 5-hydroxypyran-4-one, rather than the *ortho*-hydroxyl groups in the B ring [86].

Thanks to this ability they are able to prevent metal-mediated generation of free radicals and, accordingly, may protect the potential biological targets from oxidative stress. Thus, the overall anti-oxidant action of flavonoids appears to be a combination of a direct reaction with free radicals and of a chelation of the metal ions responsible for the production of reactive oxygen species.

The pH has an important influence on Flavonoids, which are weak polybasic acids that tend to protonate. Therefore, pH has a strong impact on complex formation with metal ions [87]. For example, pH values around 6 favor deprotonation of flavonoids and, consequently, more complex species. On the other hand, at higher pH values, metal ions are often involved in side reaction (hydrolysis) and hydroxo-complexes are formed [88].

Complexation with flavonoids as unidentate or bidentate ligands leads to the formation of complexes that contain protons in addition to the metal ion and ligand (so-called protonated complexes) which tend to dissociate at pH values higher than 6. In this case, the dissociations of the protonated complexes or the formation of new complexes with different stoichiometric composition could be observed. Hence, the absorption spectra exhibit a bathochromic shift, as shown by Malesev et al. 2007 for the titanyloxalato-quercetin complex [88].

1.3.3.1 Quercetin

Quercetin (IUPAC 3,3',4',5,7-pentaidrossiflavone) belongs to the flavonols group and it is the agliconic component of various glicosides, like rutin and quercitrin.

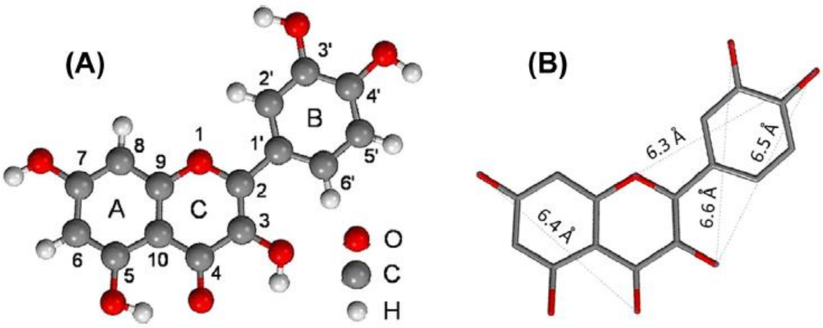

Figure 11 Molecular structure of quercetin: (A) ring lettering and atom numbering convention; (B) oxygen–oxygen distances that roughly match structural Ca–Ca distances in HA [93].

The biochemical activity of quercetin depends on the structure and the relative orientation of the rings and of the hydroxyl groups inside the molecule. The B ring hydroxyl configuration mostly determines the antioxidant effect, while the activity of the other hydroxyl position is not yet clear [89].

The torsion angle of B ring compared to all the other part of the molecule strongly influences the antioxidant activity. The planarity allows the coniugation, the electronic dislocation and a consequent increase in stability of the phenoxide radical.

The removal of –OH in position 3 deletes the coplanarity and the coniugation, thus compromising completely the quercetin antioxidant activity in the oxidation of linoleic acid [90].

It has been assumed that the hydroxyl group of B ring forms a hydrogen bonding with the –OH group in position 3, aligning the B ring with the heterocycle and the A ring. Deleting this hydrogen bonding compromised the electron delocalization property.

The molecular geometry is defined by two effects that act in oppositely: the hydrogen atom repulsion in ortho position on the B ring, that would bring the molecule in a staggered position, and a coniugation effect that tends to bring the phenyl in the chromone plan.

The data obtained by X-ray analysis show that quercetin crystallizes in the spatial group P1, with two water molecules for unit cell [91]. With five hydroxyls groups and one carbonyl, quercetin has a huge possibility to create intra- and intermolecular hydrogen bonds.

Quercetin contains two crystallization water molecules, which take part in a wide network of hydrogen bonds across the crystal. The hydroxyl groups in position 3 and 5, in fact, are involved in intra-molecular hydrogen bonds with the carbonyl oxygen in position 4 [92]. This oxygen atom takes part to the formation of a dimer obtained through the inter-molecular hydrogen bond with the hydroxyl group in position 5 of the adjacent molecule. Quercetin, hence, has a quasi-planar structure and tends to form highly oriented nanostructure in suspension.

Quercetin molecular dimensions are similar to those between the Ca^{2+} ions on the (110) face of HA. Moreover quercetin has a negative charge on the molecular plane and so it could be attracted by the calcium ions present in the HA structure. On this basis, it has been suggested that quercetin could act as soft template in the regulation of crystal growth direction of HA [90].

1.3.4 Polydopamine

Dopamine (DA) is a neurotransmitter which is found in animal/humans and has a chemical structure similar to 3,4-dihydroxy phenylalanine (DOPA).

DA contains catechol and amine functional groups that can self-polymerize in weak alkaline solution to form polydopamine (PDA). Similar to DOPA, PDA can tightly adsorb on the surface of materials. Moreover, PDA is an excellent reducing agent that can be employed to produce metal nanoparticles via direct reduction of a metal precursor salt at room temperature [94-96].

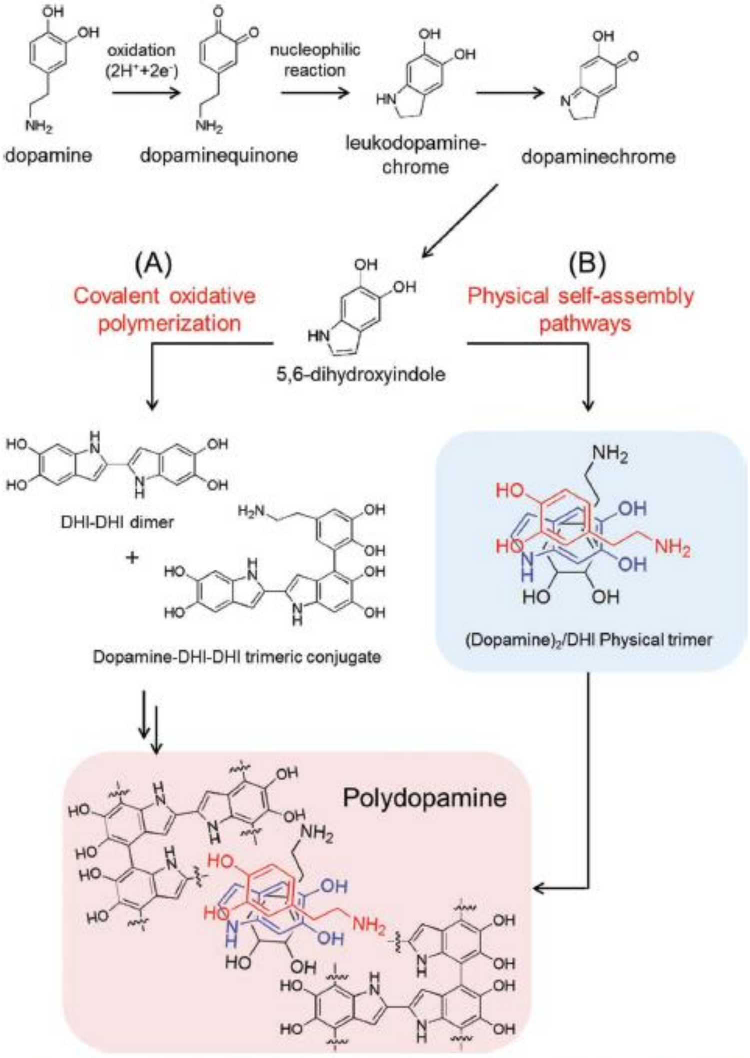

Figure 12 Polydopamine synthesis occurs via two pathways: (A) a pathway of covalent bond-forming oxidative polymerization and (B) a newly proposed pathway of physicalself-assembly of dopamine and DHI [98].

Thanks to its chemical properties (reactivity with nucleophiles, its ability to chelate metal ions, and its redox activities) polydopamine can be applied to various types of surface with the aim of creating new materials with advanced properties. Polydopamine is spontaneously formed by pH-induced, oxidative polymerization of dopamine-hydrochloride in alkaline solutions (pH > 7.5), but the molecular mechanism behind polydopamine formation is not fully clarified yet. It has been suggested that polydopamine formation shares many characteristics with melanin biosynthesis pathways [97]. Melanin biosynthesis includes an oxidative reaction pathway, which transforms dopamine into 5,6-dihydroxyindole (DHI), followed by further polymerization steps.

Polydopamine is formed through two different pathways, non-covalent self-assembly and covalent polymerization where the first process occurs in parallel with the second one (Figure 12). Moreover, a significant amount of dopamine remains unpolymerized as a self assembled stable complex [98].

Thanks to its chemical structure, that incorporate many functional groups, polydopamine is not only used as a coating material but also for applications across the chemical, medical, biological and materials sciences (Figure 13). These functional groups (such as catechol, amine, and imine) can serve as starting points for covalent modification with a wide numbers of molecules or for the loading of metal ions.

The primary advantage of polydopamine is that it can be easily deposited on all types of inorganic and organic substrates, with controllable film thickness and durable stability. In this way it is possible to create numerous multifunctional substrates with specific properties, using the grafting of diverse species including DNA [99], proteins [100], growth factors [101], hydroxyapatites [102], noble metal nanoparticles [103], polymers [104] and other molecules [105−107].

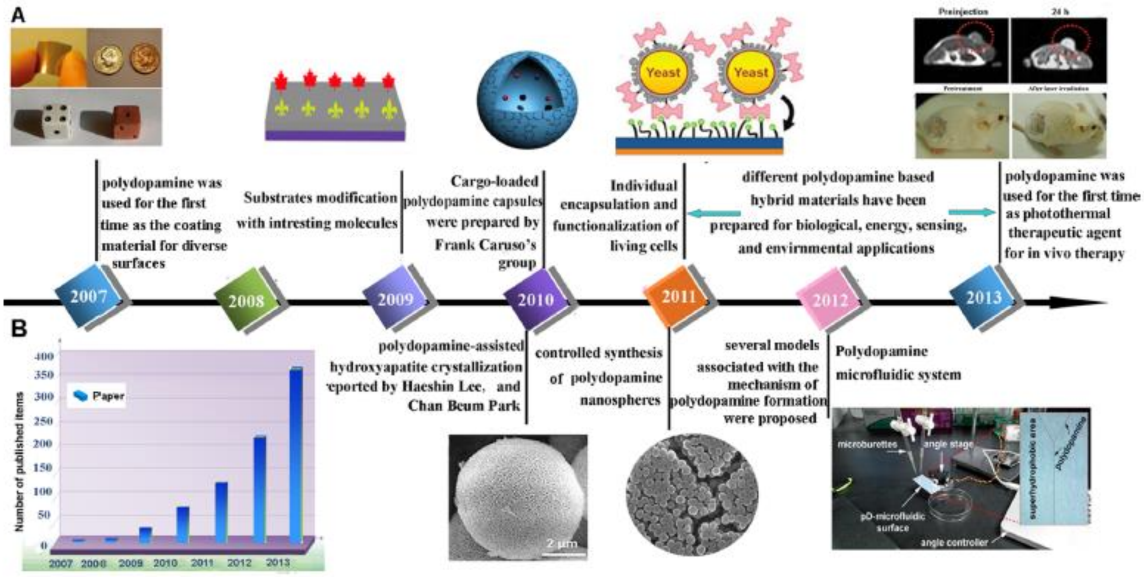

Figure 13 (A) A brief timeline for the development of the use of polydopamine in different application. (B) The number of publications in terms of polydopamine sorted by year [108].

1.3.5 Polyethylenimine (PEI)

The versatility of PEI is to be either a linear or a branched polymer, and its use is determined by these structural chain properties. Branched polyethyleneimine (B-PEI) contains branched chains of primary, secondary, and tertiary amino groups, in a 1:2:1 ratio, and has been produced since the early 1940s by acid-catalyzed aziridine-based aqueous solutions [109].

Linear polyethyleneimine (L-PEI), also known as crystalline polyethyleneimine, is made of – (CH2–CH2–NH)– repeating units and was first synthesized in 1970 by Dick by cationic polymerization of 2-substituted-2-oxazolines [110].

PEIs have been extensively studied as a vehicle for DNA delivery system thanks to the electrostatic interactions between the positively charged polymer and the negatively charged phosphate groups of DNA. In aqueous solution, PEI condenses DNA and the resulting PEI/DNA complexes, carrying a net positive surface charge, can interact with the negatively charged cell membrane and be readily internalized into cells [111].

1.3.6 Bisphosphonates

Bisphosphonates (BPs) are currently the major class of drugs used for the treatments of osteoporosis and other diseases characterized by increased bone resorption, like Paget's disease and bone-related cancers.

The first examples of BPs were developed in the 1970s and 1980s for the treatment of diseases characterized by abnormal calcium metabolism but was only in the late 1990s, thanks to a successful screening of new compounds in short term rat models [112,113], that the importance of bone affinity and the involvement of cellular target of BPs were showed.

BPs are synthetic pyrophosphate analogs, in which the P-O-P group is replaced by the P-C-P bridge, where the two P are two phosphonic acid groups bound to the same carbon (Figure 14).

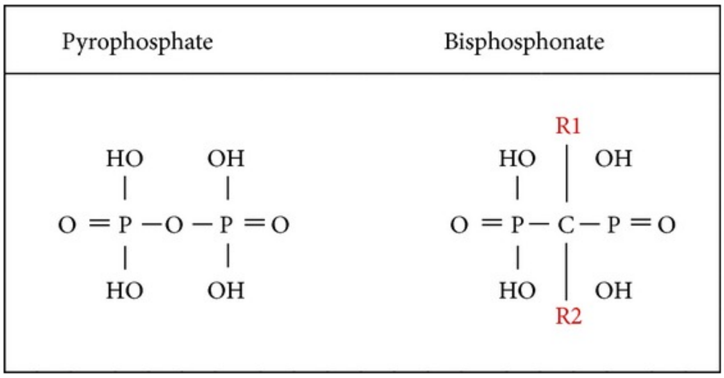

Figure 14 Structure of inorganic pyrophosphate and a generic bisphosphonate [114].

Stability is conferred by the carbon atom that connects the two phosphonates, making the molecule able to withstand incubation in acids or with hydrolytic enzymes.

The P-C-P moiety is responsible for the strong affinity of the bisphosphonates for the skeleton and allows for a series of variation in the structure based on the substitution of the R1 and R2 sidechains. The ability of the BPs to bind to bone mineral is enhanced when the R1 sidechain is a hydroxyl group [115] because it increases the affinity for bone mineral, owing to the ability of these bisphosphonates to chelate calcium ions more effectively by tridentate rather than bidentate binding.

In the years, several kinds of bisphosphonates with different groups in the R1 and R2 chains were studied, giving rise to different classes of molecules, with different properties (Figure 15).

In particular, bisphosphonates containing a basic primary nitrogen atom in an alkyl chain (as pamidronate and alendronate) were found to be 10-100 fold more potent than the non-nitrogen containing molecules. In the nitrogen containing class, there are also ibandronate, olpadronate, risedronate and zoledronate. The two first molecules contain a tertiary nitrogen that enhances the ability to inhibit bone resorption, and the last two types, containing a nitrogen atom within a heterocyclic ring, are 10.000 fold more potent than etidronate, in some experimental system [116].

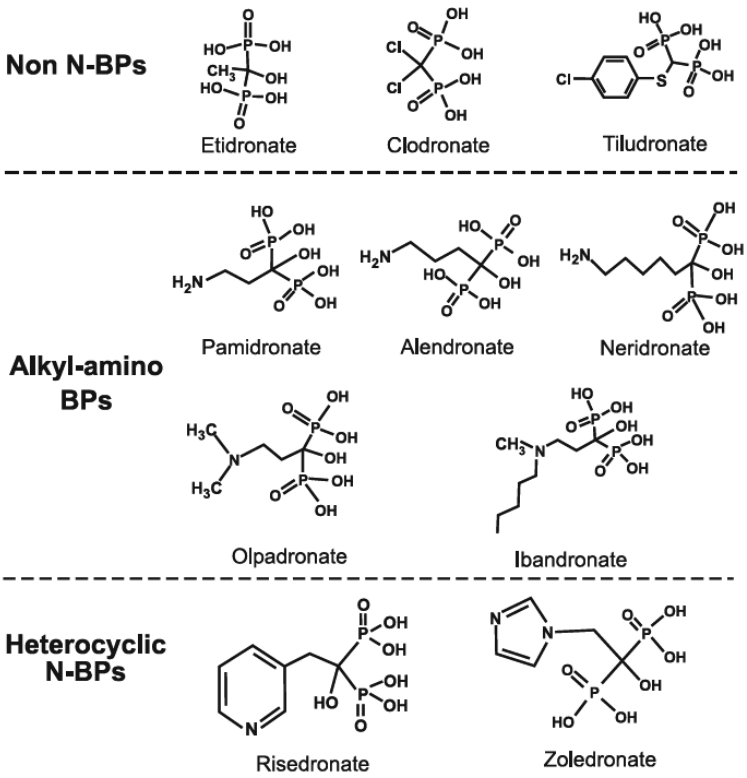

Figure 15 Structure of non-nitrogen containing bisphosphonate, alkyl-amino bisphosphonate and heterocyclic nitrogen containing bisphosphonate [120].

Altrough the structure of the R2 side chain is the major determinant of antiresorptive potency, both phosphonate groups are also required for the drugs to be pharmacologically active. Infact, alteration to one or both phosphonates groups reduces the affinity for bone mineral and consequently the activity [117].

Some studies suggest that the ability of bisphosphonates to inhibit bone resorption is dependent on two separate properties of the BPs molecules [118]. The two phosphonate groups, together with a hydroxyl group at the R1 position, impart high affinity for bone mineral and act as a “bone hook”, allowing rapid and efficient targeting of bisphosphonate to bone mineral surfaces [116]. Once localized within bone, the structure and the three dimensional conformation of the R2 side chain determine the biological activity of the molecule and influence the ability of the drugs to interact with specific molecular target.

The likelihood and the duration of the attachment of BPs to bone can be predicted considering the binding affinity of this molecules to HA, as demonstrated in some studies [119] which showed the following affinity rank order: clodronate < etidronate < risedronate < ibandronate <alendronate < pamidronate < zoledronate.

The binding affinity and consequently the loading capacity can be also influenced by the physicochemical properties of N-BPs, such as molecular charge [110].

When BPs bind to HA, the nitrogen in the R2 side chain would be expected to confer a charge at the mineral surface, resulting in a differential change in zeta potential [121]. These changes might have multiple consequences, including effects on the further binding of charged molecules, the total amount of BP that can bind to the bone surface (loading capacity), cellular distribution, skeletal distribution, and interactions with charged ions and matrix constituents.

The more positively charged BPs (alendronate, ibandronate, and zoledronate) should create a more positively charged bone surface and thereby may attract additional BPs to bind to the bone surface *via* their negatively charged phosphonate moieties. This may further augment the accumulation of BPs and increase the maximum binding capacity on the bone crystals.

On the other hand, the less positively charged N-BPs (e.g., risedronate) lead to a more negatively charged bone surface, which may limit further accumulation of BPs, and therefore lessen the maximum binding capacity on the crystal surface. Thus, zeta potential may be an independent property that does not correlate directly with affinity, but rather influences binding capacity.

Small changes in BP chemical structure have been shown to lead to substantial changes in the three dimensional (3-D) shape and atomic orientation. Therefore, it is postulated that the 3-D configuration of a nitrogen-containing BP (N-BP) and the orientation of its nitrogen may play an important role in mineral binding affinity [122-124].

Some N-BPs can form N-H-O hydrogen bonds on the HA surface. These N-H-O hydrogen bonds can be formed at two sites on HA and require an N-H-O angle ≥125° and an N-O distance of approximately 3 Å for optimal binding. One H binding site can occur at a hydroxyl at the same position in which fluoride is known to substitute. This hydroxyl is coordinated to the second type of calcium (CaII) in HA.

A second H bonding interaction can occur at neighboring calcium (CaI), which can optimally allow a bifurcated dual bonding arrangement. Overall, this indicates that N-BPs that can form any of these bonds will have a higher affinity for bone mineral [132].

The clinical efficacy of BPs primarily stems from two key properties: their ability to bind strongly to bone mineral (they inhibit the de novo precipitation of calcium phosphate from solution, delay the transformation of amorphous to crystalline HA, and inhibit the aggregation and dissolution of HA crystals [125-127], and their inhibitory effect on mature osteoclasts.

The adsorption of bisphosphonates to HA bone mineral surfaces brings them into close contact with osteoclasts and other cells in the bone.

During the process of bone resorption, the subcellular space beneath the osteoclast is acidified by the action of vacuolar-type proton pumps in the ruffled border of the osteoclast membrane. The acidic pH of this microenvironment causes dissolution of the hydroxyapatite bone mineral, whilst the breakdown of the extracellular bone matrix is brought about by the action of proteolytic enzymes. Since bisphosphonates adsorb to bone mineral, especially at sites of bone resorption where the mineral is most exposed [128-130], osteoclasts are the cell type in bone most likely to be exposed to the highest concentrations of free, non-mineral-bound bisphosphonate, as a result of the release of the bisphosphonate from bone mineral in the low pH environment beneath osteoclasts.

At molecular level, Bisphosphonates act in two different ways (Figure 16). The simple BPs are metabolized to toxic analogues of ATP, it is likely that intracellular accumulation of these metabolites within the osteoclast inhibits osteoclast function and may cause cell apoptosis.

In contrast, the nitrogen-containing bisphosphonates interfere with other metabolic reactions, for example, the mevalonate pathway [130-132] that is responsible for the production of cholesterol and isoprenoid lipids, such as isopentenyldiphosphate (IPP), farnesyldiphosphate (FPP), and geranylgeranyldiphosphate (GGPP). FPP and GGPP are responsible for the prenylation of small GTPases (like Ras, Rho, Rac) which are important signaling proteins that regulate a variety of cell processes important for osteoclast function, including: cell morphology, cytoskeletal arrangement, ruffled border and apoptosis [133, 134].

Prenylation is required for the correct function of these proteins, since the lipid prenyl group serves to anchor the proteins in cell membranes and may also participate in protein-protein interaction [135,136].

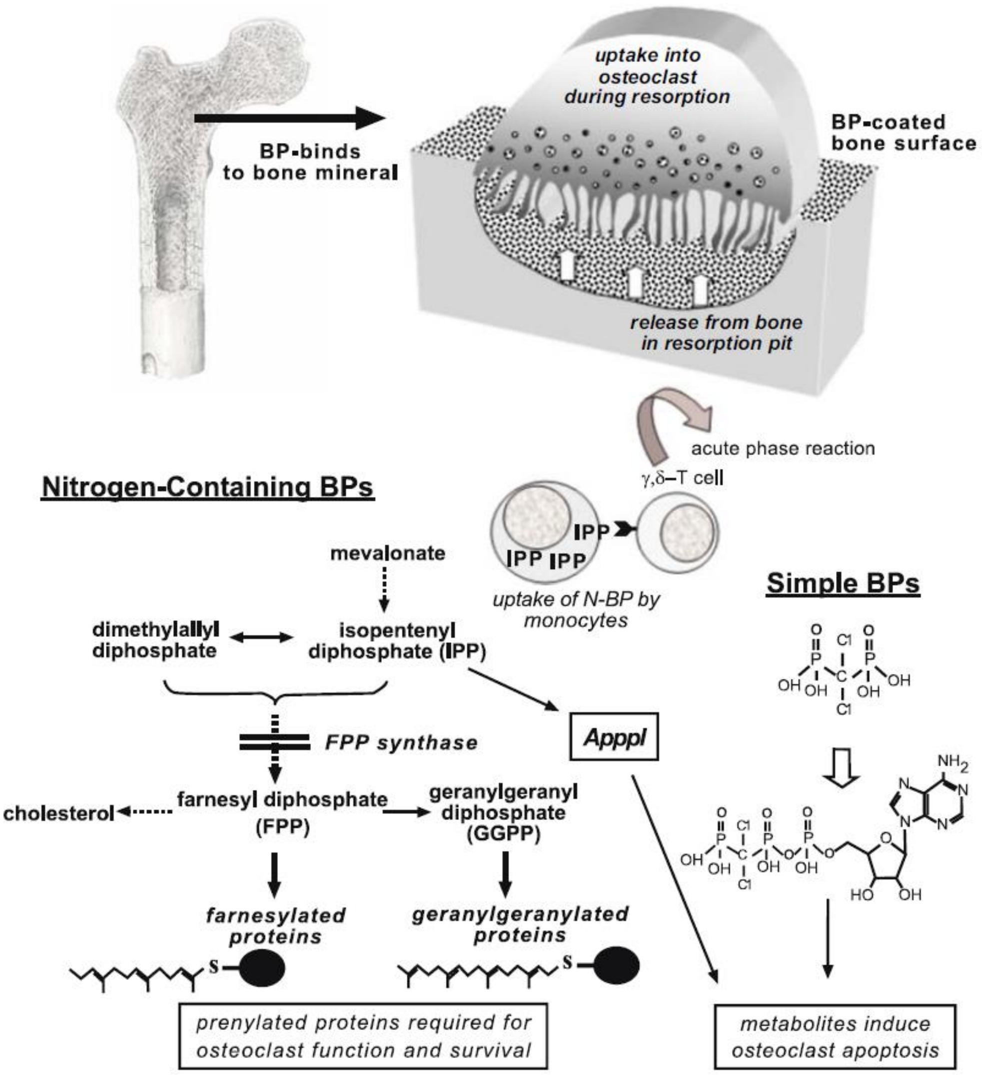

Figure 16 Mechanism of action of nitrogen containing bisphosphonate and simple bisphosphosphonate [120].

1.4 Adsorption / Release

Adsorption processes involve two substances. One is the solid or the liquid on which adsorption occurs and it is called adsorbent. The second is the adsorbate, which is the gas or liquid or the solute from a solution which gets adsorbed on the surface.

Depending upon the nature of forces existing between adsorbate molecules and adsorbent, adsorption can be classified into two types:

1. **Physical adsorption (physisorption):** If the force of attraction existing between adsorbate and adsorbent are Vander Waal's forces, the adsorption is called physical adsorption. It is also known as Vander Waal's adsorption. In physical adsorption the force of attraction between the adsorbate and adsorbent is very weak, therefore this type of adsorption can be easily reversed by heating or by decreasing the pressure.

2. **Chemical adsorption (chemisorption):** If the force of attraction existing between adsorbate and adsorbent is almost of the same strength as chemical bonds, the adsorption is called chemical adsorption. It is also known as Langmuir adsorption. In chemisorption the force of attraction is very strong, therefore adsorption cannot be easily reversed.

Isotherm adsorption models

An isotherm is a model that describes the retention/release or mobility of a substance from the aqueous porous media or aquatic environments to a solid-phase at a constant temperature and pH [137].

Adsorption equilibrium (the ratio between the adsorbed amount and that remaining in the solution) is established when the adsorbate containing phase has been in contact with the adsorbent for sufficient time, and the adsorbate concentration in the bulk solution is in a dynamic balance with the interface concentration [138,139].

The parameters obtained by the isotherm equation express the surface properties and the affinity of the adsorbent, at a fixed temperature and pH.

To evaluate the accuracy of the fit of a two parameters isotherm model, the magnitude of the coefficient of determination (R^2) for the linear regression has to be close to the unity.

Over the years, a wide variety of equilibrium isotherm models have been formulated, those used for this study are described later.

Langmuir Isotherm

The Langmuir isotherm can be obtained based on the following key assumptions:

- adsorption is localized and reversible;

- adsorption sites are energetically equivalent, with no lateral interaction and steric hindrance between the adsorbed molecules, even on adjacent sites

These assumptions imply that each site can adsorbs a maximum of one molecule of solute, and that the probability of adsorption is the same for each site. The formula of the isotherm is:

$$Q_{ads} = N \times \frac{\left(K \times C_{eq}\right)}{1 + \left(K \times C_{eq}\right)}$$

where:

N is the amount of BPs adsorbed at saturation, expressed in mg of adsorbed molecules / m^2 of solid or µmol/ m^2

K is the affinity Langmuir constant of adsorbed molecules for the slid expressed in mol/L

K and N can be determined by plotting C_{eq} / Q_{ads} vs C_{eq} .

Freundlich Isotherm

The Freundlich isotherm describes the non-ideal and reversible adsorption, not restricted to the formation of a monolayer. This empirical model can be applied to multilayer adsorption, with non-uniform distribution of adsorption heat and affinities over the heterogeneous surface [140]. In this perspective, the amount adsorbed is the summation of adsorption on all sites (each having bond energy), with the stronger binding sites occupied first, until adsorption energy exponentially decreases upon the completion of adsorption process [141].

The formula of the isotherm is:

$$Q_{ads} = K \times C_{eq}{}^{n}$$

K is a constant expressed in µmol/m^2 and n express the surface heterogeneity.

The slope ranges between 0 and 1 is a measure of adsorption intensity or surface heterogeneity, becoming more heterogeneous as its value gets closer to zero. On the other hand, a value below unity implies chemisorption process where 1/n above one is an indicative of cooperative adsorption [142].

Langmuir- Freundlich Isotherm or SIPS

The Langmuir-Freundlich isotherm is commonly used to describe the adsorption characteristic for the heterogeneous adsorption systems and with a low interaction Adsorbate/Surface. At low adsorbate concentrations, it reduces to Freundlich isotherm; while at high concentrations, it predicts a monolayer adsorption capacity characteristic of the Langmuir isotherm [143].

The formula of the isotherm is:

$$Q_{ads} = N \times \frac{\left(K \times C_{eq}\right)^{n}}{1+\left(K \times C_{eq}\right)^{n}}$$

Where N (L/mM), K (µmol/m^2), n express the surface heterogeneity and lateral interactions parameters.

1.4.2 Drug Delivery

A way to treat bone disorders is by using local drug delivery devices. The local delivery of drugs should greatly reduce any systemic toxicities and side effects and open the door to entire classes of new treatments. These combined systems are able to administer high drug concentration in relevant tissues and to precisely control the timing of a drug release by adjusting the properties of the carriers.

For this purpose, synthetic polymers are widely used [144] because they do not cause any considerable inflammation to tissues at the implantation site. In that case, the release of biomolecules can be regulated by various mechanisms: desorption, diffusion, carrier degradation, and environmental stimuli, or controlled by the combination of the abovementioned factors (Figure 17) [145].

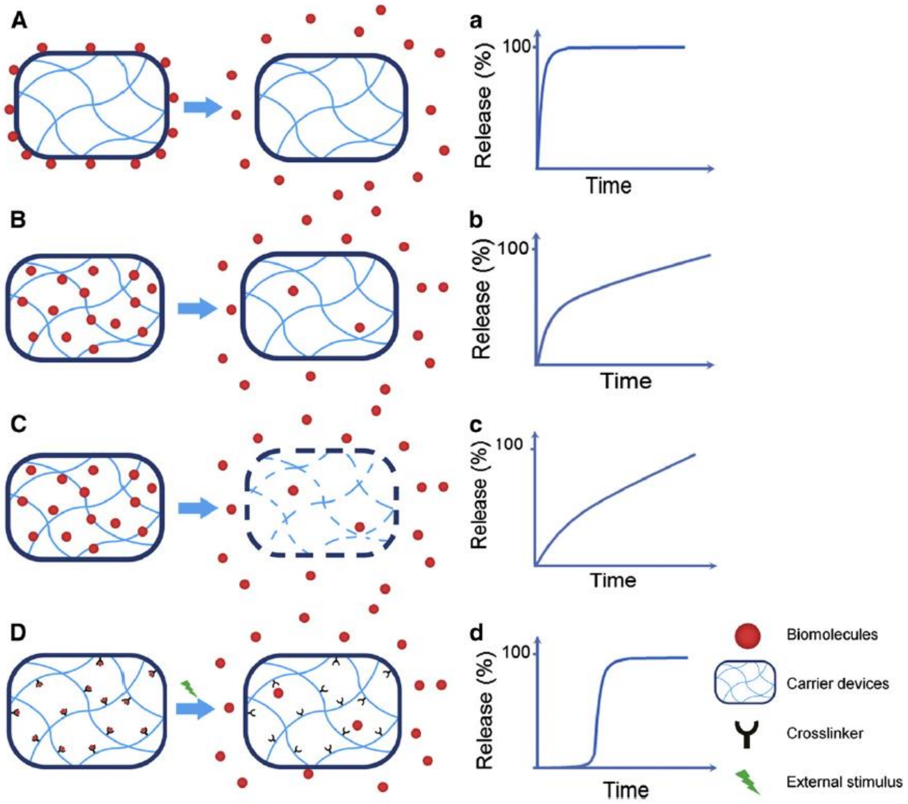

Figure17 Schematic diagram of various mechanisms for biomolecules release from carrier devices. (A-D) and typical corresponding pharmacokinetics (a-d). (A) and (a) desorption controlled release; (B) and (b) diffusion controlled release; (C) and (c) degradation controlled model; (D) e (d) stimuli-triggered release [145].

Typical desorption-controlled delivery vehicles are carriers in which biomolecules cannot penetrate inside the carrier network.

However, limitations of this strategy are obvious, including the tendency of biomolecules to deactivate during adsorption, poor capacity of delivering hydrophilic molecules, and poor control over delivery, retention, orientation, or desorption rate of biomolecules [146].

Hydrogels and polymeric fibrous membranes, that allow diffusional loading of biomolecules into polymer networks, act as drug delivery systems through diffusion process and provide a protective environment for biomolecules, prolonging their retention at treatment sites. The release profile for diffusion controlled delivery systems is normally characterized by an initial burst release, followed by a phase of sustained release that can be further regulated by fine-tuning the physicochemical properties of carrier materials [147].

Fragile biomolecules can be immobilized by physical or chemical interaction and thus be preserved from harsh environmental factors, and released with high degree of controllability by tailoring molecular weight, crosslinking and morphology of the carrier materials. In this case a degradation-controlled release system can occur.

Finally, molecules can be released with “programmed” or “triggered” systems working thank to environmental factors (e.g. pH, protein, glucose) or by external stimuli (e.g. temperature, ultrasound and irradiation) [148,149].

Although most of these drug carriers are polymers, some inorganic materials can also play a role. Indeed, calcium phosphate based materials, in various forms including ceramics, cements, composite and thin coatings, could have an added value as drug carriers for the bone tissue.

From the biological point of view, CaPs can be resorbed by cells, present evident osteoconductive and bioactive properties. Moreover, another relevant property of calcium phosphates is their unique ability to adsorb different chemical species on their surfaces.

Since the 90s, a large number of works describing different types of calcium phosphate / biomolecules system are reported in the literature. The combination of therapeutic agents such as cisplatin with poorly or well crystallized calcium phosphate [150]; the combination of antibiotics such as gentamycin, vancomycin and ampicillin with calcium phosphate cements [151,152], the incorporation of growth factors in calcium phosphate apatites [153,154], are just few examples.

However, most of these studies focus on the study of the processes of association or incorporation and the nature of the interactions molecules-media, and provide little or no details about the release mechanism involved in these associations.

Among the therapeutic molecules mostly used for the treatment of bone diseases, there are various compounds of the BPs family. In the case of BPs, a targeted and controlled release would notably increase the bioavailability of the active substance in the body and reduce the side effects [155,156].

Thus, alendronate, a BP molecule, has been associated with matrix-type systems such as hydrophilic matrix based polymer [157] or a mesoporous material ordered silica [158] to allow its local release. In the case of these two studies, the identified release mechanism is a BP diffusion through the matrix.

In addition, the release of alendronate has been studied repeatedly [159] from polymer based composite microspheres (PLGA) and from nanocrystalline apatite [160].

1.5 <u>Applications of CaPs as coatings of metallic implants</u>

Metals have been used in medical implants for many centuries because they provide the necessary strength and toughness that are required in load-bearing parts of the body.

On the other hand, metallic implants show various side effects caused by their high potential to corrode and leak corrosion product in the biological environment, which generally causes inflammation and osteolysis. Additionally, their low surface hardness and high friction coefficient limit their biomedical applications. Another problem associated with metallic implants is that they are bioinert materials and consequently they are incapable of inducing osteogenesis.

Improved implant fixation to hard tissues can be achieved by coating the metallic surface with a thin film of calcium phosphates. The deposition of calcium phosphates films on medical implants enable to combine the high mechanical strength of metallic implant with excellent bioactivity of the calcium phosphates surface layers.

Coatings can be deposited by several physical and chemical methods, including plasma spray, pulsed laser deposition, sputtering, electrodeposition, anodic deposition and anodic spark deposition, sol-gel dipping and biomimetic deposition [161-175].

Among these numerous techniques, pulsed laser deposition (PLD) is commonly used to produce calcium phosphate coatings, because this method is characterized by high deposition rate as well as possibility of precise control of thickness and composition of the growing layer (Figure 18).

On the other hand, PLD applied to organic and polymeric materials tends to cause some degree of irreversible decomposition or damage because the interaction of the UV photons with the polymeric or organic molecules causes the loss or decomposition of functional groups.

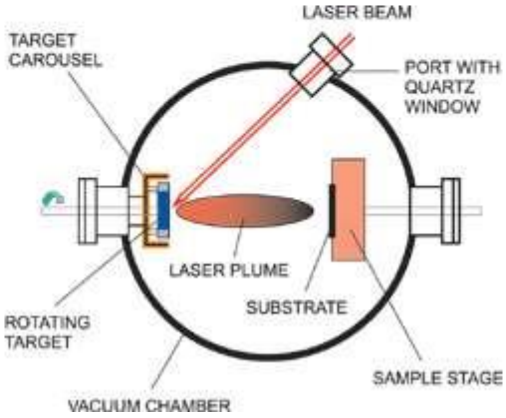

Figure 18 Scheme of the PLD technique (www.andor.com)

One approach that has shown great promise, in the case of polymeric or organic molecules, is known as matrix-assisted pulsed laser evaporation, or MAPLE.

Matrix-Assisted Pulsed Laser Evaporation

The MAPLE process was developed in the late 1990s at the U.S. Naval Research Laboratory to provide a gentler pulsed laser evaporation process for functionalized polymers [176].

In MAPLE deposition technique, the pulsed laser beam is focused on a target obtained as a frozen solution in a relatively volatile solvent of the molecules to be deposited (Figure 19). The advantage of MAPLE with respect to PLD technique is that a great part of the laser beam energy is transferred to the solvent and molecules to be deposited, which are ejected from the target mainly due to solvent vaporization.

In MAPLE, the target usually contains 55 wt% of solute material, that is, polymer or biomaterial to be deposited. Thus, each polymer or biomaterial molecule is surrounded or shielded by a large amount of solvent or matrix, reducing both thermal and photonic damage to the polymer or biomaterial in solution, during their laser-induced volatilization. Ideally, the solute molecules are entrained in the plume of matrix molecules leaving the frozen target due to collisions between the matrix and the embedded polymer or biomaterial molecules.

The substrates are typically at room temperature during the MAPLE deposition process, but they can be heated slightly to anneal the growing film. Typically, an excimer laser is used (KrF at 248 nm or ArF at 193 nm) with 10- to 30-ns pulse width, at repetition rates between 1 and 20 Hz, focused to a 1 to 10 mm^2 spot size on the target, although other types of lasers with wavelengths ranging from the visible to the infrared (IR) can be employed as well. The laser fluence at the target is typically set between 0.01 and 0.5 J/cm^2, depending on the solute material and solvent used. The depositions can be carried out at pressures ranging from vacuum to a few hundred millitorr and in the presence of inert or reactive background gases, in the same manner as conventional PLD.

The matrix solution is prepared by dissolving the organic or polymeric material in a solvent such as water, various types of alcohols, acetone, toluene, and so forth. To make a target, a few milliliters of the solution are flash frozen in a target die by submerging it in liquid nitrogen (LN_2). Once frozen, the MAPLE target is mounted on a cryogenically cooled rotating target holder with the open die and facing the laser. When a substrate is positioned directly in the path of the plume, a coating starts to deposit from the evaporated solute molecules, while the volatile solvent molecules, which have very low sticking coefficients, are evacuated by the pump in the deposition chamber.

One advantage of the MAPLE process is that it can easily be combined with noncontact shadow masks to limit the deposition to only those required areas on a substrate.

This is important for fragile substrates and is much less time-consuming than subsequent removal by patterning and etching.

Despite the great success achieved with the MAPLE technique for the deposition of polymers and biomaterials, this process is not without certain important drawbacks. First, the typical deposition rates that can be achieved with MAPLE are about an order of magnitude lower than those for conventional PLD.

Furthermore, the solvent molecules might be subject to photochemical reactions during their interaction with the laser pulse, which in some cases can result in the generation of highly reactive radicals that can alter the chemical structure and functionality of the solute polymer or biomaterial being deposited.

Another aspect that must be taken into consideration when using MAPLE is the resulting film surface morphology because, more often than not the surface morphology of the films tends to be rough and in some cases large droplets are present as well.

The film roughness not only depends on processing conditions but also on the type of polymer or organic being deposited and in the case of many biomaterials might not be modifiable due to the characteristic intrinsic arrangements of the molecular chains. For some applications, such as in biosensors, higher surface areas resulting from the rough film morphology might be desirable since they increase the area for analyte binding.

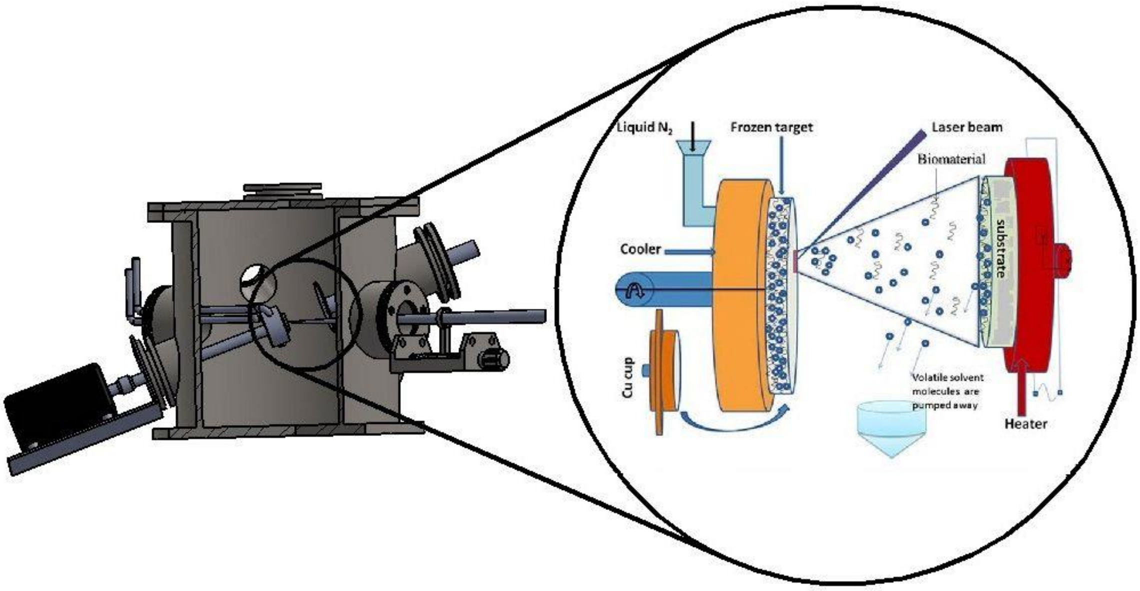

Figure 19 Schematic of the MAPLE technique: the vacuum chamber and detail of the target [177].

2. Aim of the research

This PhD thesis is aimed to develop new materials based on calcium phosphates functionalized with ions and molecules with anti-resorptive, anti-inflammatory and/or anti-bacteric properties for the local treatment of bone defects caused by injuries or pathologies.

Bone metabolism diseases are generated when there is an imbalance between the formation of new bone tissue and its resorption process. In turn, these two mechanisms depend on the interaction between osteoblast, cells responsible for the new bone formation, and osteoclast, which are responsible for the bone resorption. Calcium phosphates are excellent candidates for the preparation of biomaterials capable of supporting bone cell proliferation and promote osteogenic activity, and therefore the regeneration of bone tissue. Furthermore, such materials are susceptible to osteoclastic degradation, which promotes their complete replacement with new functional bone. The continuous aging of the population has led to a serious rise in the demand of orthopaedic implants, and in particular of materials able to couple the excellent biocompatibility and bioactivity of calcium phosphates with the therapeutic properties of functionalizing agents. Moreover, an ideal implant should be able to avoid bacterial colonization, which causes asepting loosening and infections and provokes implant failure.

On this basis, the program involves the following research lines:

a) functionalization of calcium phosphates with bisphosphonates

Bisphosphonates (BPs) are currently the major class of drugs used for the treatment of osteoporosis and other metabolic bone diseases such as Paget's disease, *osteogenesis imperfecta* and bone metastases [120,178]. However, their prolonged systemic administration has several side effects, including osteonecrosis of the jaw and atypical subtrochanteric fractures [179, 180]. Local administration at specific bone sites has been proposed as an alternative strategy to deliver N-BPs and avoid/reduce the potentially side-effects of their prolonged systemic use.

One of the objectives of this thesis is to study the role of composition and surface charge of hydroxyapatite on the adsorption and release mechanisms of risedronate. To this aim, different apatitic substrates, namely

HA with a partial substitution of zinc to calcium (ZnHA), HA and ZnHA functionalized with polyethyleneimine (HAPEI, ZnHAPEI), as well as HA as control material, have been submitted to interaction with risedronate. The investigation includes the study of the adsorption isotherms of the bisphosphonate on the different substrates, the physicochemical characterization of the products, the analysis of the process of drug release.

Functionalization of octacalcium phosphate with alendronate and zoledronate was performed through direct synthesis in aqueous solution in the presence of increasing concentration of the BPs. The results of the physicochemical characterization of the products allow to get useful information on the structural interaction between the calcium phosphate and the functionalizing molecules.

Moreover, a series of samples containing different amounts of calcium alendronate monohydrated and octacalcium phosphate have been utilized to verify the possibility to deposit thin films of the composite materials using Maple Assisted Pulsed Laser Evaporation, with the aim to realize coatings with anti-osteoporotic properties.

b) functionalization of calcium phosphates with quercetin

Flavonoids, which are widely spread in vegetables and fruits, find useful applications as anti-oxidant, anti-bacterial, anti-inflammatory and anti-viral agents [181]. In particular, quercetin has also been suggested to inhibit bone resorption in vitro and to exhibit chemo-preventive and/or chemotherapeutic properties [83, 182].

The interaction of quercetin with hydroxyapatite was investigated through different methods of synthesis, and through adsorption from solution. Moreover, the possibility to adsorb quercetin on alendronate functionalized hydroxyapatite was also investigated. The study was extended to a high soluble calcium phosphate, monetite, as well as to monetite with a partial substitution of strontium to calcium, both of which were proven to be able to adsorb the flavonoid. All the products were submitted to chemical, morphological and structural characterizations. In particular, the anti-oxidant properties of the different materials were investigated through evaluation of their radical scavenging activity.

c) calcium phosphates enriched with Ag Nanoparticles

In order to create materials with antimicrobial properties, octacalcium phosphate and α-tricalcium phosphate were used as supports for silver nanoparticles. In fact, silver ions and silver-based compounds are highly toxic to microorganisms which include 16 major species of bacteria [183, 184]. Deposition of Ag nanoparticles on the surfaces of the calcium phosphates was performed using polydopamine as functionalizing and reducing agents. The products were characterized using powder X-ray diffraction technique, scanning electron microscopy, ICP and thermogravimetric analyses.

3. Materials

3.1 Syntheses

3.1.1 Hydroxyapatite

The synthesis of HA was carried out in N_2 atmosphere using CO_2 free water. 50 ml of a 1.08 M $Ca(NO_3)_2•4H_2O$ solution (pH adjusted to 10 with NH_4OH) was heated at 90°C and 50 ml of 0.65 M $(NH_4)_2HPO_4$ solution was added drop-wise under stirring. The precipitate was maintained in contact with the reaction solution for 5 h at 90 °C under stirring, then centrifuged at 10,000 rpm for 10 min and repeatedly washed with CO_2-free distilled water. The product was dried at 37°C overnight [185].

3.1.1.1 Hydroxyapatite - Quercetin

The synthesis of HA in the presence of quercetin was carried out in a solution of ethanol and CO_2-free deionized water in an inert atmosphere (N_2) following two different procedures: (a) direct synthesis of HA and (b) phase transition from DCPA, a more soluble phase, that easily hydrolyzes into HA. The direct synthesis was performed through a modification of a classical method. In particular, the synthesis was carried out in the presence of different amounts of quercetin dihydrate (Sigma; water solubility < 4%) added into the $Ca(NO_3)_2•4H_2O$ solution hydro alcoholic (1/1 V/V) , namely 85 mg, 170 mg and 255 mg, which correspond to a final concentration of 2.8 mM, 5.6 mM and 8.4 mM respectively. The resulting solid samples were labeled as D0, D85, D170, and D255, where digits indicate the quantity (mg) of quercetin powder used in the specific preparation.

For the synthesis of monetite, 50 mL of a 0.65 M $(NH_4)_2HPO_4$ aqueous solution was added drop-wise to 50 mL of a 1.08 M Ca $(NO_3)_2$ * $4H_2O$ hydro alcoholic (1/1 V/V) solution maintained at 65°C. The pH of both solutions was not modified, keeping the spontaneous pH (about 5). After 6 days storage in solution, the precipitate was separated, washed and dried as reported above for the direct synthesis of HA. The same synthesis procedure was carried out in the presence of different amounts of quercetin dehydrate (Sigma) added into the $Ca(NO_3)_2•4H_2O$ solution, namely 85 mg, 170 mg and 255 mg. The corresponding samples were labeled as MON0, MON85, MON170, and MON255. Phase transition from monetite to HA was obtained by a modification of the last part of the procedure followed for the synthesis of monetite: after keeping the precipitates in contact with the solution at 65°C under stirring for 6 days, the pH of the reaction mixture was adjusted to 9 with ammonia solution 25% and the temperature raised to 90°C. After 5 h under stirring, the reaction products were centrifuged at 10,000 rpm for ten minutes and repeatedly washed with CO2-free deionized water. The solid samples were dried at 37°C and labeled as T0, T85, T170, and T255, where digits indicate the quantity of quercetin powder used in the specific preparation [93].

3.1.1.2 Hydroxyapatite - Poly(etyhlenimine)

Hydroxyapatite at different poly(ethylenimine) contents was obtained by adding PEI to the $Ca(NO_3)_2•4H_2O$ solution, before adjusting the pH to 10 with NH_4OH. Poly(ethylenimine) solution (Aldrich, MW~2000) was used. Concentrations of PEI were 1, 2 and 4 M calculated on the final volume, the obtained samples were labeled as HAPEI 1, HAPEI 2 and HAPEI 4. [186]

3.1.1.3 Hydroxyapatite – Alendronate

Following the standard synthesis of hydroxyapatite, after the addition of 25 ml of phosphate solution, 25 ml of alendronate solution 14mM (calculated on final volume) were dropped under stirring in the reaction vessel. The precipitate was maintained in contact with the reaction solution for 5 h at 90°C under stirring, then centrifuged at 10,000 rpm for 10 min and repeatedly washed with CO2-free distilled water. The product was dried at 37°C overnight [187], named HAAL.

3.1.1.4 Zinc – Hydroxyapatite (ZnHA)

Zn substituted hydroxyapatite was synthesized following the hydroxyapatite experimental procedure, but the cationic solution was prepared by dissolving the appropriate amounts of $Ca(NO_3)_2•4H_2O$ and

$Zn(NO_3)_2 \bullet 6H_2O$ in CO_2-free deionized water before adjusting the pH to 10 with NH_4OH. The total cationic concentration was 1.08 M, and the Zn/(Ca + Zn) molar ratio was 0.1 [60].

3.1.2 Octacalcium Phosphate

The synthesis of OCP was carried out by dropwise addition of 250 ml of 0.04 M $Ca(CH_3COO)_2$ (over a period of 50 min) into 750 ml of a phosphate solution containing 5 mmol of Na_2HPO_4 and 5 mmol of NaH_2PO_4 at starting pH 5. The reaction was carried out at 70°C under mechanical stirring. After 30 min the precipitate was filtered, repeatedly washed with distilled water and dried at 37°C [188].

3.1.2.1 Alendronate/Zoledronate - Octacalcium Phosphate

Similarly, the synthesis of OCP in the presence of Zoledronate was carried out by dropwise addition of 250 ml $Ca(CH_3COO)_2$ solution into 700 ml of a phosphate solution containing 5 mmol of Na_2HPO_4 and 5 mmol of NaH_2PO_4 at starting pH 5; afterwards the resulting slurry was stored under stirring for 30 min and then 50 ml of the bisphosphonate solution was added dropwise over a period of 10 min. Immediately after the addition of Zoledronate, the precipitate was filtered, repeatedly washed with distilled water and dried at 37°C. Zoledronate concentration was in the range 0.1 – 1.5 mM, calculated on the final volume.

The synthesis of OCP in the presence of Alendronate was performed in the same condition of the modified synthesis of OCP-Zoledronate. Alendronate concentration was in the range 0.1 - 1.5 mM, calculated on the final volume [189].

Samples were labeled as OALXX,in the case of Alendronate, or OZOLXX, in the case of Zoledronate, where XX indicates the concentration of BP in solution (expressed as mM).

3.1.3 α-TriCalcium Phosphate

α-TCP was obtained by solid-state reaction of a mixture of $CaCO_3$ and $CaHPO_4 \cdot 2H_2O$ in the molar ratio of 1:2 at 1300°C for 5 hours [190].

3.1.4 DiCalcium Phosphate Anydrous

The synthesis of monetite was carried out using 50 ml of a 1.08 M $Ca(NO_3)_2 \bullet 4H_2O$ solution heated at 90°C and 50 ml of 0.65 M $(NH_4)_2HPO_4$ solution that was added drop-wise under stirring. The precipitate was maintained in contact with the reaction solution for 5 h at 90 °C under stirring, then centrifuged at 10,000 rpm for 10 min and repeatedly washed with distilled water. The product was dried at 37°C overnight [93].

3.1.4.1 DiCalcium Phosphate Anydrous substituted with Strontium (SrDCPA)

Sr substituted monetite was synthesized following the experimental procedure used for the synthesis of monetite, but including Sr ion in the cationic solution, which was prepared by dissolving the appropriate amounts of $Ca(NO_3)_2 \bullet 4H_2O$ and $Sr(NO_3)_2 \bullet 5H_2O$ in CO_2-free deionized water before adjusting the pH to 10 with NH_4OH. The total cationic concentration was 1.08 M, and the Sr/(Ca + Sr) molar ratio was 0.2.

3.2 <u>Adsorption</u>

3.2.1 ZnHA – Polyethylenimime

Absorption of PEI on pre-formed hydroxyapatite substituted with zinc at 10% (ZnHA10) was performed by soaking ZnHA10 powder (100mg) in an aqueous solution of 4 M PEI, under stirring for 24 hours. Then, the solid was centrifuged at 10,000 rpm for ten minutes and washed with deionized water. Finally, the powder was dried at 37 ° C and the sample was labeled as ZnHAPEI.

3.2.2 Risedronate adsorption on different substrates

Adsorption experiments were carried out at physiological temperature (37 ± 1° C), by dispersing 50 mg of powder (HA / HAPEI / ZnHA / ZnHAPEI) in 5 mL of risedronate solutions (concentration ranging from 0 to 3 mM) in a polyethylene tube. The latter were prepared by dissolving the appropriate amount of risedronate in an aqueous 1 mM KCl solution (standard solution); the pH of the obtained solutions was adjusted to 7.4 using hydrochloric acid and potassium hydroxide solutions. After sonication for 1 min, the suspensions were incubated for 1 h without stirring and centrifuged for 10 min at 5000 rpm. This equilibration time was previously determined from kinetic experiments using risedronate concentrations of 0.86 mM. Blanks containing only the apatitic powders, prepared and incubated in the KCl solutions, were used as controls. After centrifugation, the solid products were washed with deionised water and dried at 37°C overnight. The supernatants were filtrated on 0.2 µm Millipore filters. The samples obtained by using the following supports HA,HAPEI, ZnHA, ZnHAPEI after risedronate adsorption were labeled, respectively, as HABP, HAPEIBP, ZnHABP and ZnHAPEIBP. [186]

3.2.3 Calcium Phosphate – Quercetin

Adsorption of quercetin on pre-formed HA, HAAL, DCPA and SrDCPA were carried out by soaking 500 mg of powders in 20 ml of 6 mM hydroalcolic solution of quercetin (H_2O/EtOH in the ratio 50/50), under stirring for 24, 48 and 72 hours at 37°. Then the solid products were filtered and washed with deionized water and dried at 37° overnight. The obtained samples were labeled HA24Q, HA48Q and HA72Q. The same format was used also for the other supports.

3.2.4 Calcium phosphates-Silver Nanoparticles (AgNPs)

Silver nanoparticles were loaded on octacalcium phosphate and on α-tricalcium phosphate previously functionalized with a coating of polydopamine.

The final materials were obtained in two steps of functionalization. In the first one, the powders were put in contact in a 2mg/ml solution of TRIS buffer and dopamine hydrochloride at pH 8.5, under stirring. After 2 hours the solution was filtered and the obtained solid repeatedly washed with distilled water and dried at 37°C overnight. The obtained samples were labeled as OCPd and α-TCPd.

In the second step, 20ml of $AgNO_3$ solution, at different concentration (1mM, 5mM and 10mM), and 20ml of sodium citrate solution 13mM, at room temperature under stirring, were added simultaneously to a becker containing the powders functionalised with dopamine. After one hour the solid was filtered repeatedly washed with distilled water and dried at 37°C overnight. The final products were named OCPd Ag1, OCPd Ag5, OCPd Ag10 and α-TCPd Ag1, α-TCPd Ag5, α-TCPd Ag10.

*3.3 **Release Tests***

3.3.1 BPs release from OCPZOL and OCPAL

Bisphosphonate release tests were performed on disk-shaped samples (Ø= 6.0 mm). Each disk was prepared by pressing 60 mg of powder into cylindrical moulds by using a standard evacuable pellet die (Hellma).

The obtained disks were immersed in 2 mL of 0.1 M Phosphate Buffer Solution (PBS) at pH of 7.4 for increasing time from 2 hours up to 7 days. The content of bisphosphonate was measured spectrophotometrically on the solid residue via complex formation with Fe(III) ions [191] using a Varian Cary50Bio instrument (λ= 290 nm).

3.3.2 Risedronate release from apatitic samples

Risedronate release profiles were obtained with a flow through cells system with 12 mm cells (6 mL) and peristaltic pump. In all experiments, laminar flow was used with one glass beads layer covered with each BP-functionalized apatitic sample, mixed with 2 g of glass beads. Different weights were utilized for the analysis of the different materials so that all the samples contained the same amount of adsorbed BP (about 1.8 $\mu mol/m^2$). The release tests were carried out at 37.0 ± 0.5 °C under sink conditions according to European Pharmacopoeia guidelines. The dissolution medium was deionized water pumped through the column at a flow rate of 9 ml/min. A closed system was used, recycling 50 ml of dissolution medium. Periodically, fractions of 5 ml were collected and risedronate content was determined by UV spectroscopy at 262 nm. The same volume of dissolution medium was replaced back after each sampling in order to maintain constant volume and sink conditions. Each release analysis was performed in triplicate.

3.4 ***Thin Film deposition OctaCalcium Phosphate- Alendronate***

Disk-shaped Ti substrates (12 mm diameter and 0.5 mm thick) were mechanically polished and submitted to chemical etching before being used as collectors. They were clean in ultrasonic sequential baths of acetone, alcohol and deionized water. For the preparation of one target used in MAPLE experiments, deionized H_2O based solution containing 0.12 g of OCP powder was suspended in 10 ml and subsequently stirred, homogenized and frozen in a special cop-per holder at 77 K in liquid nitrogen. The holder containing the solid target was then mounted inside a vacuum chamber. During exposure to multipulse laser irradiation, the target was maintained frozen by continuous liquid nitrogen flow inside a supporting cooler device and continuously rotated with 80 rpm to avoid drilling and improve the overall quality of the deposited films. A pulsed KrF* laser source(λ= 248 nm, _FWHM≤ 25 ns) operating at 5 Hz was employed for their radiation of the target. 20,000 subsequent pulses were applied at an incident laser fluence of 0.73 J cm^{-2} for the synthesis of each assembly (the corresponding pulse energy was of 280 mJ). The deposition was carried out in a residual pressure of 13 Pa. The substrate was facing the target at a separation distance of about 4 cm, while its temperature was kept constant at 30◦C during deposition. Identical MAPLE conditions were applied for the deposition of AL8 andAL20 powders. The deposited coatings were labeled cOCP, cAL8, and cAL20 [189].

AL8 andAL20 were prepared as follows: reaction of OCP and AL was carried out in bidistilled water in the presence of two different concentrations of sodium alendronate trihydrate (Chemos), that is 8 and 20 mM. Resulting solid samples have been labeled AL8 and AL20, respectively. The reaction was performed on 500 mg OCP/250 ml solution at 30◦C, maintained under stirring for 72 h. Then the products were centrifuged at 5000 rpm for 10 min, repeatedly washed with double distilled water and dried at 37◦C [189].

4. Methods

4.1 X-Ray Diffraction

X-ray diffraction analysis was carried out by means of a PANalytical X'Pert PRO powder diffractometer equipped with a fast X'Celerator detector (40 mA, 40 kV). For phase identification the 2θ range was investigated from 3 to 60 2θ degrees with a step size of 0.1 and time/step of 100 s. To evaluate the coherence lengths of the crystals, further X-ray powder data were collected in the relevant regions of 2θ by means of step scans with a fixed counting time of 100 s for each 0.033/step. Data used for cell parameters calculations were collected from 10 to 60 2θ degrees counting for 400 s at each 0.033 (2θ) and processed with the Rietveld refinement analysis.

For analysis of thin films deposited by means of MAPLE, the explored 2 θ° range was from 3 to 12°(2 θ)with a step size of 0.05° and time/step of 3000 s.

4.1.1 Scherrer analysis

For hydroxyapatite samples, the line broadening of the 002 and 310 reflections was used to evaluate the length of the coherent domains (hkl) along the c-axis and along a direction perpendicular to it.

For octacalcium phosphate samples, a qualitative estimation of the size of the coherently scattering domains was performed from the line broadening of the (100), (002) and (010) reflections. $\tau_{h\,k\,l}$ values were calculated from the widths at half maximum intensity ($\beta_{1/2}$) using the Scherrer equation [192]

$$\tau_{\mathrm{hkl}} = \frac{k * \lambda}{\beta_{\frac{1}{2}} * cos\theta}$$

where λ is the wavelength, θ the diffraction angle and K a constant depending on crystal habit (chosen as 0.9). The silicon standard peak 111 was used to evaluate the instrumental broadening.

4.1.2 Rietveld refinement analysis

In the Rietveld refimement the experimental pattern is calculated through a mathematical function, since the relation between the atom position and the intensity at each point of the powder profile are known. The pattern is reproduced by assuming it to be a sum of a number of well shaped Bragg reflections centered in their respective Bragg angle positions. A structural model is necessary in order to calculate the corresponding intensity at each $y_{i\ calc}$ step of the pattern, according to the equation (I):

$$y_{i\ calc}(k) = s \sum_k m_k L_k [F_k]^2 G\,(2\theta_i - 2\theta_k) P_k A_k + y_{ib} \qquad \text{(I)}$$

Where s is the scale factor, m is multiplicity factor, L is the Lorenz-polarization factor for the k reflection, F is the structure factor, G the reflection profile function, 2θ k is the calculated position of the Bragg peak, P is the preferred orientation factor, A is the adsorption factor, y_{ib} is the background value at point i.

The purpose of this procedure is to find the best possible agreement between the observed pattern and a calculated profile. In order to get this goal the residual S:

$$S = \sum_i w_i [(y_{i\ obs} - y_{i\ calc})]^2 \qquad \text{(II)}$$

Where $w_i = 1/y_{iobs}$, y_{iobs} is the observed intensity at the i-th step and y_i calc is the calculated intensity at i-th step.

During this procedure two sets of parameters are varied:

-non structural parameters, generally refined at the beginning of the procedure (scale factor, zero shift, background parameters, profile shape, asymmetry).

-structural parameters, refined in the last steps of the procedure (unit cell parameters, atom position, occupation factor)

This order could however change in according with the observed results on the calculated pattern after each step.

4.2 __Fourier Transform Infra-Red and Raman Spectroscopy__

For the IR analysis, 1 mg of the samples were carefully mixed with KBr (250 mg, infrared grade) and pelletized under a pressure of 10 tons for 40 seconds. The pellets were analyzed using a Nicolet 380 FTIR spectrophotometer to collect 64 scans in the range 4000 – 400 cm^{-1} at a resolution of 4 cm^{-1}.

Raman spectra of the samples were generated on a Horiba, Jobin-Yvon Labram HR800 confocal microspectrometer, equipped with a helium–neon LASER (λ = 632.82 nm). The spectral resolution was 2 cm^{-1} , the laser power was 2 mW and integration times varied from 30 to 120 s. All spectra were recorded over a wavelength range of 200–1800 cm^{-1}. Three spectral accumulations were averaged.

4.3 __Inductively Coupled Plasma__

The quantification of Ag was performed using a quadrupole mass spectrometer with plasma source ICP MS XSeries Thermo Fisher Scientific. The samples were prepared by dissolving 10 mg of powders in water/ methanol solution 1/1 V/V. 5 ml were taken and added in 50 ml of 5% nitric acid solution.

4.4 __Microscopy__

Most morphological investigation was performed by scanning electron microscopy (SEM) using a Philips XL20 instrument operating at 15 kV. The samples were sputter-coated with Au before analyses. OCP functionalized with bisphosphonates were examined using a Phenom ProX desktop-scanning electron microscope at beam acceleration voltage of 10 kV. In this case the samples were observed as prepared and not sputter coated before examination. The ImageJ® picture analyzer software was used to estimate the mean crystals dimensions, averaging the measurements over at least 100 data points per sample.

For TEM investigations, a drop of sonicated powder suspension in ethanol was transferred onto holey carbon foils supported on conventional copper microgrids. A Philips CM100 transmission electron microscope, operating at 80 kV was used.

For AFM imaging a Veeco Nanoscope 3D instrument was used. The samples were analyzed in tapping mode using a E scanner (- maximum scan size 15 μm) and phosphorus (n) doped silicon probes (spring constant 20–80 N/m; resonance frequency 250– 290 kHz; nominal tip radius < 10 nm). Roughness parameters, namely arithmetic mean roughness (Ra), root-square roughness (Rq), and the vertical distance between the highest and lowest points within the evaluation length (Rt), were recorded.

4.5 <u>Surface Area Analysis by Gas Adsorption</u>

The specific surface area was measured using a Carlo Erba Sorpty 1750 BET analyzer using constant volume N_2 absorption with desorption at 80 °C.

4.6 <u>Uv-Vis Spectroscopy</u>

Bisphosphonate content was determined spectrophotometrically via complex formation with Fe(III) ions using a Varian Cary50Bio instrument (λ= 290 nm).

Quercetin content was determined spectrophotometrically using a Varian Cary50Bio instrument (λ=256 and 373 nm)

4.7 <u>Zeta Potential Measurement</u>

Zeta potential was measured using a Malvern Instruments Zetasizer Nano. 5 mg of powder sample was suspended in 50 mL of MilliQ water after sonication for 2 minutes. Each analysis was performed in triplicate.

4.8 Static Contact Angle Measurement

Static contact angle measurements were performed on disk shaped samples (Ø = 13.0 mm). Each disk was prepared by pressing 100 mg of powder into cylindrical molds by using a standard evacuable pellet die (Hellma). A KSV CAM101 instrument was used under ambient conditions by recording the side profiles of deionized water drops for image analysis. The shape of the drop was recorded in a time range of 0–60 s, by collecting an image every 0.033 s. At least six drops were observed for each sample.

4.9 Thermogravimetric Analysis

Thermogravimetric analysis was carried out using a Perkin- Elmer TGA-7. Heating was performed in a platinum crucible in air flow (20 cm^3/min) at a rate of 10 °C/min up to 900 °C. The samples weights were in the range 5–10 mg. Results from this analysis represent the mean value of determinations for three different samples of each composition.

4.10 Radical Scavenging Activity

Antioxidant activity was determined based on the Quercetin ability to act as radical scavengers toward the stable 2,2-diphenyl- 1-picrylhydrazyl free radical ($DPPH^{\cdot}$). This method previously described by Gulcin [193] was used with slight modifications. Briefly, 50 µL of QUE and obtained samples in the concentration range 10.0–100.0 µM were added to 3 mL of $DPPH^{\cdot}$ saturated ethanol/water (20/80 V/V) solution. Samples were kept under magnetic stirring for 10 min at RT in darkness to reach the steady-state condition; after samples centrifuging, absorbance readings were taken at 515 nm. The radical scavenging activity (RSA) was determined through the following equation:

$$\% \text{ RSA} = (A_0 - A_x)/A_0 * 100$$

whereby A_0 is the absorbance of the control (containing DPPH$^{\cdot}$ solution without quercetin), and A_x is the absorbance in the presence of QUE or of obtained samples.

5. Results and Discussion

5.1 Study of the antioxidant and bone repair properties of quercetin functionalized - hydroxyapatite

Functionalization of hydroxyapatite with quercetin was carried out in order to get new materials for bone repair through local administration of the flavonoid [93]. Quercetin is a powerful antioxidant and anti-inflammatory flavonoid with the capability to prevent bone loss.

HA was synthesized in presence of different concentrations of quercetin according to two different procedures: direct synthesis and phase transition from monetite.

The details of the procedures utilized to prepare the two sets of samples illustrated in the scheme in Figure 20 are reported in chapter *Materials*, paragraph 3.1.1.1.

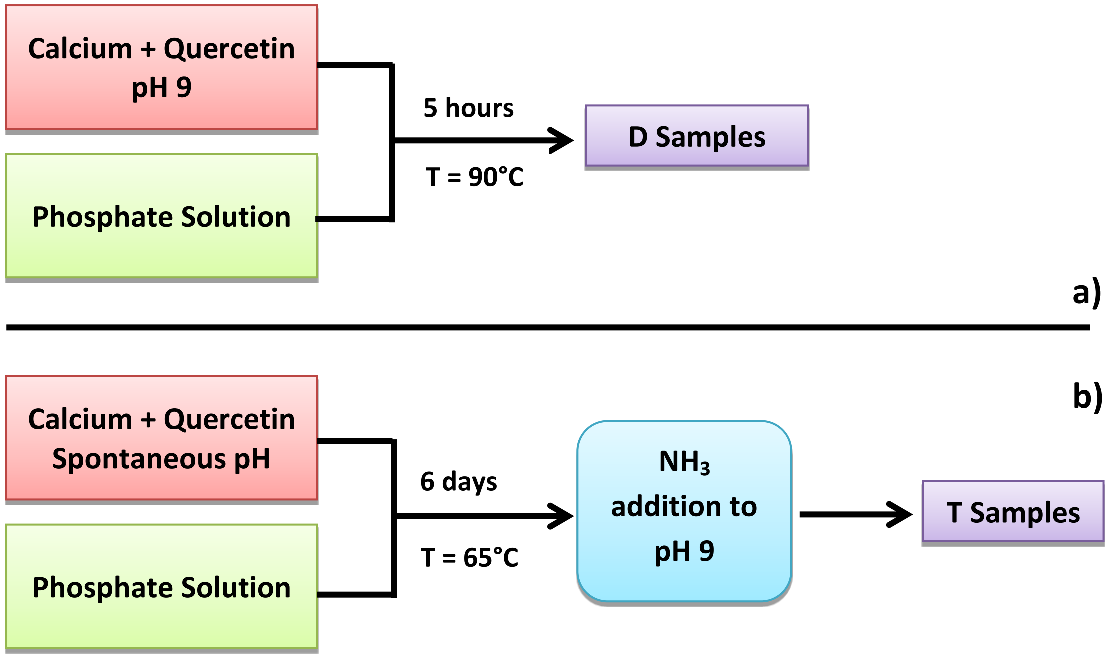

Figure 20 Scheme of the synthesis procedures: a) direct synthesis of HA b) synthesis of monetite, followed by conversion to HA.

The relative amount of quercetin in the different samples has been evaluated by thermogravimetric analysis (Figure 21). The results show an increase of quercetin content as the flavonoid concentration in the synthesis solution increases, up to a maximum value of 3.1 wt% (Table 3).

The powder XRD patterns of all the samples obtained by direct synthesis show a number of diffraction peaks characteristic of the HA, which is present as unique crystalline phase (Figure 22). The broadening of the diffraction reflections grows with quercetin content, suggesting a reduction of crystallinity with composition. To better evaluate the contribution of this modification in the peaks shape, the length of coherently scattering domains (τ_{hkl}) has been calculated using the Sherrer equation and considering a negligible microstrain. In particular, it has been evaluated τ_{002}, which is related to the mean crystallite size along the *c*-axis, and τ_{310}, which refers to the mean crystallite size along a direction perpendicular to *c*-axis. The decrease of the mean crystallite size, along both crystallographic directions, with the increasing of quercetin content indicates that the presence of the flavonoid in solution inhibits the crystallization of HA.

Table 3 Coherent lengths (τhkl) of the perfect crystalline domains in the direction normal to (002) and to (310) planes calculated using the Scherrer method; lattice parameters calculated using Rietveld method, Specific Surfaces Area, amount of quercetin associated to HA [93]

Samples	**τ_{002} (Å)**	**τ_{310} (Å)**	***a* (Å)**	***b* (Å)**	**SSA (m^2/g)**	**Que (wt%)**
D0	471(1)	222(1)	9.428(2)	6.880(2)	66(7)	-
D85	429(3)	200(1)	9.436(4)	6.880(2)	70(7)	1.0(3)
D170	387(1)	162(1)	9.435(1)	6.881(2)	92(9)	2.4(5)
D255	357(1)	96(1)	9.436(2)	6.877(3)	120(11)	3.1(5)

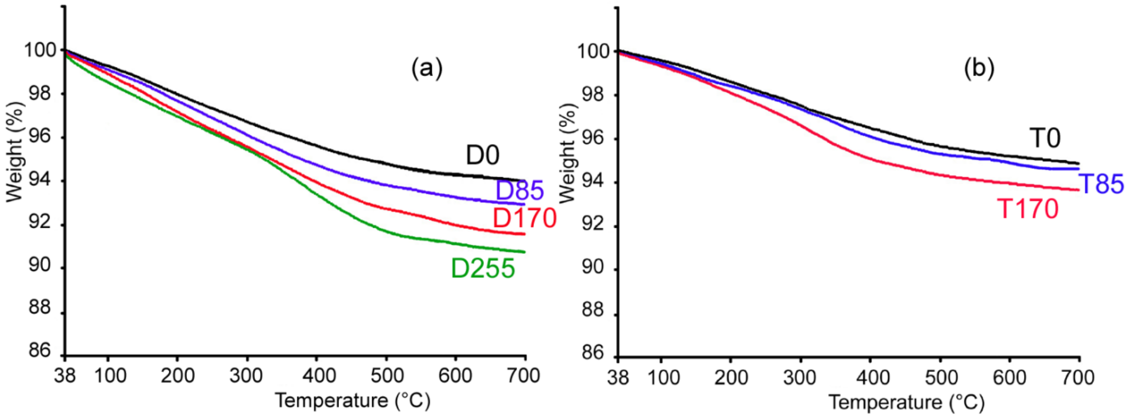

Figure 21 Thermogravimetric plots of the products obtained by (a) direct synthesis, and (b) phase transition [93].

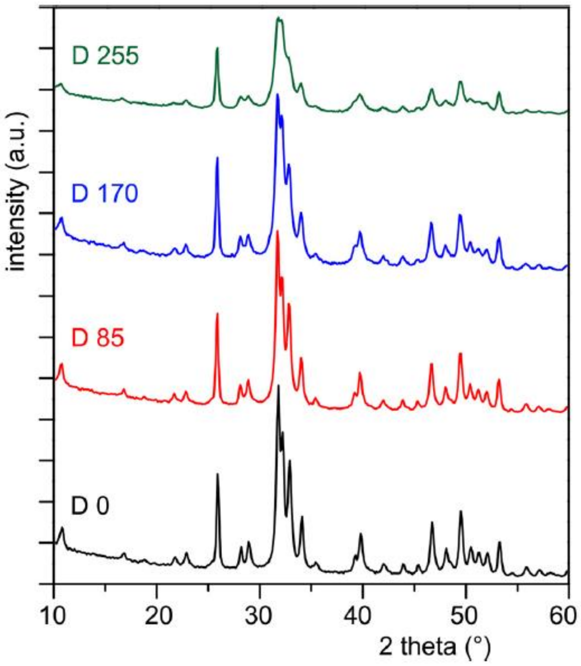

Figure 22 Powder XRD patterns of the products obtained by direct synthesis of HA in presence of different amounts of quercetin [93]

TEM images (Figure 23) show that the crystals of sample D0 (HA reference) are characterized by a plate like morphology with well defined edges, elongated along one preferential direction that corresponds to the crystallographic *c* axis. The mean dimensions are about 40 x 20 nm. With the presence of quercetin, the crystals become smaller and thinner, and display more homogeneous dimensions. The presence of quercetin, instead, does not change significantly the morphology of the crystals.

Coherently with the decrease of crystal dimensions, the surfaces area increases from 66 m^2/g to 120 m^2/g on passing from sample D0 to D255 (Table 3).

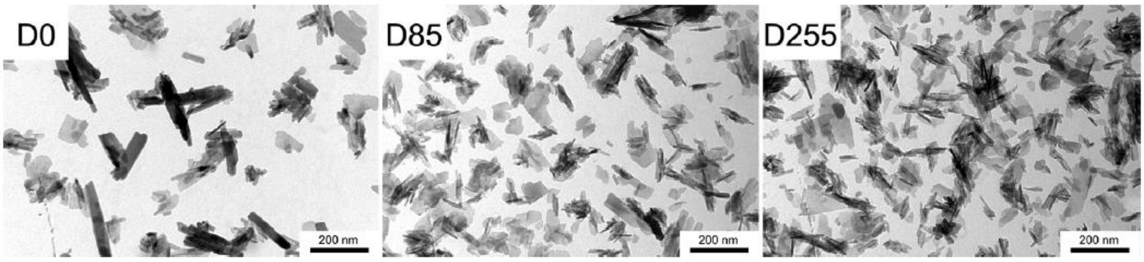

Figure 23 TEM images of the products obtained by direct synthesis (D0, D85 and D255) scale bars = 200 nm [93].

The presence in the composite nanocrystals of a hydrophobic molecule, such as quercetin, does not affect the hydrophilic behavior of HA, as supported by the values of the contact angle: the angle of the water droplet, put in contact on the sample surface, passes from 27 ± 1° for D0 to an average value of 32 ± 1° for the quercetin containing samples. After 4 seconds, water was always completely spread on the surface of the samples.

5.1.1 Composite crystals obtained through phase transition

In order to study the possible pH effect on quercetin stability and activity, an alternative approach has been developed for the synthesis of quercetin modified hydroxyapatite. The reagents are the same as those used in the procedure of direct synthesis but the pH is not adjusted, leaving the spontaneous pH of the solutions (about 4) and at the temperature of 65°C. The precipitates obtained after 6 days storage in solution are constituted of DCPA as unique crystalline phase both in absence and in presence of quercetin. After 6 days storage in solution, the pH is adjusted to 9 and the temperature is raised to 90°C, which provokes the transformation of DCPA in HA. Indeed DCPA, as well as other orthophosphates, easily hydrolyzes to the thermodynamically more stable HA phase, according to a transition mechanism that is favored by basic conditions [194].

The powder XRD patterns of samples T0, T85 and T170, show the main peaks of crystalline HA. On the contrary, the most intense peaks in the XRD pattern of the sample T255 are due to DCPA, indicating that at this concentration quercetin inhibits monetite transformation in HA (Figure 24).

The XRD peaks of the apatitic samples are very sharp and, accordingly, the values of the mean values of the length of coherently scattering domains, reported in Table 4, are relatively high and do not exhibit a relevant reduction on increasing quercetin content. At the same way, the lattice parameters do not show significant variation with composition when compared to HA reference (Table 4).

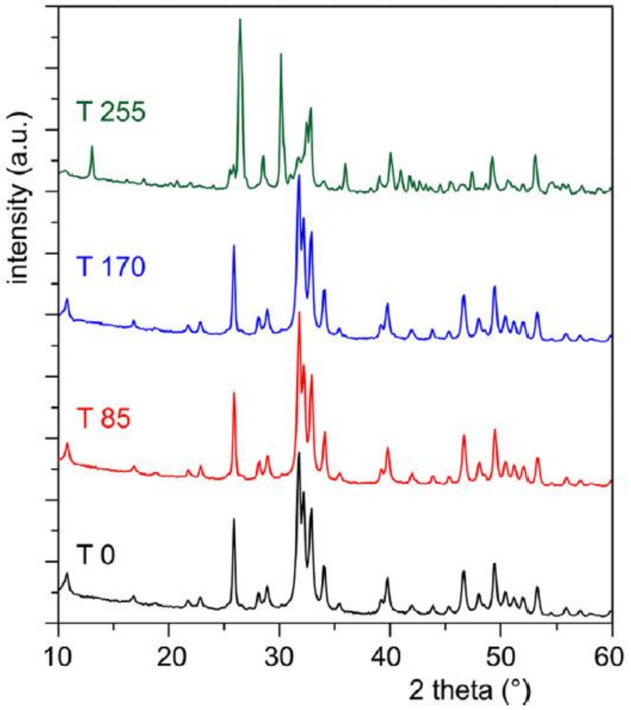

Figure 24 Powder XRD patterns of the products obtained through phase transition [93].

The amount of quercetin adsorbed on T samples increases up to about 1.3 wt%, a lower value with respect to the samples obtained by direct synthesis (Table 4).

Table 4 Coherent lengths (τhkl) of the perfect crystalline domains in the direction normal to (002) and to (310) planes calculated using the Scherrer method; lattice parameters calculated using Rietveld method, Specific Surfaces Area, amount of quercetin associated to inorganic phase [93].

Samples	**τ_{002} (Å)**	**τ_{310} (Å)**	***a* (Å)**	***b* (Å)**	**SSA (m^2/g)**	**Que (wt%)**
T0	570(1)	298(1)	9.4404(4)	6.8848(4)	16(2)	-
T85	565(1)	294(1)	9.4294(4)	6.8758(4)	16(2)	0.5(3)
T170	556(1)	288(1)	9.4377(5)	6.8818(4)	16(2)	1.3(4)

TEM images reported in Figure 6 show that samples constituted of big rod-like crystals with well defined edges and elongated along a preferential direction. The mean dimensions are 300 x 40 nm and the mean surface area is 16 m^2/g at variance with what found for the samples prepared by direct synthesis, the presence of quercetin does not affect significantly the morphology and the dimension of the crystals.

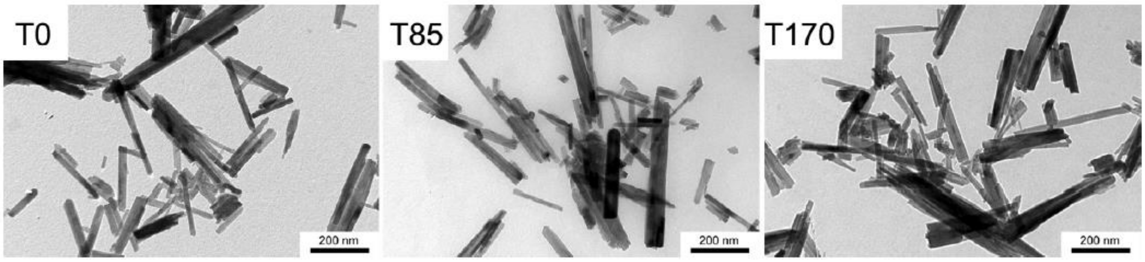

Figure 25 TEM images of the products obtained by phase transition (T0, T85 and T170) [93].

On the other hand, as for the samples obtained by direct synthesis, quercetin does not affect the hydrophilic behavior of the composite crystals, which exhibit contact angle values from 26 ± 1° to 32 ± 1° after 0.33 s the water droplet contacted the surface.

The results of full profile fitting of the XRD patterns, for composite crystals obtained by direct synthesis and by phase transition, show that there is no significant amount of amorphous material in both cases. Moreover the cell parameters, as commented before, do not vary with the composition, suggesting that HA interaction with quercetin does not provoke relevant structural modifications. Considering this information, it was possible to hypothesize a possible interaction between HA and quercetin dihydrate considering the full atomic position set, occupancy factors and thermal parameters.

In fact in the molecular structure of quercetin, the distances oxygen-oxygen are around 6.4/6.6 nm, which fit well with the calcium periodicity of HA along the axis *c*. According to this structural data, the oxygens of quercetin may interact with calcium (I) of hydroxyapatite, without significantly affecting its structure (Figure 26).

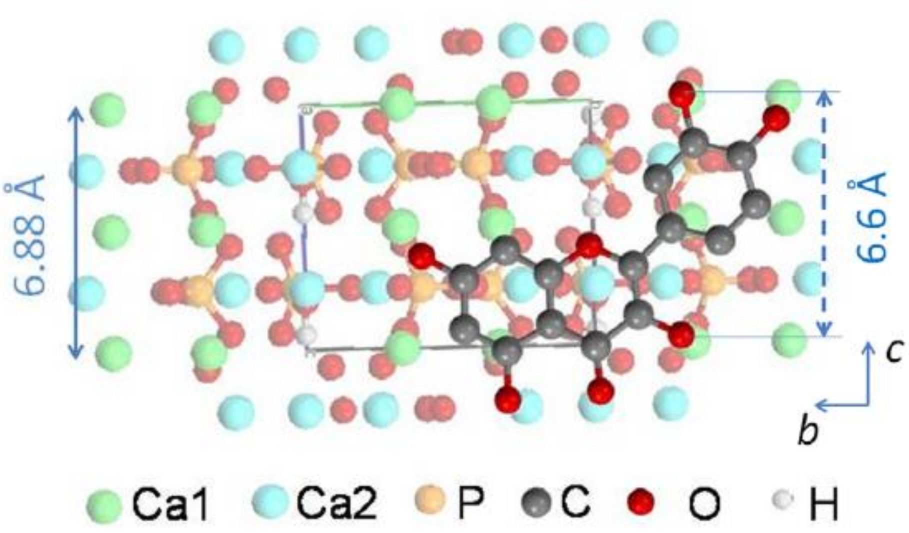

Figure 26 Structural model showing a possible interaction between HA and quercetin [93].

5.1.2 Quercetin oxidation

The photographic images reported in Figure 8 allow to appreciate the color change of the final products as a function of the type of synthesis procedure and of flavonoid concentration.

Figure 27 Photographic images of the different products [93].

Table 5 Effects of heat treatment, pH and storage condition on quercetin content [195].

Food processing	Food product	Processing condition	Results
Thermal	Bean	Atmospheric (100°C) and pressure boiling(121°C) with and without soaking	70% degradation of quercetin [197]
	Onion bulbs	Atmospheric boiling (100°C) for 60 min.	43% degradation of quercetin [198]
	Solutions	Heating at 97°C for 240 min under pH 8, N2	15% degradation of quercetin [199]
Alcali or acid	Grapefruits juices	Heating at 80°C for 91 sec	17% degradation of quercetin [200]
	Solutions	Treatment with different pH values (pH 5 and 8) for 300 min	100% degradation of quercetin [201]
	Solutions	Treatment with different pH values (2, 7, 10) for 96 h	100% degradation of quercetin [202]
Metal ions	Solutions	Quercetin and $CuCl_2$	Increase antioxidant activity [203]
	Solutions	In the presence of Cr^{3+}	Increase DPPH radical scavenging activity [204]
	Solutions	In the presence of Sn^{2+}	Decrease DPPH radical scavenging activity [205]

Compared to the white reference HA, the products obtained by direct synthesis in the presence of quercetin display a yellow-brownish color which becomes darker with the increasing of the flavonoid content. On the other hand, in the products obtained through phase transition, the color passes from yellow to dark yellow as a function of composition. This color variation might be due to quercetin oxidation, which would be provoked by the relatively high pH of the synthesis medium. The different color range of the products, obtained with the two synthesis methods, might suggest that the quercetin has undergone different mechanisms of oxidation and/or degradation.

UV-Vis spectrum of quercetin shows two characteristic bands at 256 and 373 nm that are due to the $\pi \rightarrow \pi^*$ transitions at rings A and B respectively. Upon oxidation, these bands begin to decrease and a further band appears at 295-330 nm. In the experimental UV-Vis absorption spectrum of sample D170, the band at 373 nm is no more appreciable, whereas the relative intensity of the 256 nm band appears significantly reduced, in agreement with a degradation of quercetin (Figure 28).

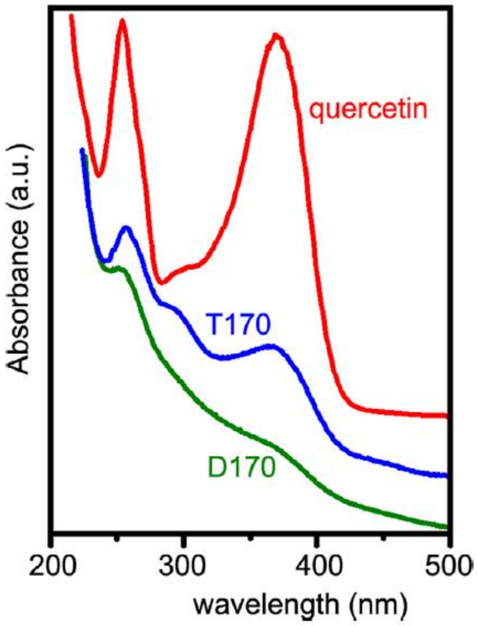

Figure 28 UV–vis absorption spectra of pure quercetin, D170 and T170 [93].

In literature several processes have been proposed for the oxidation of quercetin; the one proposed by Wang et al [195] might be eligible for these samples. Quercetin can be oxidized into various products, namely quercetin-quinones, which include one ortho-quinone and three quinone methides (Figure 29). A cleavage of quercetin leading to a protocatechuic acidis is one of the possible degradation of the cynnamoil system.

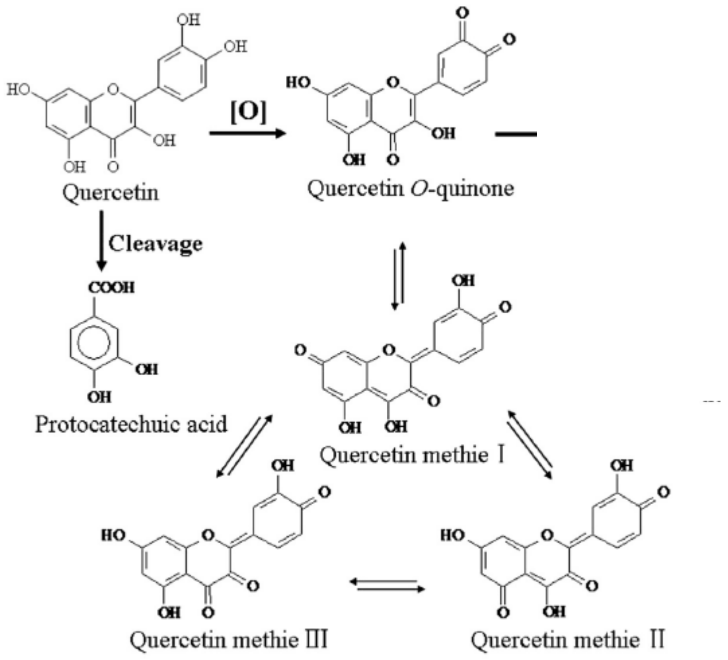

Figure 29 Oxidation and degradation pathways of quercetin [195]

5.1.3 Radical scavenging activity

RSA of the different samples are compared with that of pure quercetin, in the following figure.

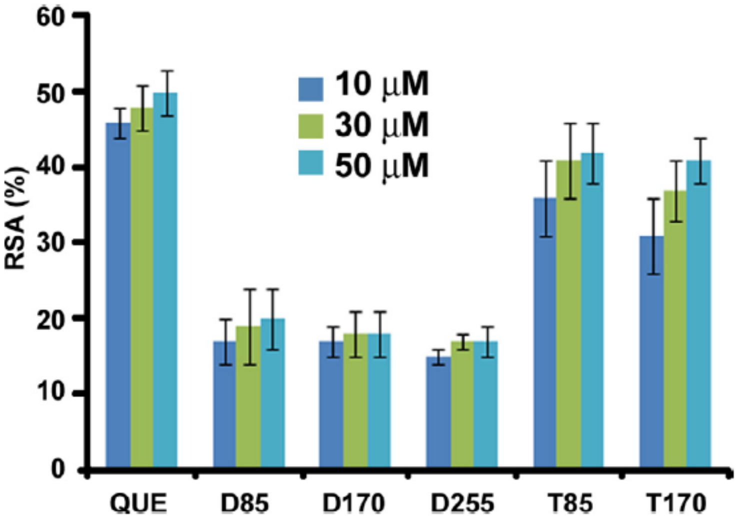

Figure 30 Comparison between the antiradical activity, expressed as% RSA, of the different products and that of pure quercetin. Each bar represents the mean standard deviation of three independent measurements [93].

Pure quercetin exhibits RSA values varying from 45% to 50% as a function of concentration, in good agreement with previous data [196]. RSA values of the products obtained through direct synthesis are significantly reduced with respect to those of pure quercetin, whereas those obtained for the products obtained through phase transition are still very high, reaching levels of about 40%, as shown in Figure 30. These data confirm that the antioxidant activity of quercetin is maintained in the apatitic samples obtained through phase transition, whereas it is remarkably reduced in the samples prepared by direct synthesis, as shown by the results of spectrophotometric analysis.

On the basis of these results, which demonstrate the good radical scavenging activity of the products synthesized through phase transition, in vitro study was performed on samples T85 and T170, as well as on T0 as control sample.

The study was performed utilizing an innovative *in vitro* model, which involves co-culture of osteoblast, osteoclast and endothelial cells. Osteogenesis is closely related to angiogenesis, since a suitable angiogenic response is essential for successful bone repair. As a consequence, a triculture model involving the interplay of osteoblast, osteoclast and endothelial cell (HUVEC) populations is necessary to mimic bone physiological microenvironment.

The results demonstrated that hydroxyapatite functionalized with different amounts of quercetin displays both the good bioactivity of the inorganic phase and the therapeutic properties of the flavonoid. In fact, in vitro data show the quercetin functionalized samples stimulated osteoblast proliferation and activity, down-regulated osteoclastogenesis, and supported microangiogenetic processes necessary for new bone formation, allowing to state that the new materials exert a beneficial action onto bone repair microenvironment.

5.2 Calcium Phosphates functionalized with Quercetin.

5.2.1 Hydroxyapatite modified with alendronate

Hydroxyapatite was synthesized in the presence of alendronate, as previously reported [206]. The XRD diffraction pattern of HAAL sample (Figure 31) shows a slight increase of the peaks broadening when compared to HA pattern, suggesting that the presence of alendronate provokes just a modest increase of disorder.

The amount of alendronate incorporated into HA crystals was found to be 7 wt%. Despite the relatively high content of alendronate, the values of the lattice constants of the apatitic phase (a = 9.424(1) Å, c = 6.880(1) Å), as well as the Ca/P molar ratio (Ca/P = 1.67), are not significantly affected by alendronate incorporation [206].

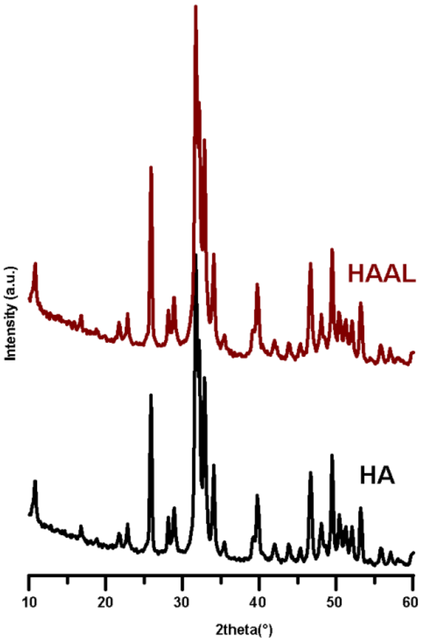

Figure 31 XRD patterns of HA and HAAL

5.2.2 HA and HAAL functionalized with Quercetin.

The powder XRD patterns reported in Figure 32 show that all the products obtained after quercetin adsorption are constituted of crystalline hydroxyapatite, independently from the time length of the adsorption process. However a peak, of low relative intensity (about 3%), is observable at 27.4 2θ°: it can be assigned to quercetin dihydrate phase. The amount of quercetin associated to HAAL samples does not vary as a function of time: the maximum amount of adsorbed quercetin (about 5.4 wt%) is reached already at 24h (Table 6).

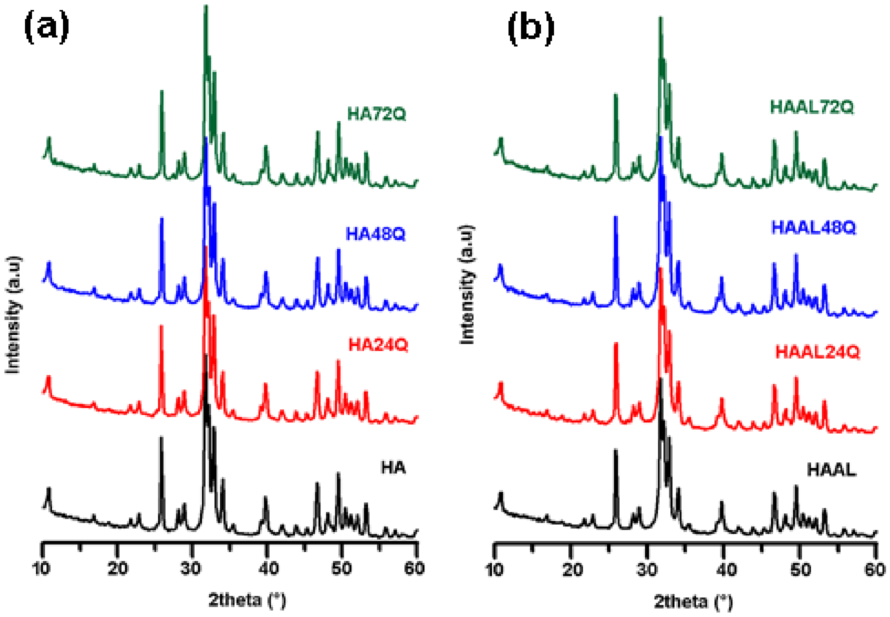

Figure 32 XRD patterns of (a) HA and (b) HAAL maintained in quercetin solution for different times.

Table 6 Quercetin content in the samples obtained with different adsorption times.

	Que 24h (wt%)	**Que 48h (wt%)**	**Que 72h (wt%)**
HA	4	5	6
HAAL	5.4	5.4	5.3

At variance, a modest increase of the amount of adsorbed quercetin as a function of time has been observed onto HA samples (Table 6)

Figure 33 reports the FTIR spectrum of pure quercetin, whereas Table 7 reports the FTIR bands assignment.

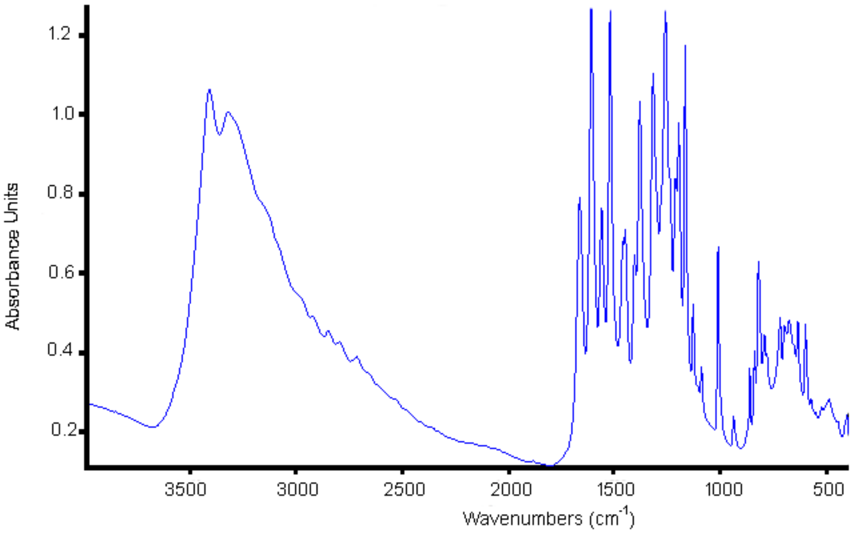

Figure 33 FTIR spectra of quercetin dihydrate.

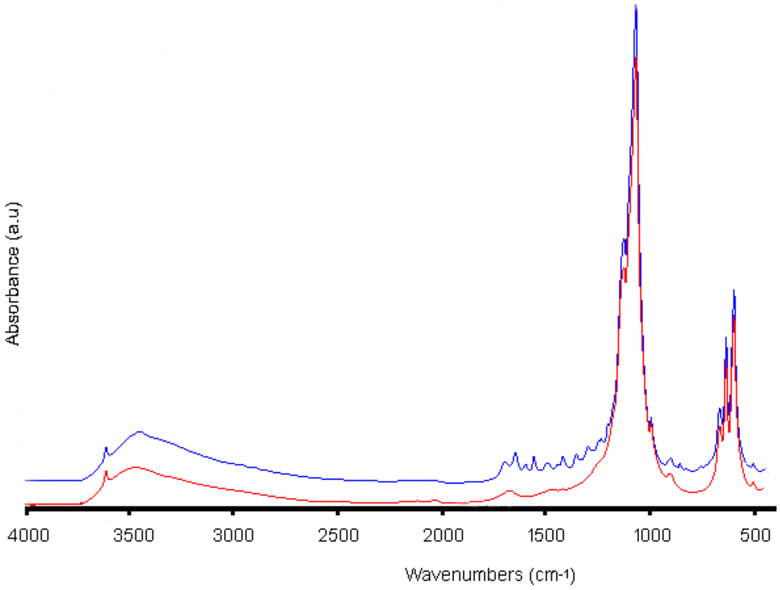

Figure 34 FTIR spectra of HA72Q

The most intense bands (1700- 800 cm^{-1}) of the flavonoid are present also in the spectra of HA and HAAL with adsorbed quercetin. The bands display a lower intensity, but fall in the same positions as in the reference spectrum (Figure 34). This result confirms the presence of quercetin on the apatitic crystals and the conservation of the flavonoid structure.

Table 7 FTIR band assignment of quercetin dihydrate [207, 208]

Attribution	Wavenumber (cm^{-1})
CCO bending (C)	601
CCO bending (C)	637
CCO bending (B)	678
CCO bending (A,B)	724
CCC bending (b) (C3-C4-C5)	760
CCC bending (B)	797
CCO bending (C)/ COC bending (C)	823
CCO bending (C)/ COC bending (C)	844
HCC bending (A,B)	941
HCC bending (A,B)	1013
COH bending (C)	1090
COH bending (B) (C2-OH)	1130
CCO bending (C)	1168
CC stretching (C,B)/ COH bending (A,C)/ HCC bending (A)	1196
OC stretching (B) (C2-O)	1216
CC stretching (C,B) / COH bending (C) (C3-OH)	1262
OC stretching (B/) COH bending (B) (C2-OH,C4-OH)	1313
CC stretching (A) /COH bending (B) (C4-OH)	1383
CC stretching (A) / CCO bending (A,C)	1410
CC stretching (A) / CCO bending (A,C)	1446
C=O stretching / CCC bending (B) (C2-C3-C4)	1523
C=O stretching / COH bending B (C5-OH)	1562
CC stretching (B)	1616
CC stretching (C) (C2-C3) / OC stretching (A,C)	1664
CH stretching (B)	2850
CH stretching (B)	2961
OH stretching C2-OH	3101
OH stretching	3244
OH stretching C,B	3313
OH stretching C,B	3384
OH stretching (A) C4-OH	3580

The antioxidant activity of these composite materials was evaluated through analysis of the radical scavenging activity, expressed as % RSA, which was performed on all the HA and HAAL samples modified with quercetin (Figure 35, 36). The test was performed on solutions at different concentrations, in order to analyze the effect of increasing amounts of quercetin. The solutions exhibited slightly different values of pH as a function of concentrations (Table 8); the pH of the solutions of pure quercetin was adjusted accordingly, in order to examine comparable data.

Table 8 pH of the solutions used to perform RSA analysis.

	10μM	**30μM**	**50μM**	**100μM**
HAQ	2.32	2.46	2.70	3.15

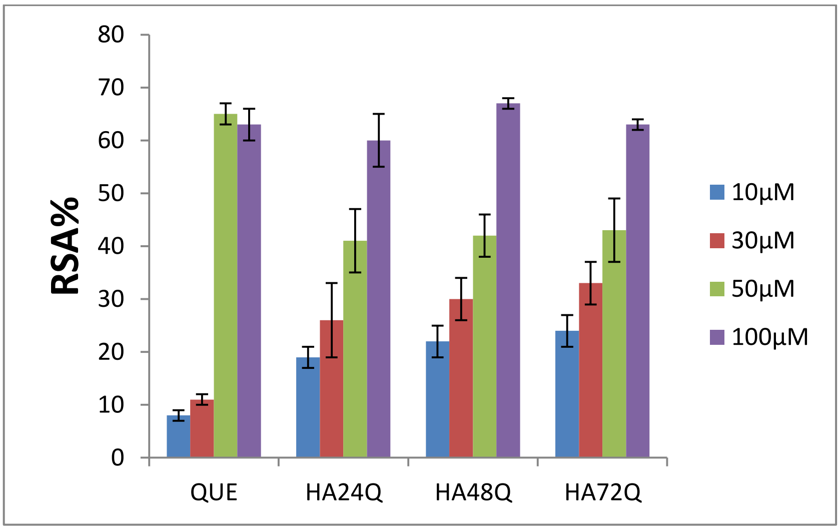

Figure 35 Comparison between the antiradical activity, expressed as% RSA, of the different products and that of pure quercetin. Each bar represents the mean standard deviation of three independent measurements.

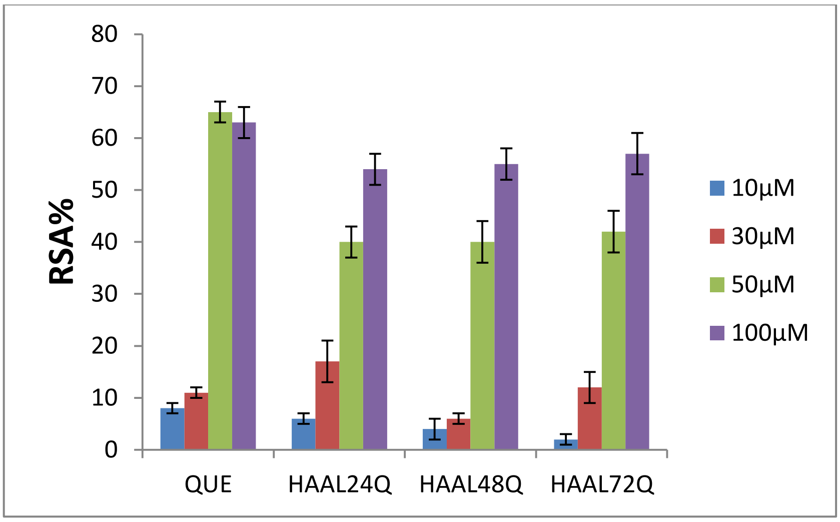

Figure 36 Comparison between the antiradical activity, expressed as% RSA, of the different products and that of pure quercetin. Each bar represents the mean standard deviation of three independent measurements.

Pure quercetin exhibits RSA values varying from 10% to 60% as a function of concentration. RSA values of the HAQ and HAALQ samples are generally similar to those of pure quercetin, with the exception of the data relative to 50 μM concentration. These data confirm that the antioxidant activity of quercetin is maintained in both HAQ and HAALQ samples.

5.2.3 DCPA and SrDCPA functionalized with Quercetin.

The powder XRD patterns reported in Figure 37 show that the products maintained in quercetin solutions for different times are constituted of crystalline monetite. Also in this case, the presence of a low intensity peak, at 27.4 2θ°, indicates the presence of quercetin dihydrate. The amount of quercetin associated at each samples increases slightly as a function of adsorption time (Table 9).

Performing this adsorption on DCPA, the crystallinity of the product was influenced by the presence of the ethanol and by the time of contact. To evaluate this influence, DCPA powder was put in contact with ethanol solution in the absence of quercetin for 24 and 72 hours. The XRD patterns show that the sharpness of the calcium phosphate peaks increases as function of exposure time (Figure 38) and so presumably does crystallinity.

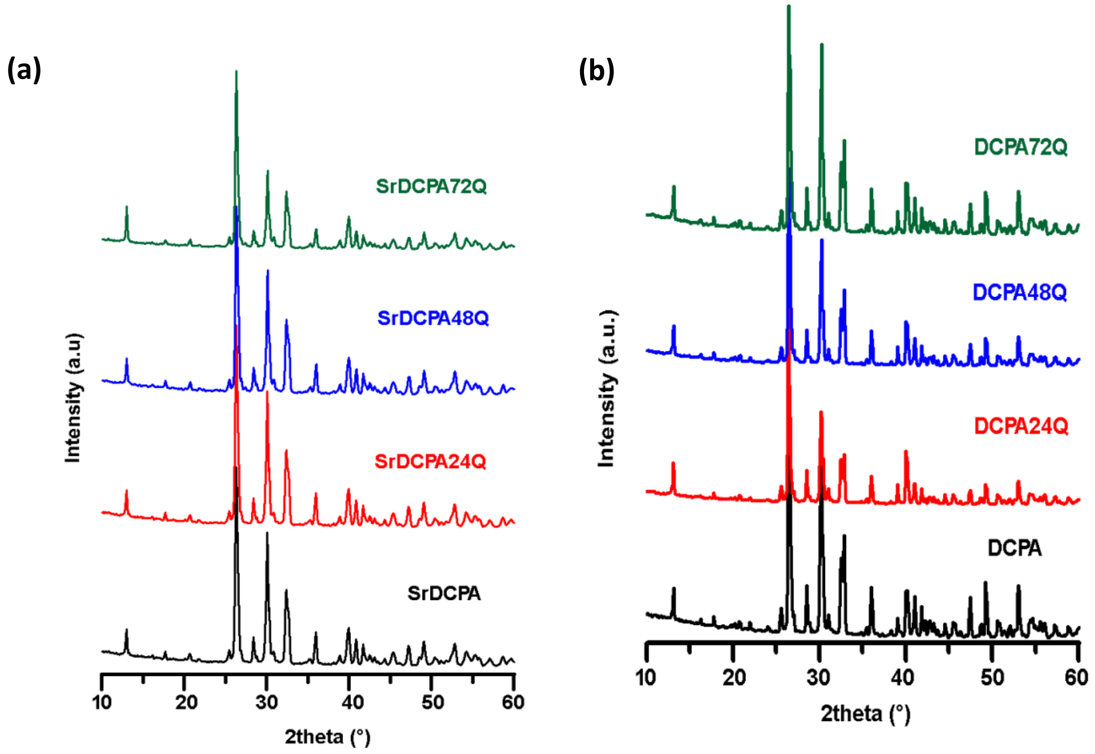

Figure 37 XRD patterns of (a) SrDCPA and (b) DCPA maintained in quercetin solution for different times.

Table 9 Quercetin content of DCPA and SrDCPA samples at different adsorption times

	Que 24h (wt%)	**Que 48h (wt%)**	**Que 72h (wt%)**
DCPA	3	3.7	4.4
SrDCPA	4	4	5.2

The FTIR spectra of DCPA and SrDCPA with quercetin, show the most intense bands (1700- 800 cm-1) of the flavonoid, which display a lower intensity and no appreciable shift with respect to those of the reference spectra (Figure 34). Figure 39 reports the FTIR spectra of the sample DCPA72Q. This result confirms the presence of quercetin on the apatitic crystals and the conservation of the flavonoid structure.

The FTIR bands attributions of monetite are reported in Table 10

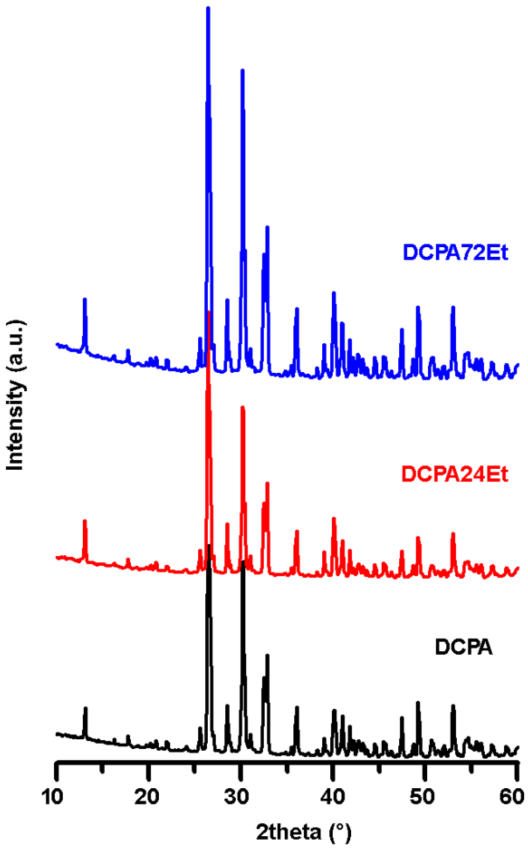

Figure 38 XRD patterns of DCPA after incubation in ethanol solution.

Table 10 FTIR bands of monetite [209].

Wavenumbers (cm^{-1})	Attribution
893	P-O(H) stretching
996	P-O stretching
1070	P-O stretching
1132	P-O stretching
1353	O-H in plane bending
1652	O-H in plane bending
2369	P-O-H stretching
3216	O-H stretching
3415	O-H stretching

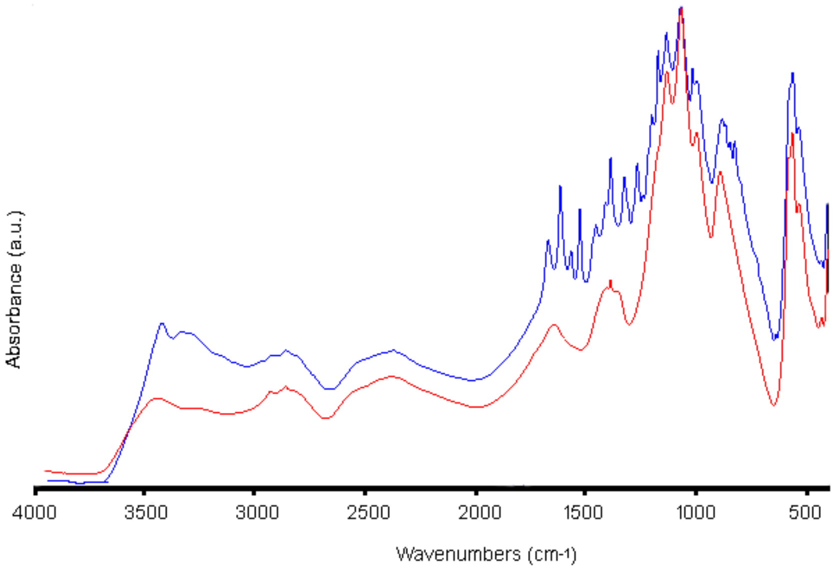

Figure 39 FTIR spectra of DCPA72Q

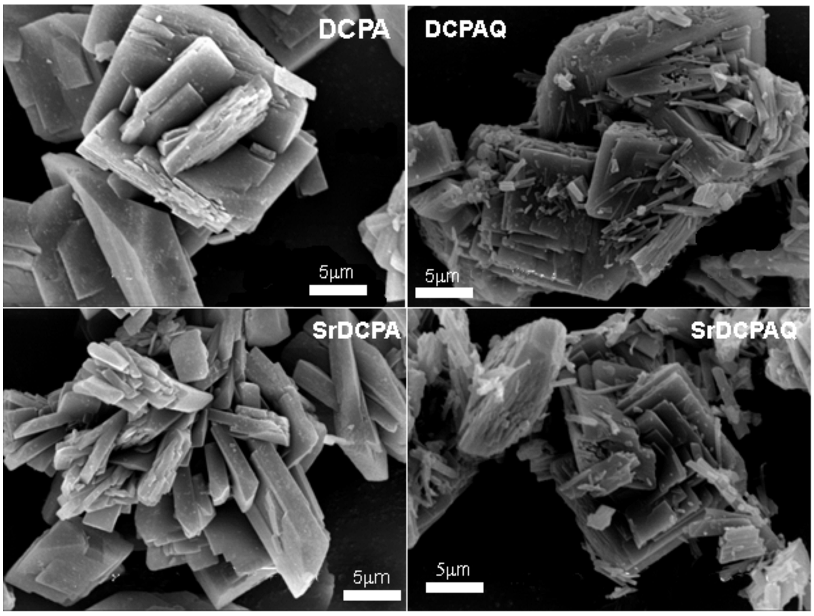

Figure 40 SEM images of DCPA and SrDCPA before and after quercetin adsorption.

SEM analysis shows that DCPA and SrDCPA crystals exhibit well defined edges and twinning.. After flavonoid adsorption, the crystals appear splitted in smaller ones with ill-defined edges, most likely affected by the stirring used for the adsorption experiments Figure 40).

The values of RSA of the different samples are compared with that of pure quercetin, determined at different values of pH (Table 11), in Figures 41 and 42.

Table 11 pH of the solutions used to perform RSA analysis

sample	10μM	30μM	50μM	100μM
DCPAQ	2.23	2.33	2.48	3.03

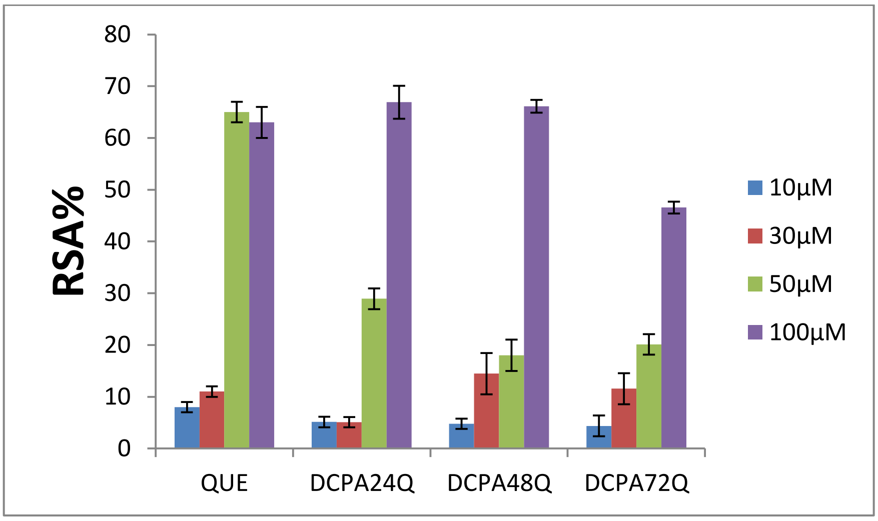

Figure 41 Comparison between the antiradical activity, expressed as% RSA, of the different products and that of pure quercetin. Each bar represents the mean standard deviation of three independent measurements.

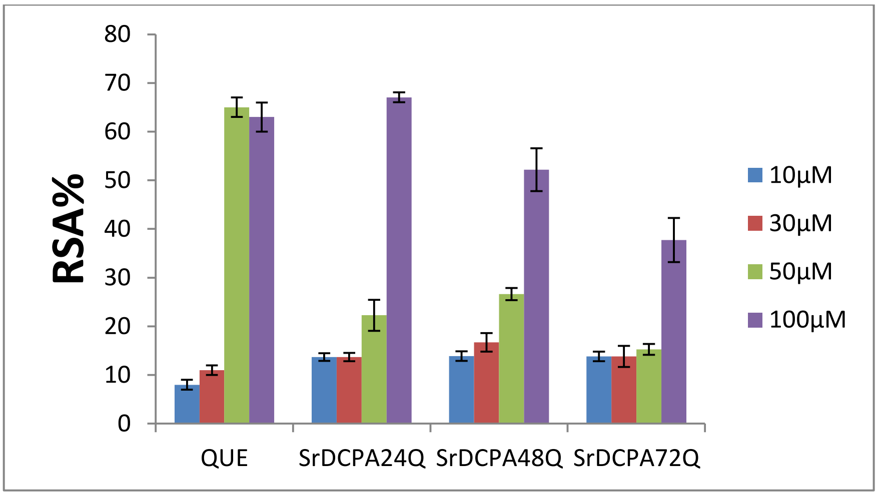

Figura 42 Comparison between the antiradical activity, expressed as% RSA, of the different products and that of pure quercetin. Each bar represents the mean standard deviation of three independent measurements.

The trend is similar to that previously observed for the apatitic samples (Figures 35 and 36) and confirms that the antioxidant activity of quercetin is maintained also in these samples.

5.3 *Octacalcium phosphate functionalized with alendronate and zoledronate*

The aim of this study is the functionalization of octacalcium phosphate with alendronate and zoledronate, in order to obtain new biomaterials for the local treatment of diseases characterized by abnormal bone loss. In fact, the possibility to functionalize OCP with BPs through co-precipitation in order to couple the good biological performance of OCP with the therapeutic properties of bisphosphonates has not been explored up to now.

The results of XRD analysis show that functionalization of OCP with alendronate can be obtained up to a bisphosphonate concentration in solution of 1.2 mM. In fact the XRD patterns of the products exhibit the presence of octacalcium phosphate, as unique crystalline phase, up to sample OAL1.2. At variance, the XRD pattern of the sample OAL1.5 shows also the presence of a little amount of crystalline calcium alendronate [210], as evidenced by the presence of two additional peaks at about 9.1° and 12.8° of 2θ (indicated by symbols in Figure 43).

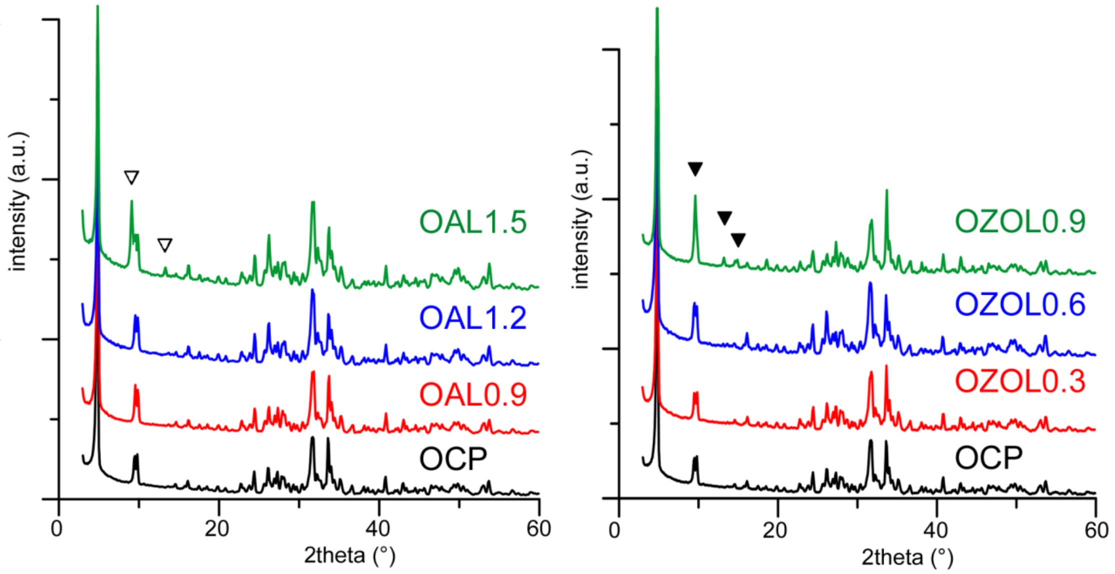

Figure 43 X-ray diffraction patterns of the products synthesized in the presence of increasing concentrations of alendronate and zoledronate, compared with that of pure OCP. The symbols indicate the presence of crystalline calcium alendronate (▽) and calcium zoledronate(▼) [189].

The structure of OCP is not significantly affected by the presence of AL, in agreement with the absence of significant variations in the values of the lattice parameters, which are close to those calculated for pure OCP

(Table 12). At variance, the broadening of the diffraction reflections displays a modest increase with the increasing of alendronate content, suggesting a reduction of the crystallinity degree.

Table 12 Cell parameters (e.s.d. in parentheses) of OALXX samples which showed octacalcium phosphate as unique crystalline phase [189].

	a (Å)	*b* (Å)	*c* (Å)	α (°)	β (°)	γ (°)
OCP	19.722(3)	9.552(2)	6.847(1)	90.13(1)	92.56(2)	108.28(1)
OAL0.1	19.733(8)	9.564(4)	6.855(2)	90.16(4)	92.58(5)	108.24(4)
OAL0.3	19.706(3)	9.542(1)	6.841(1)	90.13(1)	92.55(1)	108.25(1)
OAL0.6	19.709(3)	9.547(2)	6.842(1)	90.15(1)	92.55(2)	108.26(1)
OAL0.9	19.720(3)	9.553(1)	6.847(1)	90.15(1)	92.54(2)	108.26(1)
OAL1.2	19.722(3)	9.552(1)	6.845(1)	90.15(1)	92.54(1)	108.26(1)

A qualitative estimation of the size of the coherently scattering domains (i.e. the crystallite size) was performed from the line broadening of the 100, 002 and 010 reflections. The lengths of the coherent domains (τ_{hkl}), calculated using the Scherrer equation, are showed in table 13.

Table 13 Coherent lengths (τhkl) of the perfect crystalline domains in the direction normal to (100), (002) and to (010) planes calculated using the Scherrer method; zeta potential (ξ); and bisphosphonate content [189].

	τ_{100} (Å)	**τ_{002} (Å)**	**τ_{010} (Å)**	**ξ(mV)**	**BP content (wt%)**
OCP	545(21)	816(48)	604(21)	-7.8	--
OAL0.1	530(49)	796(41)	617(10)	-3.0	3.0
OAL0.3	515(40)	759(62)	606(18)	-2.0	3.2
OAL0.6	508(26)	777(83)	667(22)	-3.1	3.6
OAL0.9	487(42)	727(70)	586(17)	-3.9	4.3
OAL1.2	468(33)	742(61)	557(15)	-3.6	5.2

The data reported in Table 13 show that on increasing alendronate concentration, τ_{hkl} values display a general trend to decrease. The amount of alendronate contained in the solid products increases from a minimum value of 3.0 wt% up to a maximum value of about 5.2 wt%. .

SEM images show plate like crystals, which exhibit a morphology typical of OCP. Moreover, it is evident the reduction of the mean dimensions of the crystals with the increase of alendronate content. The relative size histograms, reported in Figure 44, show that the decrease of the mean size is greater along the width of the crystals than along their length. Accordingly, the length/width ratio passes from about 10 to about 15 on going from pure OCP to OAL1.2, suggesting a preferential interaction of alendronate with the (0k0) faces of OCP structure.

Table14. Mean length and width values of OCP and OALXX crystals as measured from SEM observations. T Student test was employed to assess statistical significant differences vs. OCP (* $p<0.05$; ** $p<0.001$) [189].

	Mean Length (µm)	Mean Width (µm)	Length/Width
OCP	71.95 ± 26	6.75 ± 2	10.66
OAL0.6	40.55 ± 21	3.99 ± 2	10.16
OAL0.9	42 ± 18	3.29 ± 1	12.76
OAL1.2	32.69 ± 12	2.16 ± 1	15.13

The zeta potential of OCP was found to be -7.78 mV, in agreement with the basic pH of the solution (about 8.5) [211]. The zeta potential values of the samples containing alendronate are slightly higher than that of pure OCP, without showing any significant variation as a function of alendronate content, as shown in Table 13.

These results could be related to the data on alendronate release. Figure 45 shows that, in the first 10 hours, all OALXX samples display a fast release, after which they reach constant alendronate content. On this basis, it can be suggested that a great part of alendronate is weakly bound to OCP crystals and easily lost in solution, whereas the part retained in the solid products involves a stronger interaction with the calcium phosphate. After release, the different samples exhibit similar values of alendronate content (about 1.5 wt %), which could justify the similar values of zeta potential.

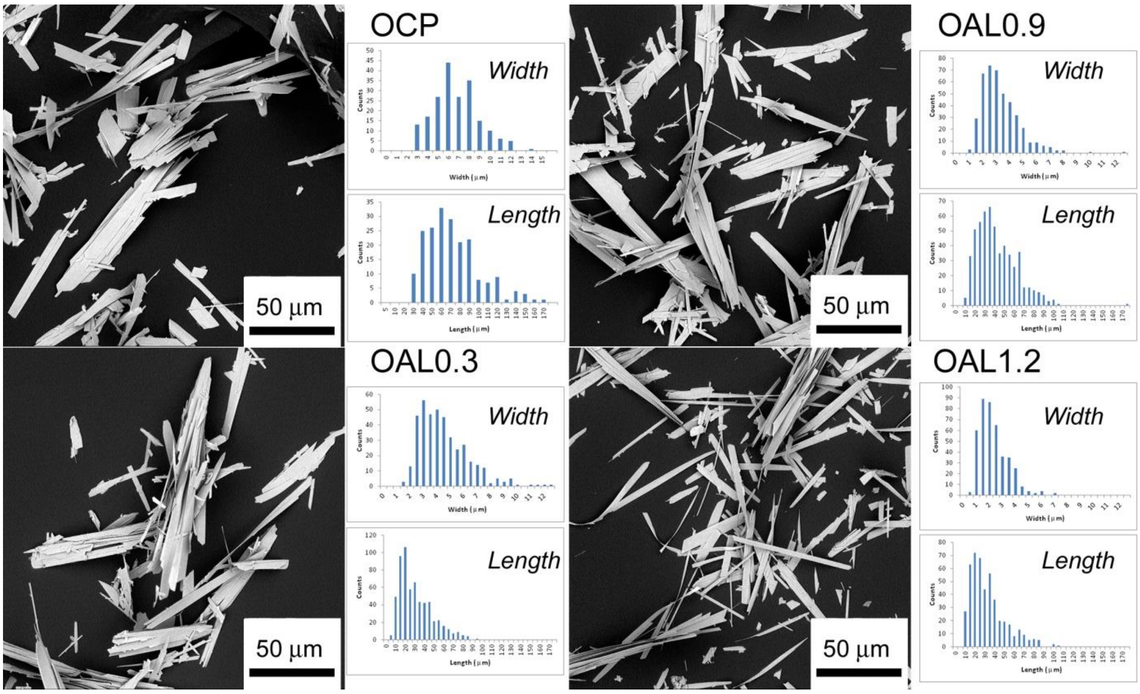

Figure 44 SEM images of the products synthesized in the presence of increasing concentrations of alendronate compared with that of pure OCP. The histograms show the size distribution along the length and the width of the crystals [189].

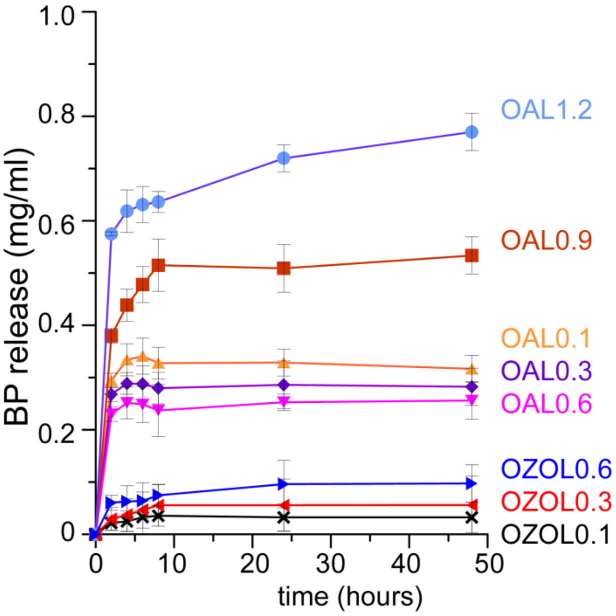

Figure 45 Alendronate and zoledronate release from the different samples as a function of time [189].

The range of zoledronate concentration which allowed to obtain OCP as a single crystalline phase is lower than that verified for alendronate. In fact, the XRD patterns (Figure 46) show that OZOL0.9 contains also a second phase, as supported by the presence of three additional peaks at 9.6, 13.2 and 18.6 ° of 2θ, which correspond to the most intense peaks of crystalline calcium zoledronate [120].

SEM images of the sample OZOL0.9 show big plate-like crystals characteristic of OCP mixed with very small thin elongated crystals, supporting the information obtained by XRD analysis about the presence of a second crystalline phase (Figure 46). OCP crystals synthesized in the presence of zoledronate tend to aggregate: SEM images of all ZOLXX samples show the presence of both separate crystals and spherulites, with the relative amount of aggregates increasing with increasing ZOL content (Figure 4). Moreover, histograms in Figure 46 show an increase of the length/width ratio with respect to that of OCP, similar to what observed for OALXX samples, caused by the variation of crystal dimensions on increasing ZOL content in solution.

Table 15 Mean length and width values of OCP and OZOLXX crystals as measured from SEM observations. T student test was employed to assess statistical significant differences vs. OCP (* $p<0.05$; ** $p<0.001$) [189].

	Mean Length (µm)	Mean Width (µm)	Length/Width
OCP	71.95 ± 26	6.75 ± 2	10.66
OZOL0.1	76.65 ± 28	5.28 ± 2	14.52
OZOL0.3	55.46 ± 23	4.30 ± 1	12.90
OZOL0.6	26.98 ± 11	2.005 ± 1	13.46

Zoledronate content in the solid products increases with its concentration in solution, up to about 3.5 wt% (Table 16). As observed for alendronate, the lattice parameters are not influenced by the incorporation of zoledronate, whereas the mean lengths of the coherently scattering domains along the crystallographic direction 100, 002 and 010 significantly reduce.

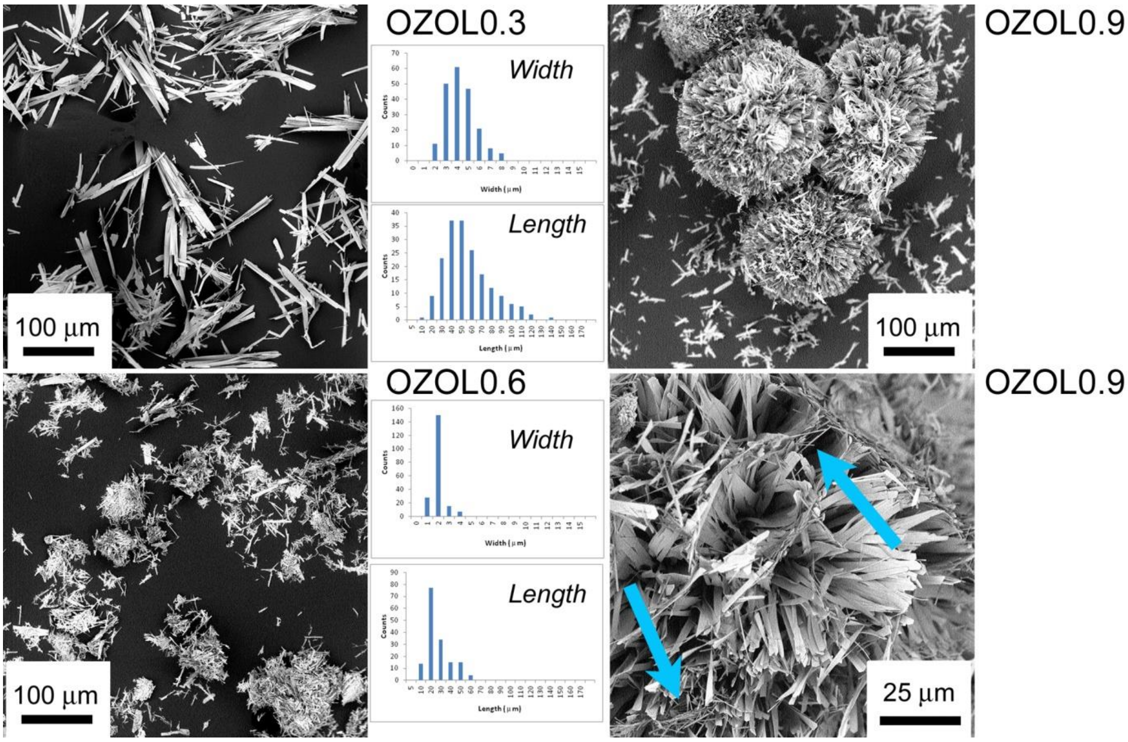

Figure 46 SEM images of the products synthesized in the presence of increasing concentrations of zoledronate. The histograms show the size distribution along the length and the width of the crystals [189].

Table 16 Coherent lengths (τhkl) of the perfect crystalline domains in the direction normal to (100), (002) and to (010) planes calculated using the Scherrer method; zeta potential (ξ); and bisphosphonate content [189].

Sample	τ_{100} [Å]	τ_{002} [Å]	τ_{010} [Å]	ξ[mV]	BP content [wt%]
OCP	545(21)	816(48)	604(21)	-7.8	--
OZOL0.1	547(29)	726(65)	581(15)	-16.0	1.3
OZOL0.3	500(33)	595(32)	538(19)	-17.3	2.4
OZOL0.6	487(32)	573(40)	518(15)	-20.0	3.5

Table 17 Cell parameters (e.s.d. in parentheses) of OZOLXX samples which showed octacalcium phosphate as unique crystalline phase [189].

	a (Å)	*b* (Å)	*c* (Å)	α (°)	β (°)	γ (°)
OCP	19.722(3)	9.552(2)	6.847(1)	90.13(1)	92.56(2)	108.28(1)
OZOL0.1	19.734(4)	9.557(2)	6.848(1)	90.14(2)	92.57(2)	108.29(2)
OZOL0.3	19.718(6)	9.547(2)	6.845(1)	90.14(2)	92.55(3)	108.22(2)
OZOL0.6	19.737(3)	9.560(2)	6.849(1)	90.15(1)	92.54(1)	108.27(1)

The graph in Figure 45 show that OZOLXX composite samples do not show appreciable BP release in solution, at variance with the results obtained for OALXX samples. This result can be explained with the stronger interaction that zoledronate has with OCP structure. The stronger binding affinity of the two bisphosphonates towards hydroxyapatite was previously justified by the possibility of ZOL to form two H bonds with HA structure and by the availability of a favorable Ca ions coordination geometry [212, 213].

In particular, these N-H-O hydrogen bonds can be formed at two different sites on HA and, for optimal binding, an N-H-O angle ≥125° and an N-O distance of about 3 Å is required. One H binding site can occur at a hydroxyl coordinated to the second type of calcium (CaII) in HA.

The $-NH_2$ group of alendronate is able to form this N-H-O bond because of its structure (132°, 2.7 Å N-O distance).

A second H bonding interaction can occur at a neighboring calcium (CaI), which can optimally allow a bifurcated dual bonding arrangement, as predicted by the zoledronate N-H-O bonding angles and distances with its distal heteroaromatic nitrogen [212].

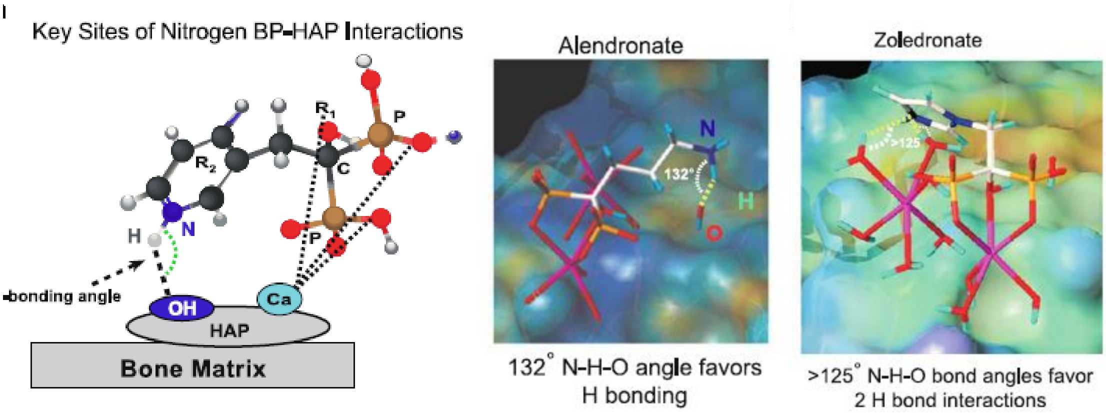

Figure 47 Molecular modeling: bisphosphonates binding to hydroxyapatite. An electrostatic surface representation of HAP with the key binding residues of Zoledronate and Alendronate [212].

Considering that OCP and hydroxyapatite are structurally similar, the same argument can be extended to discuss the different interaction of ZOL and AL with OCP. A sketch of possible interactions between OCP structure and BPs is reported in Figure 48.

The values of zeta potential of ZOLXX samples reduce significantly on increasing BP content, down to -20 mV (Table 16). A similar effect of zoledronate on zeta potential was previously reported for hydroxyapatite crystals at different ZOL content; the shift of the zeta potential towards negative values was interpreted as due to the binding of negatively charged phosphonate groups to Ca^{2+} sites on the surface of hydroxyapatite, which becomes more negative [214]. Previous results on the different influence of zoledronate and alendronate on the zeta potential of hydroxyapatite as a function of BPs concentration in solutions [121] were justified on the basis of the different pKa of AL and ZOL functional groups.

Hydrolysis test was carried out on pure OCP and the obtained powders were controlled using X-ray diffraction analysis. The results show that, after three days storage in solution at pH 7.4 at 60°C, octacalcium phosphate is completely converted into HA (Figure 49). On the contrary, the composite OALXX and OZOLXX crystals do not exhibit any conversion into HA even after 30 days (Figure 50), indicating that the presence of BPs prevents the hydrolysis reaction.

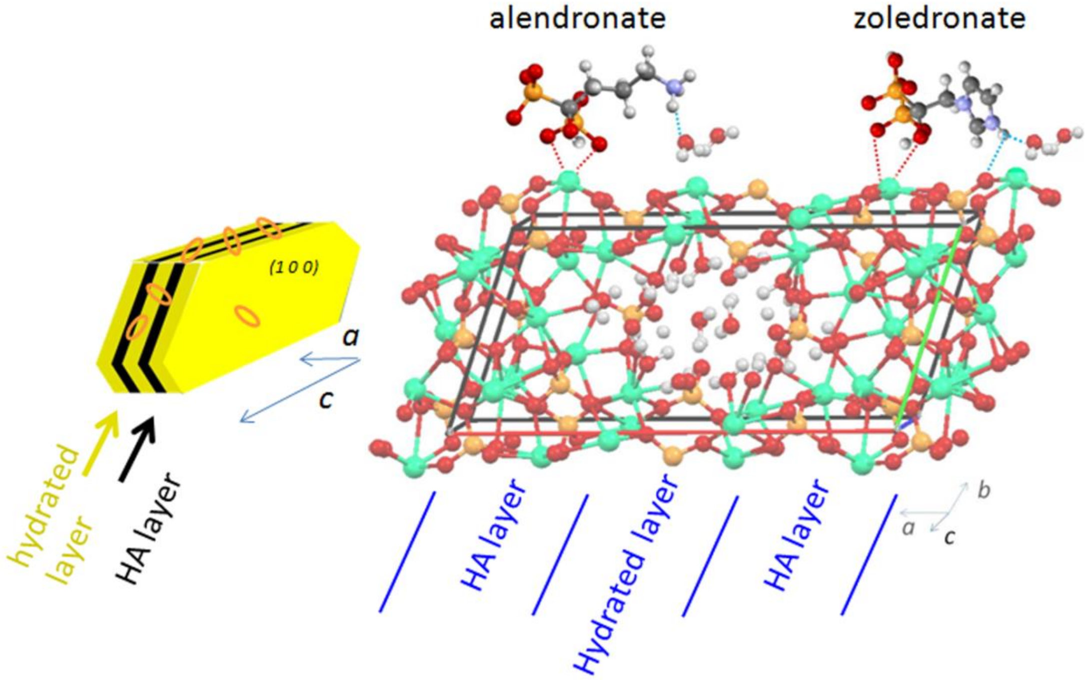

Figure 48 Scheme of possible structural interaction between alendronate or zoledronate molecules and the crystalline structure of OCP [189].

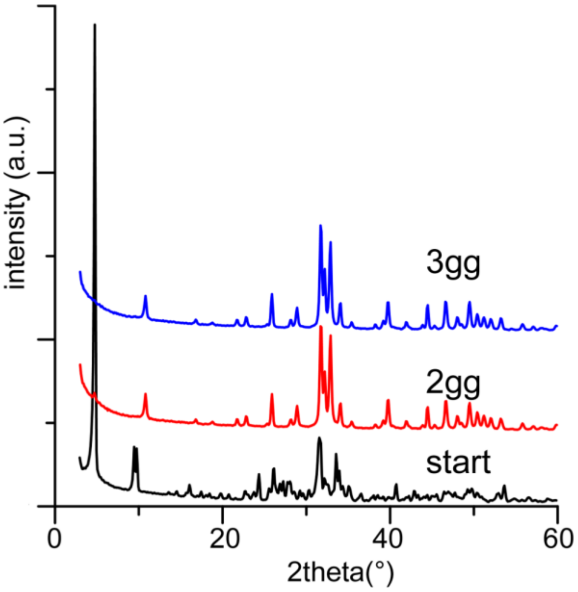

Figure 49 Powder X-ray diffraction patterns of the solid products obtained after OCP storage in aqueous solution at pH 7.4 and 60°C, plotted as a function of storage time [189].

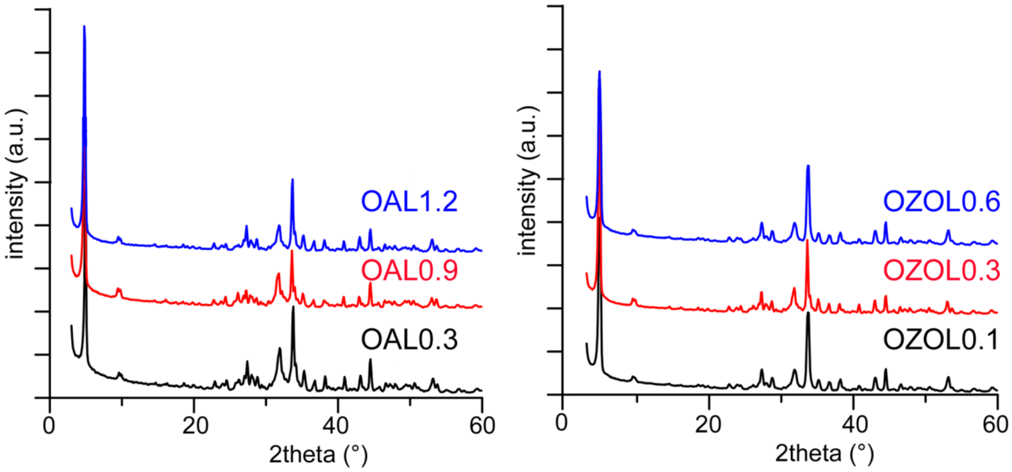

Figure 50 Powder X-ray diffraction patterns of the solid products obtained after OALXX and OZOLXX storage in aqueous solution at pH 7.4 and 60°C, after 30 days of storage time [189].

These results can be explained looking the two limiting equations for the hydrolysis reaction depending on the availability of calcium ions in the solution, proposed by Brown et al [215]

$$\frac{10}{8}\ Ca_8H_2(P0_4)_6 * 5\ H_20\ (xtal) \rightarrow 2\ Ca_5(PO_4)_3OH\ (xtal) + \frac{3}{2}\ H_3PO_4(soln) + \frac{17}{4}\ H_20\ (soln) \qquad (1)$$

$$Ca_8H_2(PO_4)_6 * 5\ H_20\ (xtal) + 2\ Ca^{2+}(soln) \rightarrow 2\ Ca_5(PO_4)_30H\ (xtal) + 4\ H^+(soln) + 3H_20\ (soln)\ (2)$$

It can be seen from equation (1) that 20% of the phosphate is lost to the solution in the absence of calcium ions in the solution and this loss probably affects the kinetics of the reaction.

If the calcium ions are not easily available, the reaction is likely to fall somewhere between equations (1) and (2). At the same time, the apatitic product may be calcium deficient. It has been observed that the hydrolysis process does not go to completion. This indicates that the mechanisms for diffusion of calcium ions into the hydrolyzing crystal and those for removing water molecules and hydrogen ions are inadequate and lead to the retention of OCP in the crystals.

In the case of OALXX and OZOLXX samples, calcium ions might be sequestered by BPs because of their high affinity with it, blocking the hydrolysis reaction.

On the other hand, BPs do not influence the thermal stability of OCP. The XRD patterns recorded from pure OCP at increasing temperatures show the onset of a shoulder next to the (100) small angle reflection at 4.7° 2θ, together with a variation towards an apatitic pattern in the higher angles region. Above 200°C, the split of the low angle reflection in two peaks and the onset of a new peak at 5.2 ° 2θ suggest the presence of a further phase, previously identified as “collapsed OCP” [216], whereas above 250°C the pattern displays the characteristics of a poor crystalline apatitic phase. The same trend is observable for OALXX and OZOLXX samples, as shown in Figure 51 for the sample OZOL0.6.

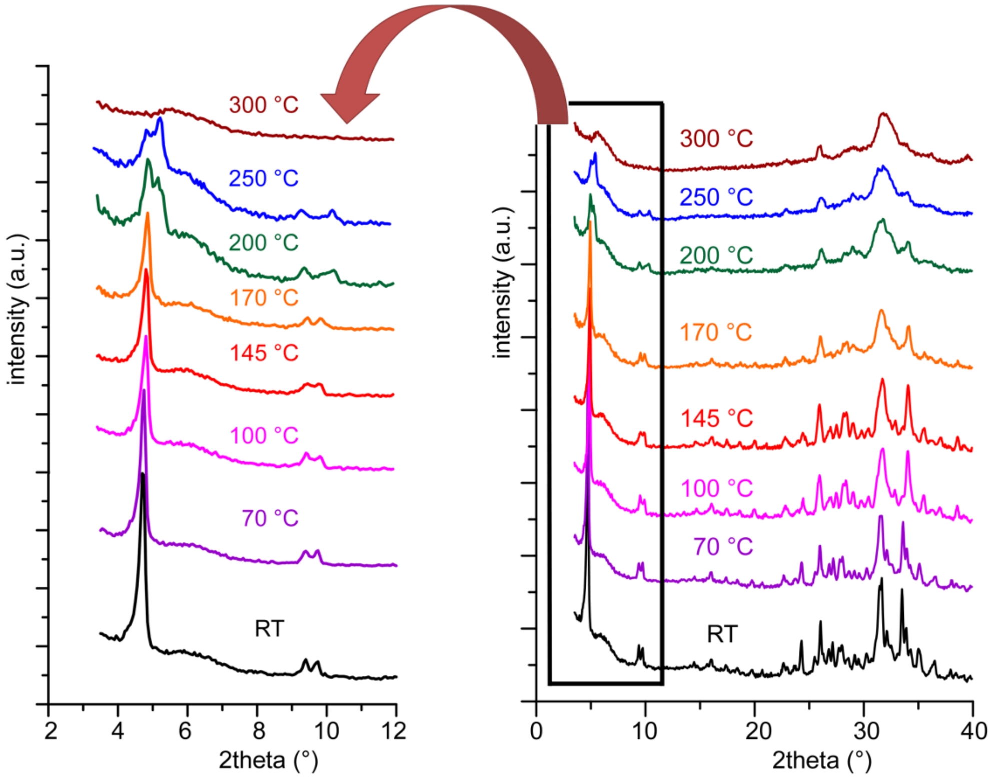

Figura 51 Powder X-ray diffraction patterns of OZOL0.6 recorded in situ at increasing temperature up to 300 °C (right) and high magnification of the small angle region (left) [189].

Bone cells response of the synthesized materials was tested *in vitro* using a triculture model involving osteoblasts (OB), osteoclast (OC) and endothelial cells (HUVEC) in order to mimic bone microenvironment. In order to avoid morphology influence on cell response, the tests were performed on disk-shaped which do not present significant surface difference as a function of composition and similar roughness parameters, Ra=0.178±0.014 μm, Rq= 0.220±0.022 μm, Rt=1.681±0.065 μm.

The results of the triculture tests indicate that BP functionalized samples downregulate the viability of the cells, sustain osteoblast differentiation and accelerate the production of collagen type I and osteocalcin. At variance, they inhibit monocyte differentiation into osteoclast and provoke a dose dependent reduction of VEGF production, exhibiting antiresorptive and anti-angiogenetic properties that can be usefully exploited for the local treatment of abnormal bone losses [189].

5.4 Hydroxyapatite functionalization as a tool to modulate adsorption and release of risedronate.

Calcium phosphates (CaPs) have been largely suggested as supports for the local administration of bisphosphonates (BPs), because of their biocompatibility and bioactivity and of the great affinity that BPs display for them [213, 217-223].

CaPs functionalized with BPs can be prepared through adsorption from solution, as reported in literature [220, 213, 223], but it has been demonstrated that the structure and the composition of the apatitic surface play a fundamental role on the mechanism of adsorption and desorption process, influencing adsorption parameters and the kinetic of release of bisphosphonate [223-225].

On this basis, in this study HA with a partial substitution of zinc to calcium (ZnHA), HA and ZnHA functionalized with polyethyleneimine (HAPEI, ZnHAPEI), as well as HA as control material, were utilized to investigate the role of composition and surface charge of hydroxyapatite on the adsorption and release mechanisms of risedronate.

The polycationic polymer PEI should enhance the positive charge the surface of the apatitic nanaocrystals, promoting the adsorption of negatively charged BP from solution and controlling its release. On the other hand, cationic substitution in HA can influence crystal growth and influence specific surface, modifying adsorption capability.

The adsorption of risedronate on these supports and the relative release mechanisms were investigated in order to understand the interaction of BP with the apatitic supports.

5.4.1 Characterization of HA, HAPEI, ZnHA and ZnHAPEI substrates

The amount of PEI associated to the apatitic phase was determined through thermogravimetric analysis (Figure 52): it increases as a function of concentration in solution up to about 2.5 wt%.

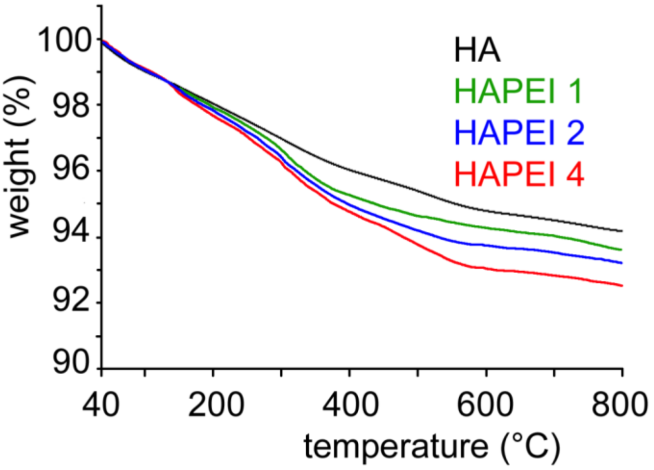

Figure 52 Thermogravimetric plots of the apatitic samples synthesized in the presence of increasing PEI concentration in solution (1 M, 2 M and 4 M of PEI) [186].

The powder XRD patterns reported in Figure 53 show that the products obtained through the synthesis of HA in the presence of different PEI concentrations in solution, namely 1, 2 and 4, are constituted of hydroxyapatite as unique crystalline phase. Observing the XRD patterns of the HAPEI samples, it's evident that the sharpness of the diffraction peaks increases on increasing PEI concentration, which suggests an increase of crystallinity of the apatites precipitated in the presence of the polymer.

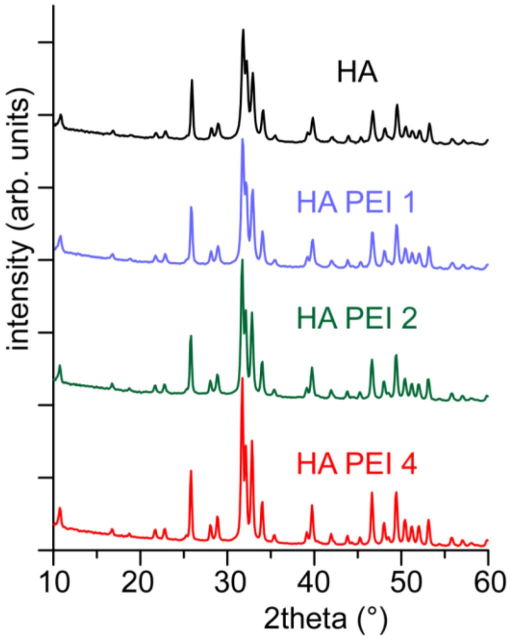

Figura 53 Powder X-ray diffraction patterns of the apatitic samples synthesized in the presence of increasing PEI concentration in solution (1 M, 2 M and 4 M of PEI) [186].

The increase of crystallinity, related to the PEI content in the different samples, is confirmed also by RAMAN analysis, as shown in Figure 54. The Raman spectra not only show the characteristic bands of apatite, reported in Table 18, but also the presence of the bands of the polymer, which display an increase of intensity with the increasing of PEI content in the samples. The PEI characteristic bands are between 2800 cm^{-1} and 3200 cm^{-1} and they can be attributed to the stretching vibration of the CH and CH_2 groups.

Table 18 Raman bands of apatite [226]

Attribution	**Raman (cm^{-1})**
ν_2 PO_4	432 452
ν_4 PO_4	584 590 611
P-OH, HPO_4	1004 873
ν_1 PO_4	961
ν_3 PO_4	1005 1032 1044 1071
ν_1 CO_3 Type A Type B	1071 1103

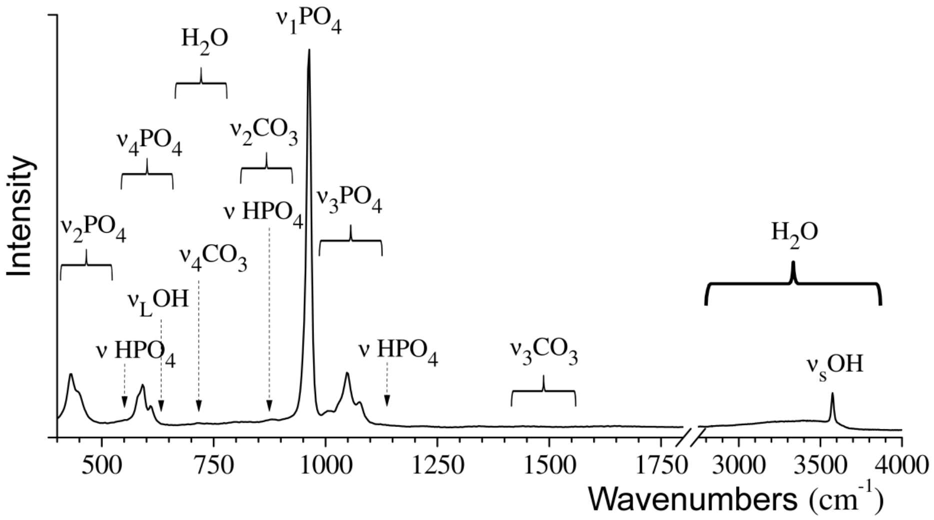

Figure 54 Raman assignments for apatite

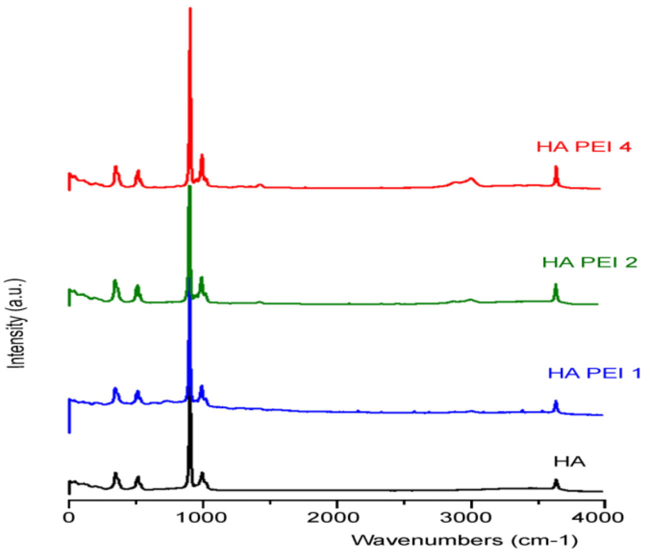

Figure 55 Raman spectra of the apatitic samples synthesized in the presence of increasing PEI concentration in solution (1 M, 2 M and 4 M of PEI) [186].

The FTIR spectra show no relevant differences among the samples at different amount of PEI, however the spectral decomposition in the 400-800 cm^{-1} vibration domain displays an enhancement of the relative intensity of the OH band, on passing from HA to HAPEI 4. This result, in agreement with Raman and XRD analysis, confirms the increase of crystallinity as function of PEI content. Ratios of bands integrated intensities were used to follow the evolution of spectral features, taking the sum of apatitic phosphate bands as a reference, as shown in the following formula.

$$Integrated\ intensity\ ratio\ of\ OH^{-}\ ions\ = \frac{OH^{-}\ apatitic}{OH^{-}\ apatitic + PO_4^{3-} apatitic + HPO_4^{2-}\ apatitic}$$

For these mathematical decompositions, based on Kauppinen’s methodology [227], the bands were considered as Lorentzian in shape. Ratios of bands integrated intensities were used to follow the evolution of spectral features, taking the sum of apatitic phosphate bands as a reference. The FTIR bands used for this analysis and the others characteristic of apatite are reported in Table 19.

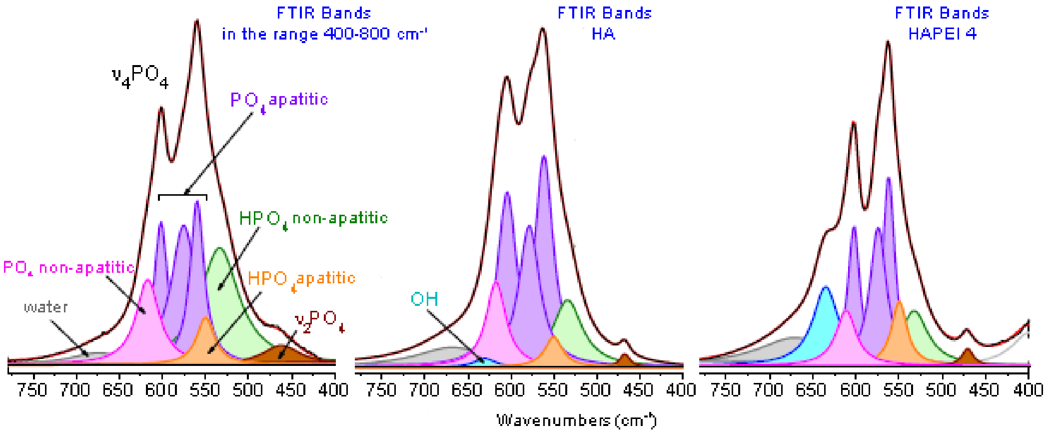

Figure 56 Mathematical decomposition of the FTIR bands in the range400-800 cm^{-1}

Table 19 Attribution of FTIR bands of apatite

Attribution	Wavenumbers (cm^{-1})
ν_2 PO_4	469
HPO_4 non apatitic	533
HPO_4 apatitic	551
ν_4 PO_4 antisymmetric bending PO43-	562, 575, 603
PO_4 non- apatitic	617
ν_L OH vibration of OH^-	633
HPO_4 stretching P-OH	873
ν_1 PO_4	962
ν_3 PO_4 symmetric stretching PO_4^{3-}	1006, 1020, 1031, 1044, 1059, 1072, 1091, 1104
HPO_4	1144

In particular, the principal FTIR bands are those of the apatitic phosphate groups: the multiple bands between 1006 cm^{-1} and 1104 cm^{-1} correspond to the antisymmetric stretching mode ν_3 and the band at 962 cm^{-1} corresponds to the symmetric stretching ν_1.

The bands of the bending mode of the PO_4^{3-} group are between 562 cm^{-1} and 617 cm^{-1} (ν_4) and at 469 cm^{-1} (ν_2).

When apatite is not stoichiometric the hydrogen phosphate groups are detected at 551 cm^{-1}, 870 cm^{-1} and 1144 cm^{-1} .

The lengths of the coherent domains (τ_{hkl}), in particular τ_{002}, which is related to the mean crystallite size along the *c*-axis, and τ_{310}, which it refers to the mean crystallite size along a direction perpendicular to *c*-axis, and the values of microstrain (ε) were calculated from the microstructure parameters of X-ray diffraction pattern refinement procedure. The results show that the coherent length of the perfect crystalline domains increases significantly both along the *c*-axis direction and, even more, along the orthogonal direction on increasing PEI content in the solids (Table 20). At variance, the values of microstrain are of the order of 10^{-4} and do not change appreciably as a function of composition. In agreement with the increase of crystallinity, the lattice parameters exhibit a slight but significant reduction of the *a*-axis on increasing PEI content.

Table 20 Lattice parameters, coherent lengths (Lhkl) of the perfect crystalline domains and microstrain (Ɛ hkl) in the direction normal to 002 and to 310 planes; PEI content, zeta potential and Ca/P molar ratio of the apatitic samples synthesized in the presence of PEI [186].

	HA	**HAPEI 1**	**HAPEI 2**	**HAPEI 4**
a (Å)	9.4318(3)	9.4358(2)	9.4299(2)	9.4298(2)
c (Å)	6.8862(2)	6.8903(3)	6.8855(2)	6.8872(2)
L_{002} (Å)	657(4)	667(5)	749(6)	929(7)
L_{310} (Å)	311(3)	358(3)	405(4)	543(5)
ε_{002} ($*10^{-4}$)	9.9(8.5)	6.9(5.1)	6.9(2.7)	5.9(7.0)
ε_{310} ($*10^{-4}$)	6.0(1.2)	4.6(1.2)	6.2(2.3)	6.8(4.8)
PEI content (wt%)	---	0.9(0.5)	1.7(0.5)	2.4(0.5)
zeta potential (mV)	- 15.6	+ 19.5	+ 24.2	+ 26.2
Ca/P	1.67	1.67	1.67	1.73

TEM images show that the morphology of the composite nanocrystals is influenced by PEI. In fact, the HAPEI nanocrystals display a shorter mean length and a greater thickness when compared with HA ones (Figure 57). On the basis of their increased thickness and coherent length of perfect crystalline domains, HAPEI nanocrystals could be suggested to be indeed mesocrystals [228] made up of nanoparticles of HA aligned by PEI. In fact, PEI interacts preferentially with the hydroxyapatite crystal faces parallel to the c-axis and promotes the oriented attachment of nanoparticles, which leads to the observed increased thickness.

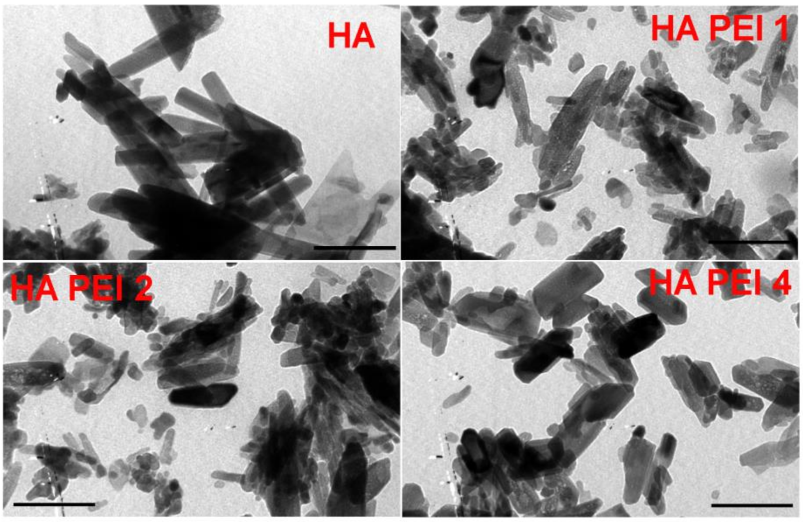

Figure 97 TEM images of the samples obtained by synthesis with PEI, at different concentration.

In general, when an organic matrix is present, there are two ways for the formation of nanocrystals as the building blocks of mesocrystals. In one case, the nanocrystals are generated first. They then attach to the organic matrix and get oriented. In another case, the organic matrix provides a heterogeneous nucleation site for the nanocrystals. A sketch that explains the nanocrystal alignment by an oriented organic matrix [229] is reported In Figure 58.

However, in the case of HAPEI the morphological variation does not provoke significant modification of the superficial area, which is similar to that of pure HA (Table 21).

The zeta potential of HA is -15.6 mV but the presence of PEI confers positive charge to the samples, which increases as a function of the content of the polycationic polymer (Table 21).

Finally, chemical analysis of HA powder gave a Ca/P ratio of 1.67 characteristic of stoichiometric hydroxyapatite.

At variance, ZnHA nanocrystals exhibit more perturbed shape, ill-defined edges and significantly reduced dimensions (Figure 59), as well as a remarkably increased superficial area (Table 21). HA crystal growth is inhibited by the presence of Zn in solution [51, 60] and, as consequence, the XRD pattern shows a broadening of the diffraction reflections of ZnHA with respect to those of HA (Figure 60). Accordingly, the coherent lengths of the perfect crystalline domains of ZnHA evaluated from the line broadening of the 002 and 310 reflections are significantly reduced with respect to those of pure HA (Table 21).

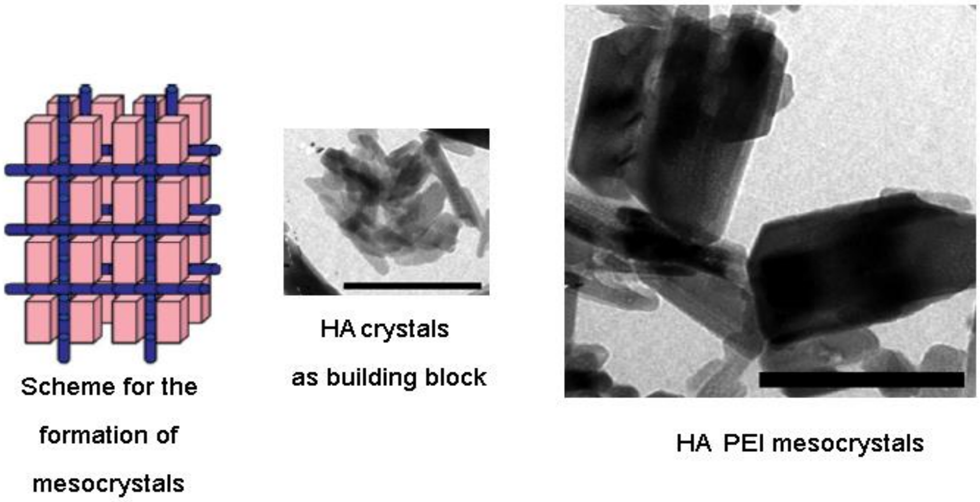

Scheme for the formation of mesocrystals

HA crystals as building block

HA PEI mesocrystals

Figure 58 Scheme for the formation of mesocrystals .

Zn amount into HA nanocrystals is about 7.9 atom % and provokes a reduction of the lattice parameters, in agreement with its smaller ionic radius with respect to that of calcium [230]. Samples obtained by adsorption of PEI on ZnHA nanocrystals, named ZnHAPEI, do not show significant differences with respect to ZnHA in terms of morphology (Figure 59), coherent lengths of the perfect crystalline domains and lattice parameters. Instead, the amount of adsorbed PEI, as well as the value of zeta potential (Table 21), are considerably higher than those of HAPEI.

Table 21 Lattice parameters, coherent lengths (τ_{hkl}) of the perfect crystalline domains in the direction normal to 002 and to 310 planes; Specific surface areas (SSA); Zeta potential; PEI and Zn content of the different apatitic samples synthesized [186].

	a **(Å)**	***c*** **(Å)**	**L 002 (Å)**	**L 310 (Å)**	**PEI content (wt %)**	**Zn content (at %)**	**SSA (m^2/g)**	**Zeta potential (mV)**
HA	9.4378(3)	6.8862(2)	657(4)	311(3)	---	---	23	- 15.6
HAPEI	9.4298(2)	6.8872(2)	929(7)	543(5)	2.4	---	26	+ 26.2
ZnHA	9.4241(9)	6.8696(2)	367(4)	148(3)	---	7.9	86	- 15.3
ZnHAPEI	9.4238(5)	6.8691(4)	365(5)	152(4)	5.9	7.9	86	+30.9

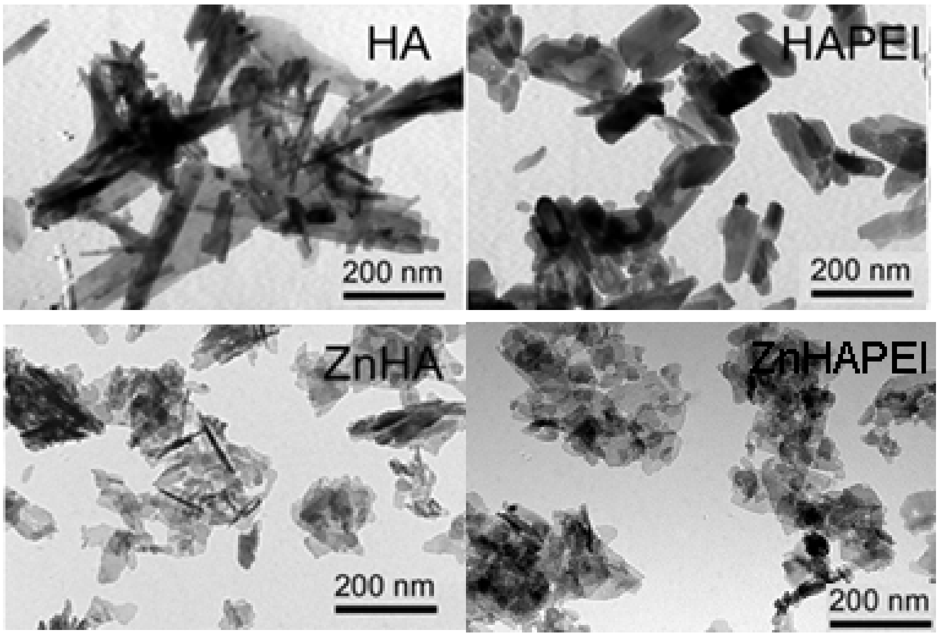

Figure 59 TEM images of the different apatitic samples : HA, HAPEI, ZnHA, ZnHAPEI.

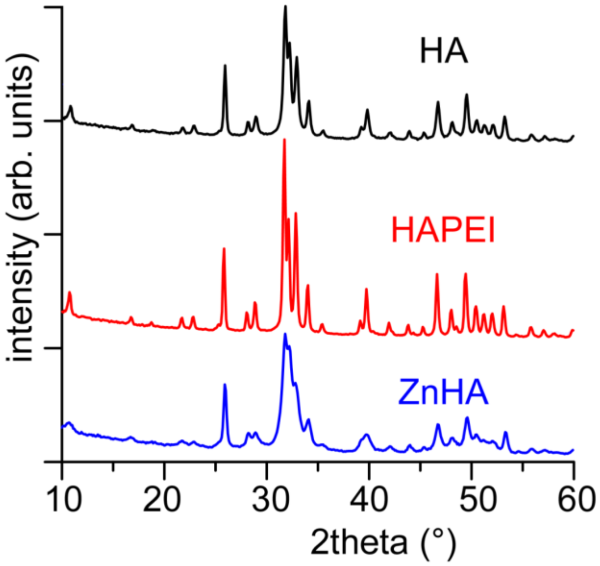

Figure 60 Powder X-ray diffraction patterns of HA, HAPEI and ZnHA [186].

5.5.2 Risedronate adsorption and characterization

The evolution of the amount of risedronate adsorbed on the solids, Q_{ads} (μmol/m^2), from the dilute solutions as a function of the equilibrium BP concentration C_{eq} (0-2 mM) is plotted in Figure 61.

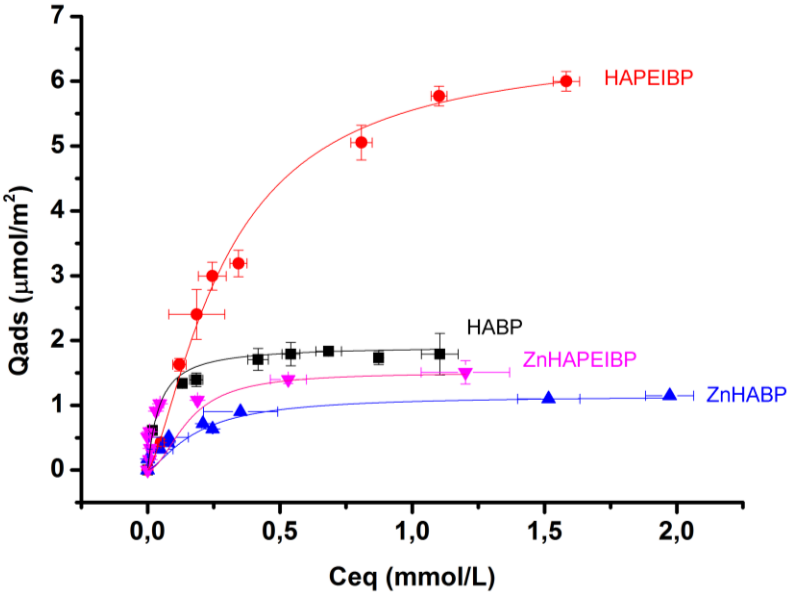

Figure 61 Adsorption isotherms of risedronate on hydroxyapatite (HA), Zn-substituted hydroxyapatite (ZnHA), PEI-modified hydroxyapatite (HAPEI) and PEI modified Zn-substituted hydroxyapatite (ZnHAPEI) at pH 7.4 and 37°C. The data fit the Langmuir isotherm.

The isotherms obtained for HA and ZnHA are Langmuirian in shape (r^2 = 0.87 and 0.94, respectively) showing a high affinity of risedronate for the apatitic surface, because the plateau is reached at relatively low equilibrium concentrations (below 1 mM). Similar observations have been reported in literature for the adsorption of bisphosphonate molecules, as risedronate and tiludronate, on apatitic support [223-225]. Because of the higher specific surface area of ZnHA (86 m^2/g) compared with that of HA (23 m^2/g), the risedronate content reached at plateau in presence of HAZn was more than twice as much as that obtained for HA, (about 40 and 100 μmol/g for HA and HAZn, respectively) (Table 23). The uptake of risedronate depended linearly on the amount of released phosphate ions in solution (Figure 62). Thereby, the adsorption of risedronate on HA can be described as a chemisorption corresponding to an ion exchange process between bisphosphonate molecules in solution and phosphates species on HA. The slope of the curve is close to 1 for

HA and it increases for ZnHA. Indeed the number of phosphate groups released per adsorbed risedronate molecule varies as a function of the characteristics of the apatitic support, as observed in previous studies on BPs adsorption on apatitic substrates [223-225,231]. It can be noticed that the calcium and zinc concentrations in the supernatants after adsorption were low and not affected by the adsorption of risedronate (below 0.5 mM Ca concentrations for HA and HAPEI; below 0.5 mM and 2 mM for Zn and Ca concentrations respectively for ZnHA and ZnHAPEI).

The parameters of adsorption can be determined from the Langmuir equation (1), (Table 22):

$$Q_{ads} = KNC_{eq}1 + (KC_{eq}) \tag{1}$$

where N corresponds to the maximum amount adsorbed of risedronate (μmol/m^2) and K is the affinity constant of risedronate for the solid surface (L/mmol). The values of N and K obtained for the HA and ZnHA supports are (Table 5): 1.88 ± 0.05 and 1.20 ± 0.08 μmol/m^2, respectively, which correspond to the values previously obtained for the adsorption of risedronate molecules on apatitic surface [223]. At the same time, a significant decrease of the affinity K parameter is observed for ZnHA (7 ± 1 L/mmol) compared with HA (21 ± 3 L/mmol) and it can be related to changes in chemical composition.

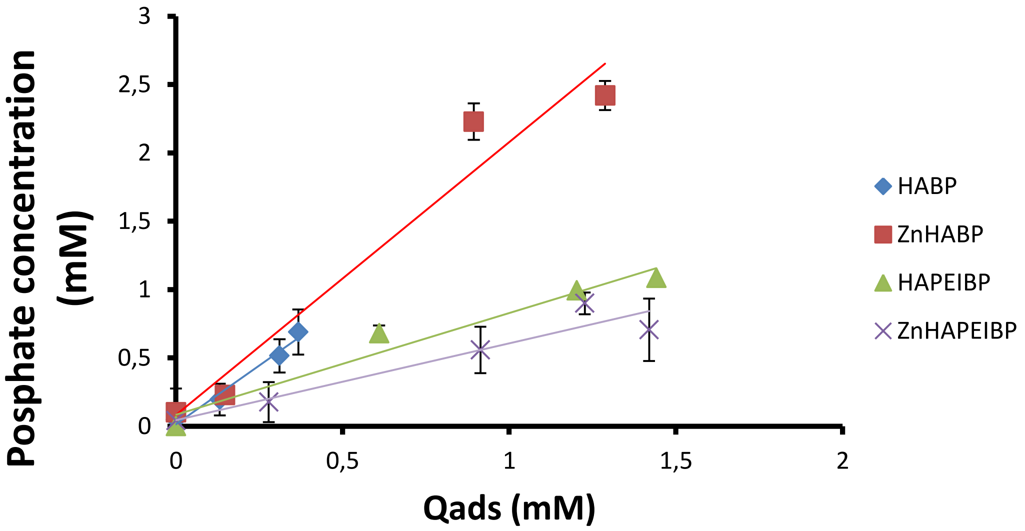

Figure 62 Concentration of phosphate ions in supernatants after adsorption of risedronate on HA, ZnHA, HAPEI and ZnHAPEI

The isotherm of adsorption of risedronate on HAPEI can also be described by the Langmuir model (r^2 = 0.99). The amount adsorbed at saturation, N, was higher on HAPEI (7.9 ± 0.4 μmol/m^2) than on HA and ZnHA but the curve does not reach a plateau even at high equilibrium concentrations in solution (C_{eq}). This can be due to the competition of two mechanisms: a chemisorption process on HA surface and a physisorption process on PEI coating. The decrease of the affinity K for HAPEI (2.2 ± 0.3 L/mmol) (Table 22) can be justified by the presence of PEI on the apatitic surface. The evolution of the amount of risedronate adsorbed as a function of phosphate released in solution is still linear, but the slope appears lower than for HA. The ion exchange process proposed to occur at the surface of the apatite seems to be affected by the presence of PEI. The number of phosphate groups released per BP molecule is lower in the presence of PEI, in agreement with the presence of two different mechanisms of adsorption: chemisorption, which provokes phosphate release, and physisorption, which does not provoke ion exchange. On the other hand, the isotherm of adsorption of risedronate on ZnHAPEI can be described by Freunlich model (r^2=0.82 and n <1). The value of affinity constant K is the lowest compared to the other isotherms and is present also a low quantity of adsorbed risedronate. The simultaneous presence of zinc and polymer might affect the adsorption capacity of the support but the fact that 1/n value is above one could suggest a cooperative adsorption process.

Table 22 Adsorption parameters of risedronate on HA, ZnHA and HAPEI, i.e. maximum amount at saturation (N) and apparent affinity constant (K) calculated from Langmuir equation plots [186].

	N ± ΔN (µmol.m^{-2})	**K ± ΔK (L.mmo1^{-1})**
HA	1.88 ± 0.05	21 ± 3
ZnHA	1.20 ± 0.08	7 ± 1
HAPEI	7.9 ± 0.4	2.2 ± 0.3
ZnHAPEI	-	1.4 ± 0.2

Table 23 Zeta potential of the different apatitic substrates after BP adsorption as a function of risedronate content [186].

	Zeta potential (mV)	**BP (wt.%)**	**BP (µmol/m^2)**	**BP (µmol/g)**
HABP	-12.9	1.2	1.8	41.2
HAPEIBP	+23.5	5.0	6.0	156
ZnHABP	-13.9	3.7	1.15	98.9
ZnHAPEI	+27.6	4.8	1.5	118

XRD analysis of the solid products obtained after bisphosphonate adsorption show that the presence of risedronate does not provoke precipitation of any other crystalline or amorphous phase and does not influence the crystallinity of the apatitic samples (Figure 63). In the insets, the order of plotting has been reversed in order to highlight possible dissimilarity.

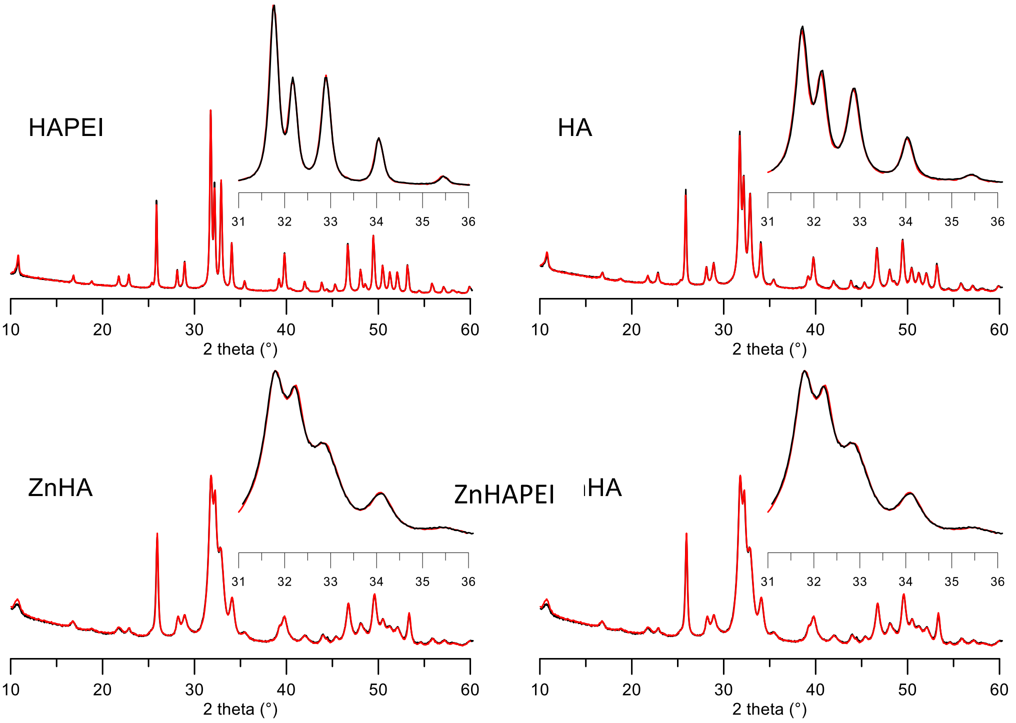

Figure 63 XRD patterns of apatitic samples before (black) and after (red) the adsorption process (Risedronate solution at 3 mM) [186].

Similarly, TEM images of HABP, HAPEIBP, ZnHABP, ZnHAPEIBP show that the different apatitic substrates preserve their initial morphology after risedronate adsorption, as it can be appreciated by comparing the images reported in Figure 59 with those in Figure 64. Adsorption of BP provokes a slight, but appreciable, decrease of the values of zeta potential (Table 23).

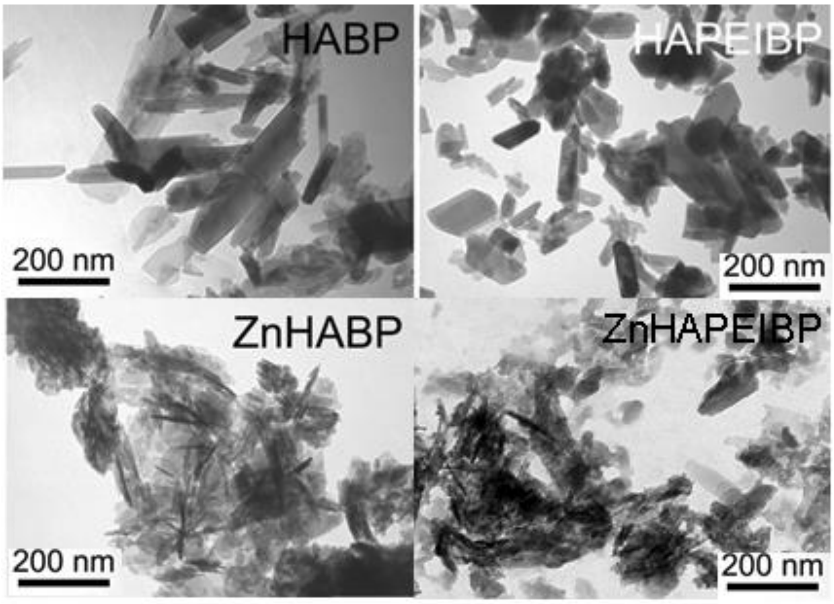

Figure 64 TEM images of the different solid apatite samples obtained after BP risedronate adsorption.

Raman spectra of all apatitic supports after adsorption (Figure 66 and 67) show the characteristic vibration bands of the apatitic structure [232], those of the apatitic phosphate groups: ν_2 (460 cm^{-1}), ν_4 (590-610 cm^{-1}), ν_1 (960 cm^{-1}), ν_3 (1000-1070 cm^{-1}), the OH vibration band at 3560 cm^{-1} [226], and additional bands which can be attributed to the presence of adsorbed BP. In particular, two bands between 2900 and 3000 cm^{-1}, corresponding to C-H stretching, and two intense bands between 1025-1055 cm^{-1}, which might be assigned to C-H pyridine ring deformation, are present. Moreover, the spectra show medium intensity bands between 1500-1600 cm^{-1}, associated with the substituted pyridine ring, and the characteristic Raman bands of phosphonate groups between 850-1230 cm^{-1}. Interestingly, we can see that these bands are shifted compared to those of risedronate sodium salt, indicating a change in the environment of these groups after adsorption. These spectroscopic observations suggest a strong interaction between risedronate molecule and calcium ions at the surface of the apatitic samples after adsorption, as no insoluble calcium salts was observed by XRD and SEM observations. These results are in accordance with the Langmuir model proposed for the adsorption isotherm, and the mechanism of interaction based on ion exchange process.

A shift of the characteristic bands of risedronate is also observed in the Raman spectrum of HAPEIBP and ZnHAPEIBP after adsorption (Figure 67), which confirms that the process of adsorption of BP on the mineral part of HAPEI is similar. Moreover the presence of the vibration bands of PEI molecules (especially stretching vibrations of CH, CH_2 groups between 2800-3000 cm^{-1}) on HAPEIBP and ZnHAPEIBP confirms that PEI is still present on HA surface. Thus, PEI is able to participate to the process of BP adsorption.

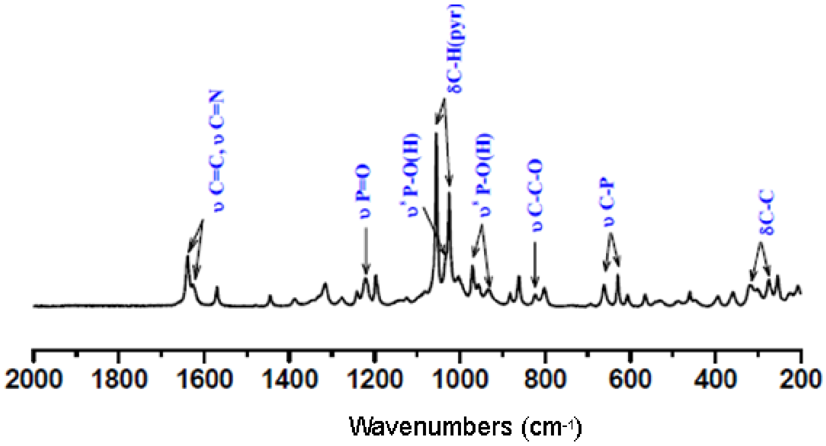

Figure 65 Raman specta of Risedronate

Table 24 Raman attributions of risedronate bands in the range 200-2000 cm^{-1}. The letters indicate the band intensity: m (medium), w (weak), s (strong), sh (shoulder)

Attribution	Wavenumbers (cm^{-1})
δ C-C	276_m, 320_w
ν C-P	629_m, 661_m
ν C-C-O	823_w
δ (P-OH)	862_m
ν_s P-O(H)	932_w,970_m, 1033_{sh}
δ (C-H) pyridine	1024_s, 1054_s
ν P=O	1222_w
δ (C-H) pyridine	1315_m
ν (C=N) ν (C=C) pyridine	1445_w, 1569_m,1625_s,1637_m

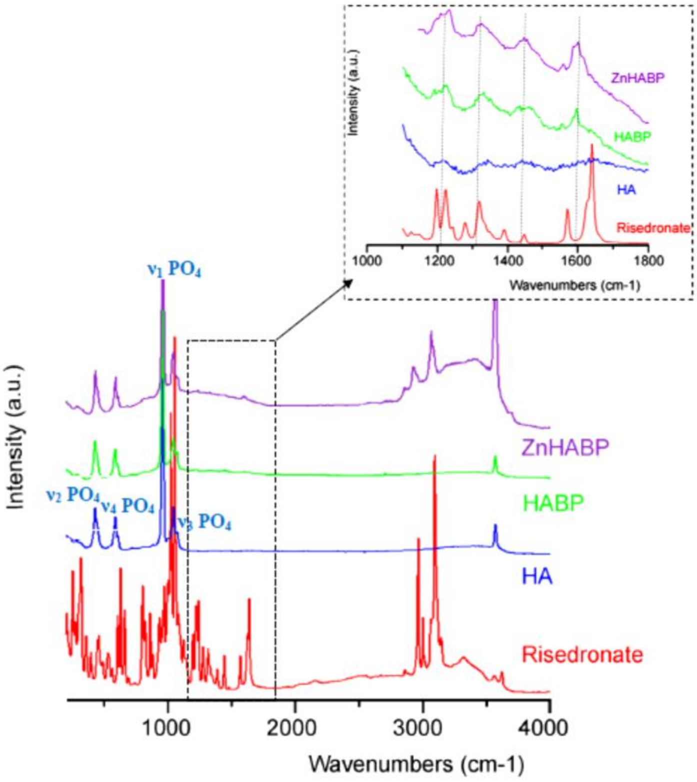

Figure 66 Raman spectra of risedronate sodium salt, HA, HABP and ZnHABP after adsorption (with Qads equal to the maximum value of the adsorption isotherm) [186].

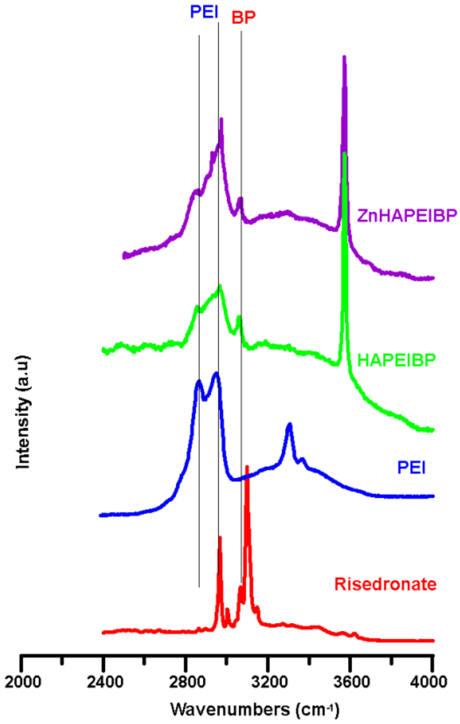

Figure 67 Raman spectra of risedronate sodium salt, PEI, HAPEIBP and ZnHAPEIBP after adsorption (with Qads equal to the maximum value of the adsorption isotherm), in the range 2400-4000 cm^{-1}.

5.5.3 Risedronate release

In Figure 68 is reported the results of risedronate release from the different apatitic supports. The release was fast during the first hour and then slowed down, as observed in previous studies for several apatitic supports [225]. The observed significant differences in the quantity of risedronate released show that the type of support is a determinant parameter controlling BP release.

Various mathematical models can be used to describe and correlate the mechanism of BP release from each support. In the present work, the release data were fitted using the Hixson-Crowell model, which assumes that the release rate is limited by the dissolution of the support, and the Higuchi and Korsmeyer-Peppas models which describe drug release as diffusion process [233].

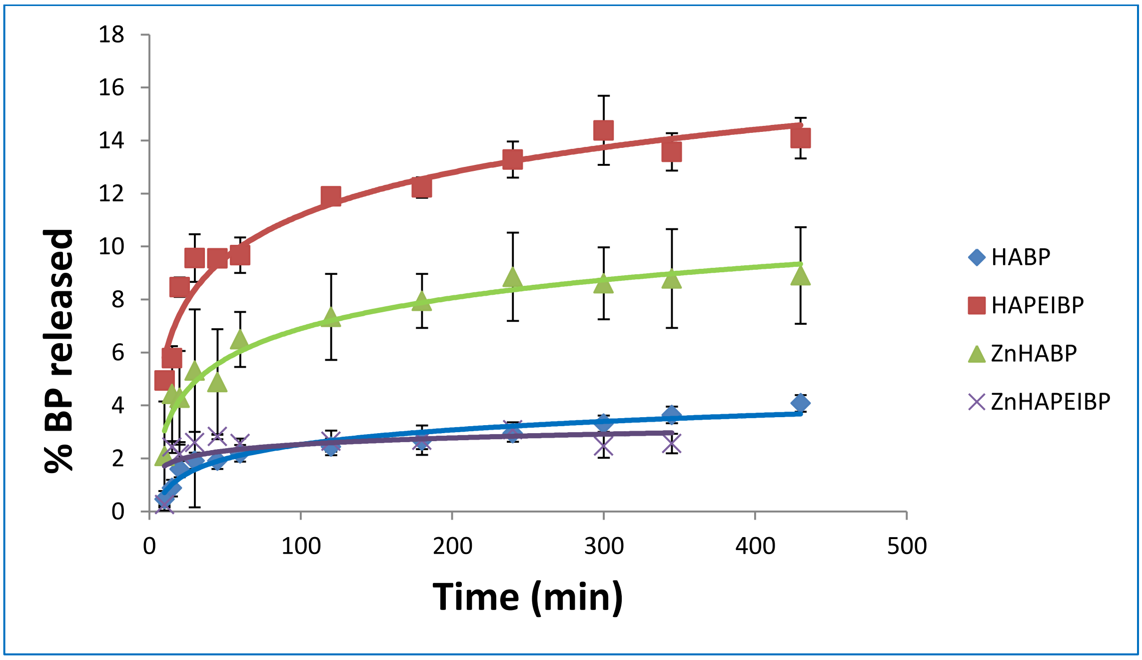

Figure 68 Risedronate (BP) released (wt%) from the different apatitic samples as a function of time.

The Higuchi diffusion model is not sufficient to describe the risedronate release from HA and ZnHA (r^2 = 0.88 and 0.83 from HA and HAZn, respectively, Figure 69a), suggesting another mechanism involving mainly dissolution of the apatitic support [233]. Infact risedronate was slowly released from these apatitic supports because it was irreversibly bound by chemisorption but, at the same time, the release rate was also limited by support dissolution. Moreover, the higher BP release rate observed from ZnHA compared with HA can be attributed to its higher specific surface and solubility.

In contrast, polymeric matrix are usually governed by simple laws of diffusion ($r^2 = 0.98$ for HAPEI, Figure 69a) [233, 234], but the composite nature of the HAPEI suggests the involvement of a secondary mechanism: the fast release, observed during the first hour, is attributed to the release of the drug molecules associated to the organic phase by physisorption and the sequent slow release of BP is due to the dissolution of the apatitic phase. This more complex mechanism of release explains the higher quantity of drug delivered from HAPEI compared with that from HA and ZnHA. The case of ZnHAPEI samples is the most complicated to understand because no mathematical models can be applied (r^2 is really small). In figure 69a, it is showed that the best data fitting is given using a diffusion model (r^2=0.54).

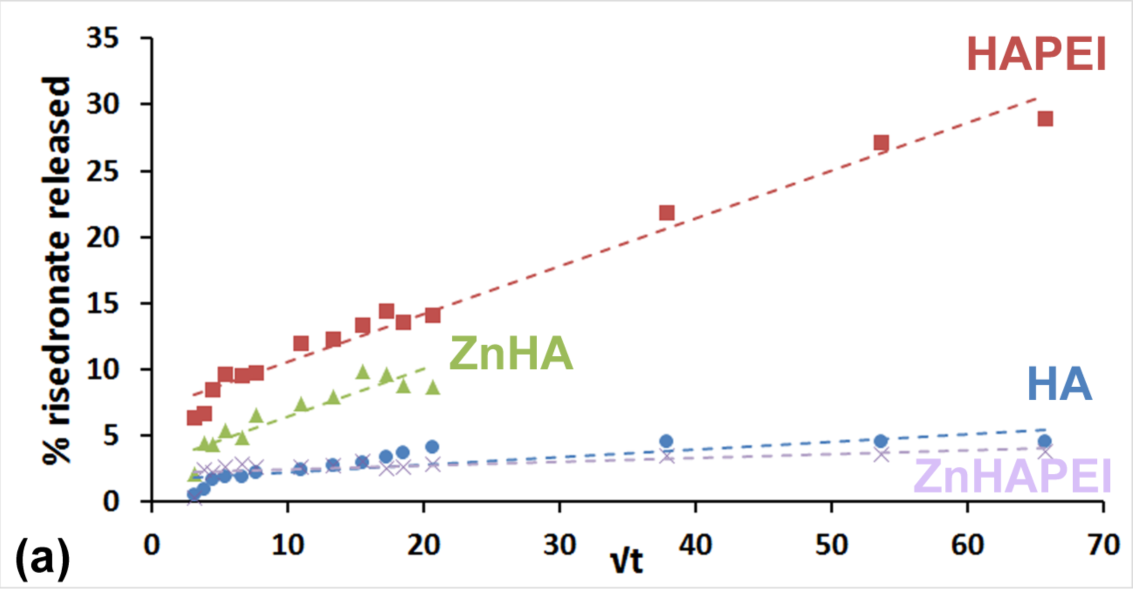

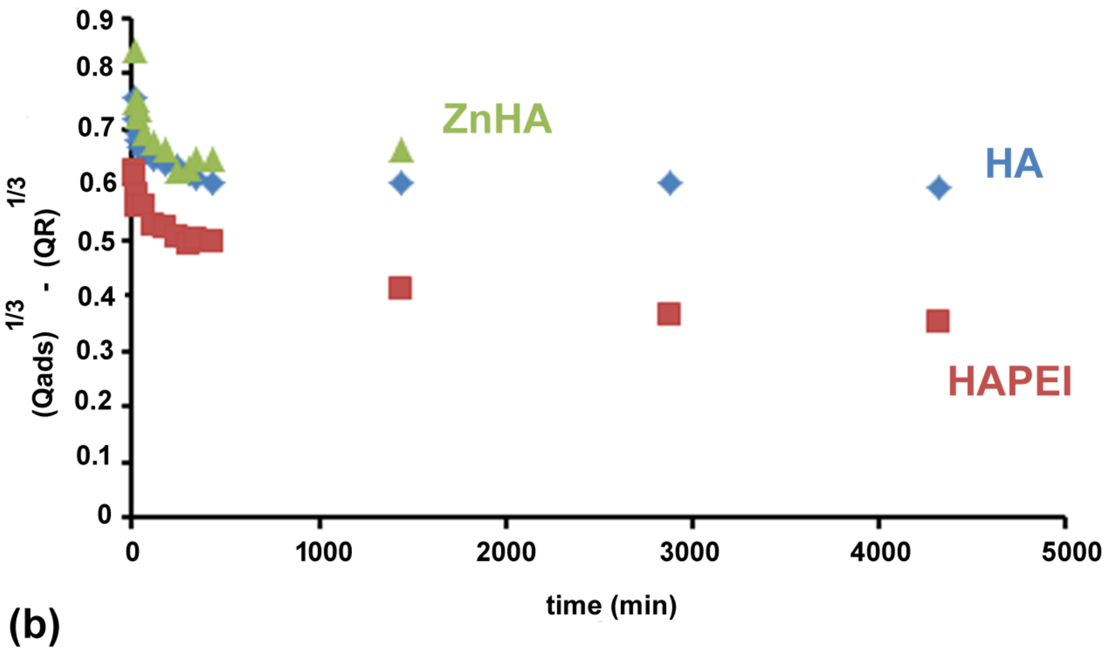

Figure 69 Linear regression of (a) Higuchi model (% BP released = √t) and (b) Hixson–Crowell model (∛Qads - ∛QR = t with QR the quantity of BP released) for the release kinetics of risedronate from HA, HAZn, HAPEI and ZnHAPEI [186].

5.5 *Octacalcium phosphate and α-tricalcium phosphate as supports for Ag nanoparticles*

This study proposes new composite materials based on OCP and α-TCP as supports for AgNPs, using polydopamine (PDA) as functionalizing and reducing agent. The well know antimicrobial properties of silver nanoparticles [235] are used to resolve the relatively high risk of infections associated to medical devices, including CaPs based biomaterials.

The experimental conditions to prepare PDA functionalized OCP and α-TCP at increasing AgNPs contents have been optimized and the influence of the presence of silver nanoparticles on the antibacterial properties of the composite materials has been investigated. Moreover, bone cells response was tested using an in vitro model based on co-culture of mesenchymal stem and endothelial cells.

SEM analysis performed on the samples after immersion in the solution containing dopamine shows a greater amount of the polymer onto α-TCP porous particles than onto OCP flat crystals (Figure 70). However, PDA onto α-TCP appears clustered into aggregates whereas it seems more spread in close contact with the large surface of OCP crystals. Moreover, the samples obtained after immersion for 18 h show a massive dopamine polymerization that occurs without a close relationship with the calcium phosphates.

Thermogravimetric analysis was used to estimate the amount of PDA deposited on OCP and α-TCP : the relative content of PDA was determined as difference between the total weight loss of functionalized samples and that of the pristine calcium phosphates. The data, reported in Table 25, indicate that the amount of deposited PDA increases with immersion time and is significantly higher onto α-TCP than onto OCP. This information is in agreement with SEM images and can be correlated to the different morphology of the two calcium phosphates.

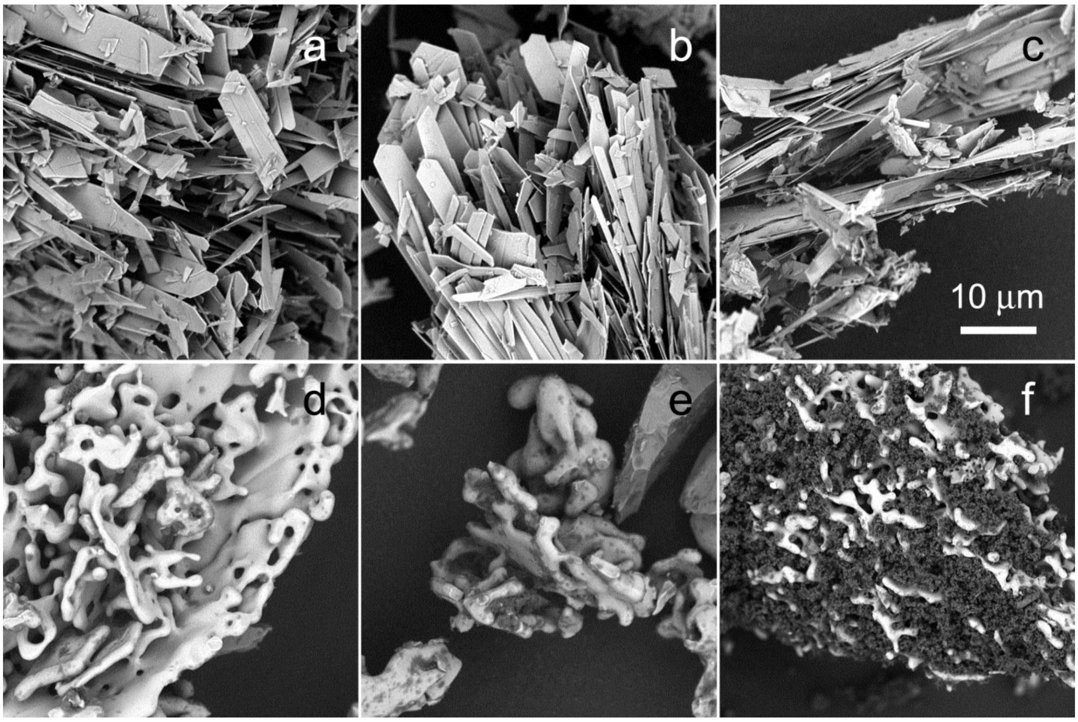

Figure 70 SEM images of (a-c) OCPd and (d-f) α-TCPd after immersion times of (a,d) 1, (b,e) 2 and (c,f) 18 h.

.

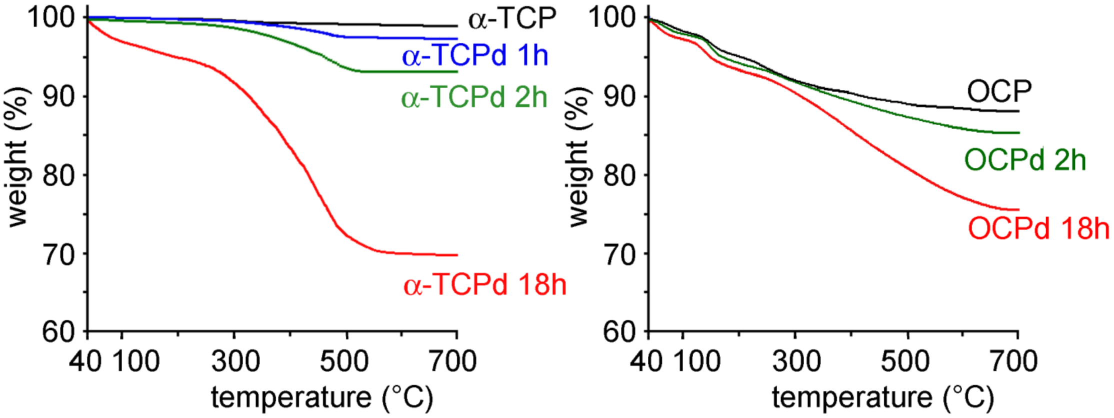

Figure 71 Thermogravimetric plots of the different samples.

Deposition of silver nanoparticles was carried out on functionalized samples obtained using an immersion time of 2 h, as compromise to load a good amount of PDA and to avoid the presence of massive dopamine polymerization.

Table 25 Polydopamine content (determined through thermogravimetric analysis) of the different samples as a function of time. The values of contact angles and water absorption time are also reported.

Substrate	Time (h)	PDA content (wt %)	Static Contact Angle θ (°)	Absorption time (sec)
OCP	-	-	28	2
OCP	1	<1	43	11
OCP	2	2.1	45	>15
OCP	18	10.4	65	>>15
α-TCP	-	-	23	1
α-TCP	1	2.4	32	1
α-TCP	2	6.5	53	3
α-TCP	18	25.7	55	12

The presence of PDA influences the values of contact angle and time required for water complete spreading on the surface, which increase with PDA content (Table 25). This finding is somewhat opposite to what usually verified in other studies where PDA deposition induces a decrease of the contact angle with respect to that of the support [236, 237]. However, at variance with the supports used in these studies, both OCP and α-TCP are highly hydrophilic, in agreement with their low contact angles and water spreading times (Table 25). The modest increase of the values of these parameters on increasing PDA could be ascribed to the less homogeneous surfaces of the composite samples due to the presence of the polymer.

The XRD patterns of the PDA functionalized calcium phosphates after AgNPs deposition show the characteristic reflections of OCP and α-TCP, respectively, together with reflections at about 38.1° and at about 44.5 ° of 2θ corresponding to the most intense peaks of silver (Figure 72). The relative intensity of these reflections increases with the concentration of the $AgNO_3$ solution used for the deposition. The presence of AgNPs onto the surface of functionalized OCP and α-TCP is clearly appreciable also in the SEM images of the composite materials, as shown in Figure 73.

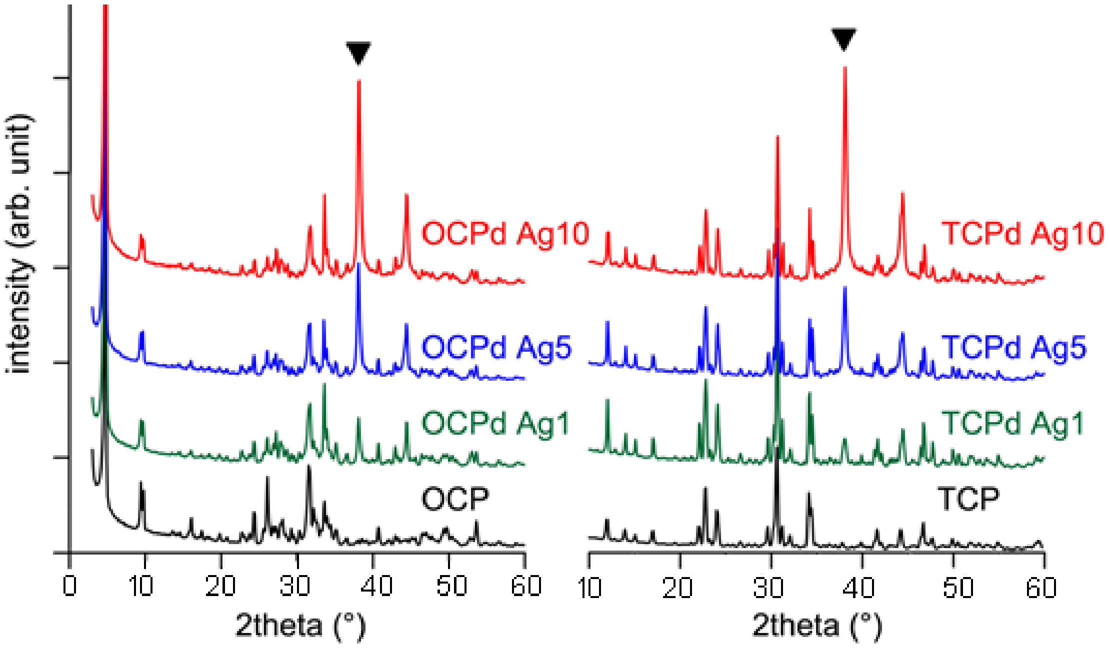

Figure 72 XRD patterns of the different samples. The relative intensity of this reflection increases on increasing the concentration of the silver nitrate solution.

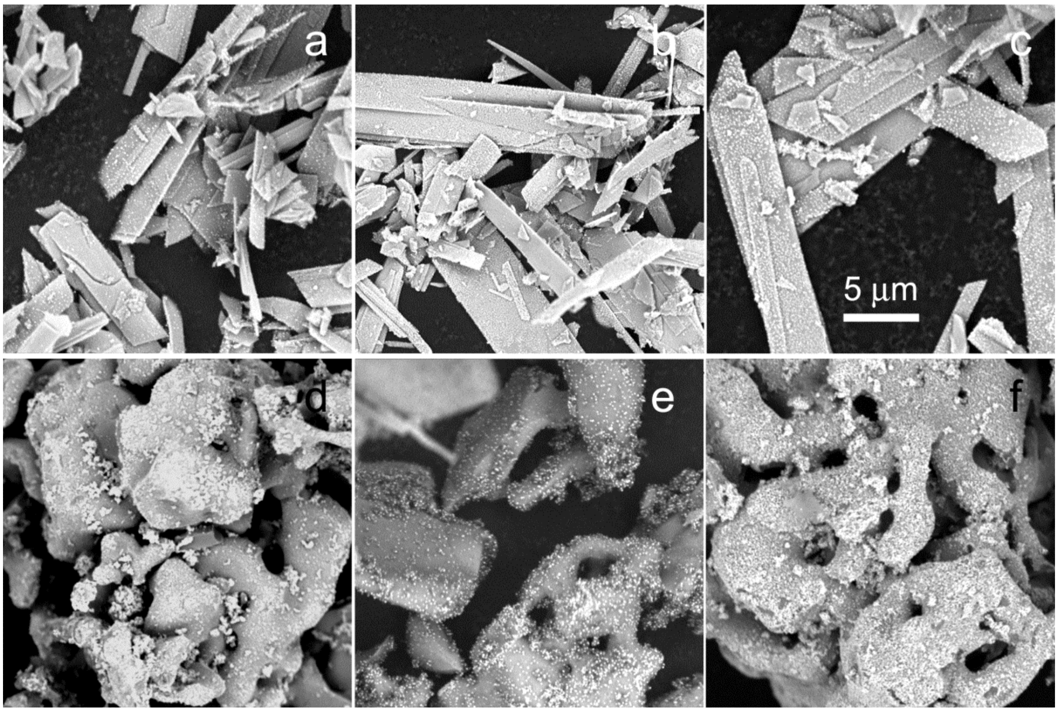

Figure 73 SEM images of (a) OCPdAg1, (b) OCPdAg5, (c) OCPdAg10, (d) α-TCPdAg1, (e) α-TCPdAg5, (f) α-TCPdAg10.

Table 26 Ag content (wt%) determined through AAS analysis in solid samples after immersion of OCPd and α-TCPd into solutions at different concentration of $AgNO_3$

Samples	**Ag content (wt %)**
OCPdAg1	1.6
OCPdAg5	8.2
OCPdAg10	11.6
α-TCPdAg1	0.8
α-TCPdAg5	4.7
α-TCPdAg10	6.8

The results of ICP analysis, reported in Table 26, indicate that the amount of AgNPs associated to OCPd and α-TCPd increases with silver concentration in solution up to about 11.6 and 6.8 wt%, respectively. The greater deposition of AgNPs onto OCPd cannot be ascribed to a greater presence of PDA, since its content its smaller than on α-TCPd, and it might be due to the morphology of huge plate-like crystals of octacalcium phosphate, which favors a more homogeneous deposition of PDA, and, as a consequence, of AgNPs.

*5.6 **Antiresorption implant coating based on calcium alendronate and octacalcium phosphate deposited by matrix assisted pulsed laser evaporation (MAPLE)***

The chemistry and the physic of a bone implant surface are fundamental for the good integration and the success of a synthetic implantation with the natural bone tissue.

In this study, AL indicates the crystalline form of calcium alendronate monohydrate, which was obtained by calcium sequestration from octacalcium phosphate CaAL•H_2O [210, 238]. In the crystal structure of CaAL · H_2O the molecules are arranged at the origin and center of the unit cell and are organized in a network interlinked along the *c* -axis, with the water molecule relatively far from the metal atom, 3.6 Å (Figure 74). The calcium atom is coordinated to six oxygen atoms belonging to phosphonate groups in a distorted octahedral geometry, with distances in the interval 2.2÷2.7 Å and mean distances (2.4 Å) very close to Ca-O mean distances in OCP.

Calcium alendronate, especially when associated to octacalcium phosphate (OCP), exhibits a remarkable inhibition of osteoclast proliferation and activity, whereas it enhances osteoblast differentiation [210].

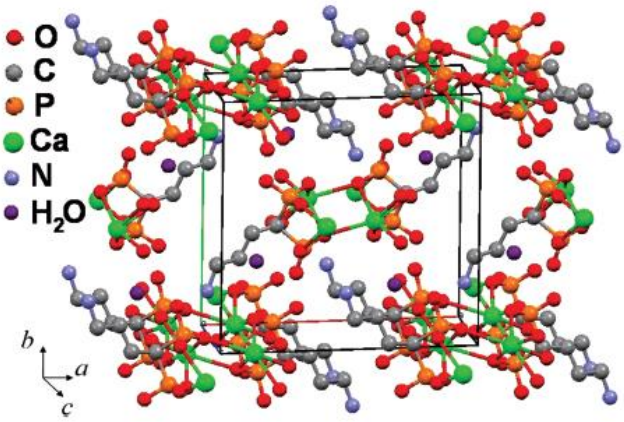

Figure 74 a view of CaAL*H20 structure [210].

Using MAPLE technique to deposit thin films of OCP, at different contents of CaAL•H_2O, on titanium (Ti) substrates, it was explored the possibility to create coatings able to offer a suitable interface for bone tissues thanks to the presence of OCP, and to provide a local availability of BP. In fact, although metallic materials, such as Ti, fulfill the requirements of a successful orthopaedic implant, in terms of strength, toughness and resistance to wear and corrosion [239], incomplete osteointegration and stress shielding are the main causes of bone implant failures [240]. Coating the metallic surface with a thin film of calcium phosphate improves implant fixation to hard tissues [241, 242].

5.6.1 Characterization of the crystalline powders

The amount of CaAL*H_20 in the composite material was tailored varying the concentration of alendronate in solution in order to have, in the final solid samples, 48 wt% and 100 wt% of CaAL*H_2O respectively in the sample AL8 and AL20.

In agreement, the XRD patterns (Figure 75) show that in the sample AL8 are present both characteristic peaks of OCP and of CaAL*H_2O whereas calcium alendronate monohydrate is the unique crystalline phase in the sample AL20. From a morphological point of view, SEM images show that the sample AL8 is a mixture of big plate like crystals, characteristic of OCP, and of tiny long road-like crystals characteristic of CaAL*H_2O. The sample AL20 presents only calcium alendronate monohydrate crystals (Figure 76).

The FTIR absorption spectra reported in Figure 77 confirm the different composition of the samples. The spectrum of pure OCP displays the absorption bands in the regions 1100–1000 cm^{-1} and 630–450 cm^{-1}characteristic, respectively, of PO4 stretching and bending. The bands in the range 1300 and1100 cm^{-1}, and 960 and 840 cm^{-1}, are characteristic of HPO_4^{2-} stretching [243]. The spectra of the sample AL20 show the absorption bands at 1135 and 1094 cm^{-1}which are associated to O-P-O and C-C-O bond stretching, whereas the bands at 940–916 cm^{-1} are connected only to motion of O-H-O and H-O-P, while the 613–580 cm^{-1} absorption bands are related to modes of the phosphate group [244]. The FTIR spectrum of AL8 clearly indicates the contribution of both OCP and AL.

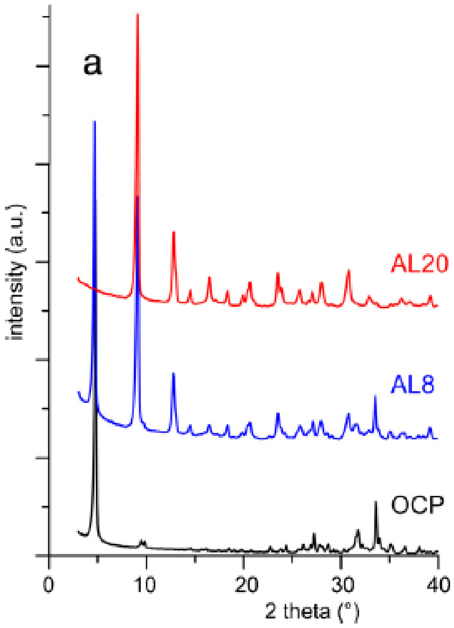

Figure 75 X-ray diffraction patterns of crystalline powders obtained at increasing AL concentration in solution [246].

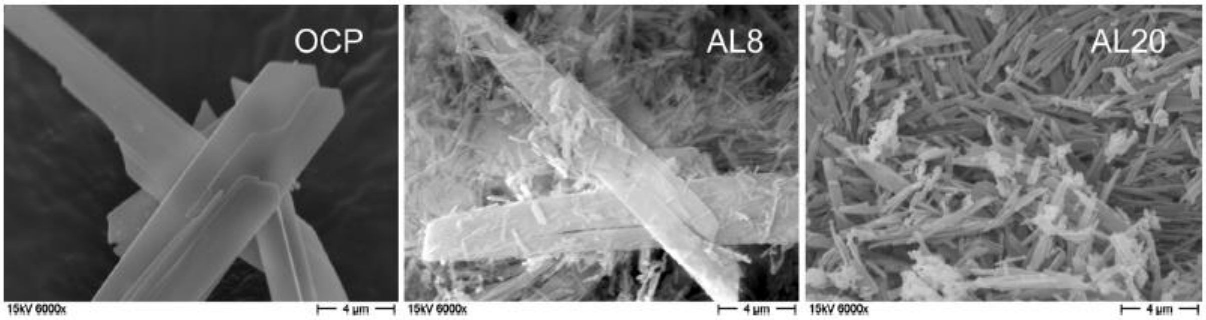

Figure 76 SEM images of crystalline powders showing characteristic morphologies of the two component crystalline phases: OCP and CaAL•H2O [246].

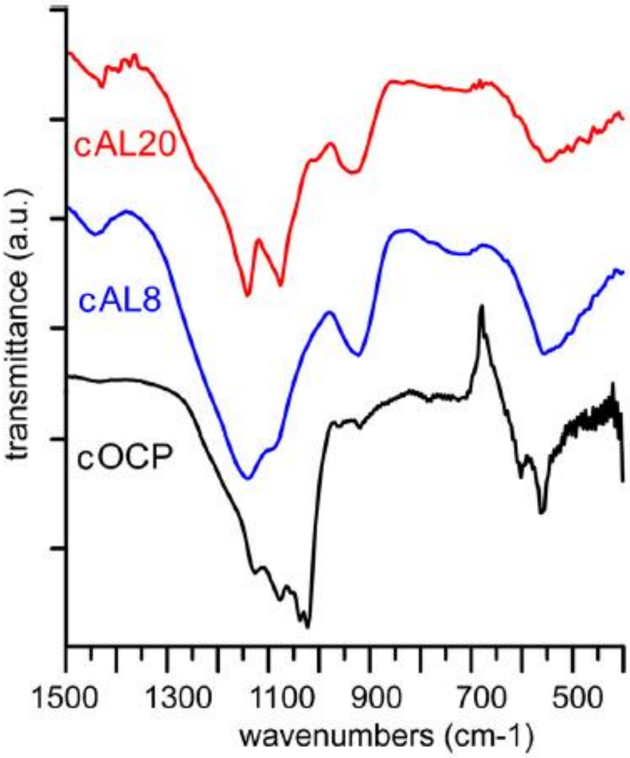

Figure 77 FT-IR spectra of thin coatings obtained after MAPLE transfer of different crystalline powders [246].

5.6.2 Structural and morphological characterization of the coatings

The XRD patterns of the thin films confirm the data obtained by XRD analysis of the powder. At low angle, the X-ray diffraction pattern of cOCP thin film presents just the characteristic peak of OCP at 4.7° 2θ, whereas the XRD pattern of cAL20 shows just a peak at 9.1° 2θ, in agreement with the presence of CaAL•H_2O as the unique crystalline phase. The contribution of both crystalline phases, OCP and CaAL•H_2O, can be discriminated in the XRD pattern of cAL8. Similarly, the crystalline phases present in the different thin films can be identified also by FTIR absorption spectra (Figure 78), even if the absorption bands are generally less resolved with respect to those shown in the spectra of the corresponding powder samples.

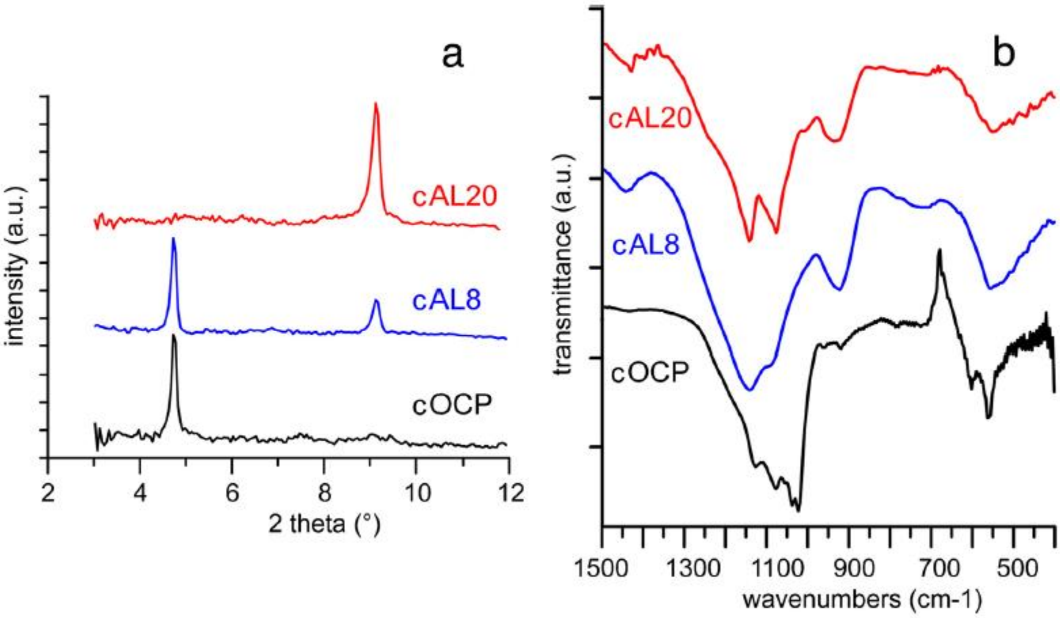

Figure 78 X-ray diffraction patterns (a) and FT-IR spectra (b) of thin coatings obtained after MAPLE transfer of different crystalline powders [246].

AFM analysis was used to calculate the roughness parameter of the coatings. Roughness parameters, namely arithmetic mean roughness (Ra), root-square roughness(Rq), and the vertical distance between the highest and lowest points within the evaluation length (Rt), were recorded. The results indicate that there is no significant difference between the samples cOCP, cAL8, cAL20. Average values were: Ra = 0.211 ± 0.011 μm, Rq = 0.170 ± 0.007 μm, Rt = 1.288 ± 0.010 μm.

The coating thickness was evaluated by profilometry using a stylus profiler XP2 from Ambios Technology. For this investigation, half of Ti substrate was shielded with tape during deposition in order to evaluate the level difference between top of the coating and uncoated Ti. A continuous scanning with 10 m s^{-1}speed was used for depth evaluation from the top to the bottom of the coatings (Ti uncoated surface after tape removal). The result of the thickness measurement is similar in all the three samples and the value is around 100 nm.

SEM images of the cOCP thin films display a quite homogeneous surface and the presence of crystal fragments, together with cauliflower-like aggregates and droplets, are evidently visible at higher magnification (Figure 79). SEM images of cAL8 films show much smaller rod-like crystals, clearly discernible from the big plate-like crystals of pure OCP. These small crystals, which display the characteristic morphology of CaAL•H_2O [210], are the only ones which can be distinguished in SEM images of cAL20 thin films.

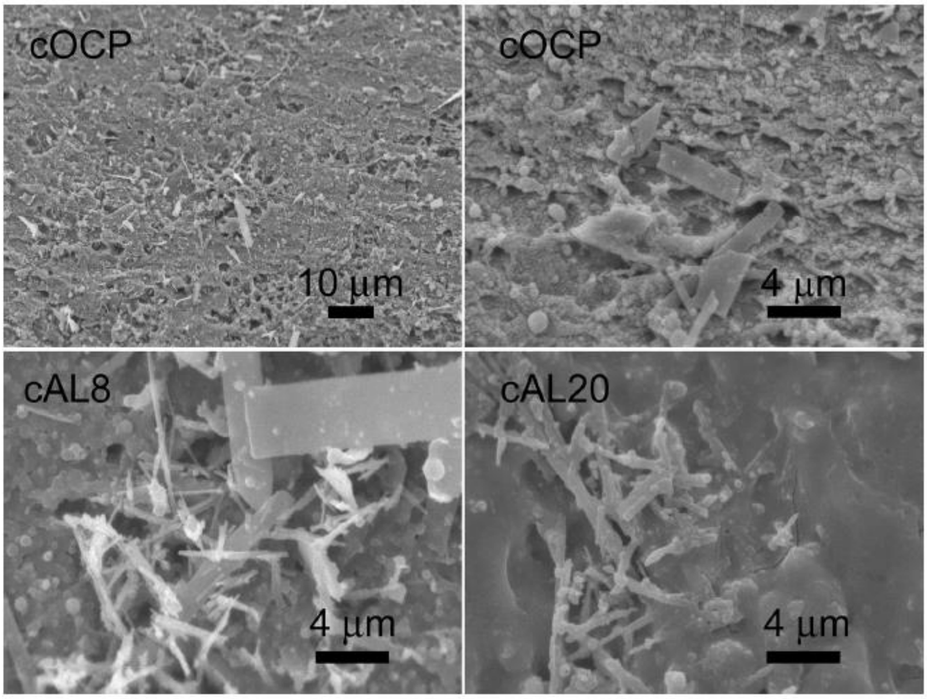

Figure 79 SEM images of coatings displaying the characteristic morphologies of the two component crystalline phases – OCP and CaAL•H2O – after MAPLE transfer [246].

Calcium release test, in physiological solution, was performed to evaluate the degradation of the coatings. The results, reported in Figure 80, are in agreement with the different solubility of CaAL•H_2O and OCP [61, 245], and indicate that Ca release from cAL20 is about14 mg/L after 6 h and it increases up to about 18 mg/l at 2 days, after which it remains constant. Ca release from cOCP is much lower, whereas the amounts released from cAL8 assume intermediate values.

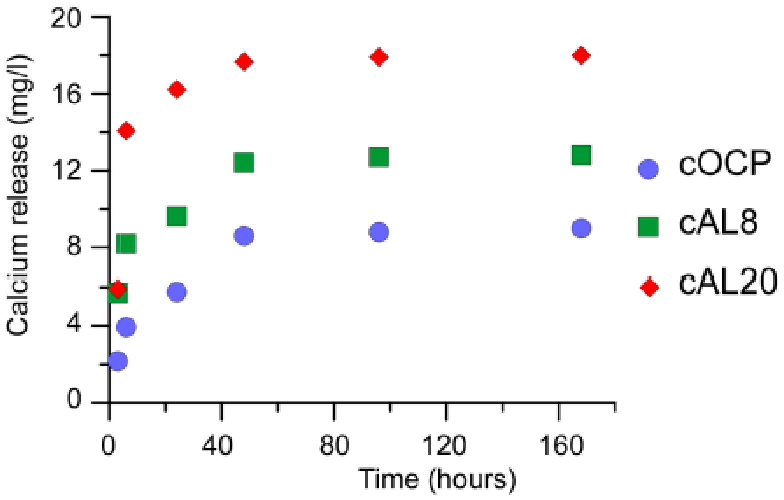

Figure 80 Calcium cumulative release from cOCP, cAL8 and cAL20 as a function of soaking time in physiological solution. Each value was determined in triplicate. The standard deviations do not exceed the size of the symbols [246].

The biological performance of the coatings was investigated through *in vitro* tests carried out using co-cultures of osteoblast derived from stem cells and osteoclast derived from monocytes of osteoporotic subjects.

The results show that the presence of calcium alendronate in the coatings dramatically inhibits proliferation, differentiation and activity of osteoporotic osteoclast. On the contrary, the bisphosphonate does not affect osteoblast viability, and it promotes their activity. Osteoblast differentiation is further enhanced when the coating is a composite of CaAL•H2O and OCP, most likely thanks to the good bioactivity of OCP.

6. Conclusions

The aim of this PhD thesis was to develop new functionalized materials for the local treatment of bone diseases and to study the effects of ions and molecules on the synthesis, stability, crystal growth and structure of some of the most common calcium phosphates used for hard tissue repair, namely HA, OCP, DCPA and TCP. The functionalized agents taken into consideration include molecules from the family of Bisphosphonates (alendronate, zoledronate and risedronate), synthetic drugs with a well known anti-osteoporotic activity, quercetin, which is a natural molecule present in several fruits and herbs and displays relevant anti-oxidant properties, and Silver nanoparticles to provide antibacterial properties.

The adsorption and the release mechanisms of bisphosphonates on CaPs was investigated through the study of the interaction of risedronate with four different hydroxyapatite-based supports with modulated composition and surface charge. The results of the study indicate that the isotherms of adsorption of risedronate on HA and on a partial Zn substituted apatite (ZnHA) were both Langmuirian in shape, but risedronate content on ZnHA at plateau was about twice with respect to HA, because of the higher specific surface of ZnHA. The mechanism of adsorption can be explained by ionic exchange between bisphosphonate molecules in solution and phosphate on the surface of apatitic supports. HA and ZnHA positive surface charges were enhanced through functionalization of the apatitic phase with a polycationic polymer containing amino groups, polyethyleneimine (HAPEI and ZnHAPEI). The isotherm of adsorption of risedronate on HAPEI can also be described by the Langmuir model. The amount adsorbed at saturation was higher on HAPEI than on the other supports, but the plateau was not reached even at high equilibrium concentrations in solution. The ion exchange process proposed at the surface of the apatite seems to be affected by the presence of PEI. On the contrary, the isotherm of adsorption of risedronate on ZnHAPEI can be described by Freundlich model. Risedronate presents a lower affinity with the substrate ZnHAPEI compared to the other supports, which is testified also by the relative low quantity of adsorbed risedronate. Probably the simultaneous presence of zinc and polymer might affect the adsorption capacity. Similarly to the adsorption process, the risendronate release is related to the nature of the apatitic supports, as shown by the higher amount of bisphosphonate released from HAPEI than from HA, ZnHA and ZnHAPEI substrates. Enhancement of positive charge on the surface of the HA nanocrystals, thanks to the presence of the polycationic polymer (PEI), promotes the adsorption of negatively charged BPs from solution and controls their release. Thus, it is possible to tailor risedronate adsorption and to control its release rate through modulation of the solubility and the chemical composition of the apatitic supports.

Two different BPs, the powerful alendronate and zoledronate, were chosen to functionalize octacalcium phosphate (OCP), which is considered the precursor phase of biological apatites. The direct synthesis allows to get a single crystalline phase up to a zoledronate and alendronate content of 3.5 and 5.2 wt%, respectively. The incorporation of both bisphosphonates provokes a slight decrease of the mean length of the coherent scattering domains, as well as morphological modifications that suggests a preferential interaction with the (0k0) faces of OCP. However, release data suggest a stronger interaction of ZOL than AL with OCP structure. The *in vitro* tests suggest that zoledronate and alendronate maintain their antiresorptive and anti-tumor properties even when incorporated into OCP.

Alendronate in the form of calcium alendronate monohydrate ($CaAL{\bullet}H_2O$), obtained by calcium sequestration from octacalcium phosphate, was used also to deposit composite thin films on titanium substrates. Calcium alendronate monohydrate and calcium alendronate monohydrate/octacalcium phosphate as composite materials were transferred on the metallic surface by the Matrix-Assisted Pulsed Laser Evaporation (MAPLE) technique. The composite materials contained different amounts of $CaAL{\bullet}H_2O$, which were tailored by varying alendronate concentration in solution; the relative content of $CaAL{\bullet}H_2O$ in the final solid samples amounts to 48 wt% for AL8 (the remaining 52 wt% is still OCP) and to 100 wt% for AL20. SEM images of the thin films deposited by MAPLE display a quite homogenous surfaces and evidence the presence of big plate-like crystals of OCP and much smaller rod-like crystals, characteristic of $CaAL{\bullet}H_2O$. The results indicate that MAPLE technique allows to develop implant coatings, which can provide not only a suitable interface for bone growth but also offer the availability of drugs able to prevent undesirable excessive bone resorption.

Quercetin-functionalized HA was prepared following two different procedures: direct synthesis and through phase transition from monetite. Direct synthesis lead to functionalized nanocrystals containing up to 3.1 wt% quercetin, which provoked a reduction of the crystals mean dimensions and of the length of the coherently scattering domains. The synthesis conditions provoked degradation of quercetin and, as a consequence, a significant reduction of its radical scavenging activity (RSA). Synthesis through phase transition yielded samples containing up to 1.3 wt% of quercetin incorporated into hydroxyapatite, with minor structural modifications. RSA values of these products reach levels of about 40% (pure quercetin exhibits RSA values varying from 45% to 50% as a function of concentration) confirming that the antioxidant activity of quercetin is maintained. These materials were submitted to *in vitro* cell tests using a tri-culture model, showing a positively influence on bone repair microenvironment and a stimulating effect on osteoblast proliferation and activity.

The possibility to functionalize different calcium phosphate substrates with quercetin was also investigated through adsorption from solution. Interaction of quercetin with hydroxyapatite (HA), hydroxyapatite modified with alendronate (HAAL), monetite (DCPA) and strontium substituted monetite (SrDCPA) yielded samples with greater amounts of quercetin content, up to 6wt% in the case of HA. At variance with the results obtained through direct synthesis, the softer procedure conditions do not provoke any oxidation process, and the functionalized materials display high values of RSA.

Finally, taking into account the relatively high risk of infections associated to medical devices, calcium phosphate based materials have been designed as supports for silver nanoparticles (AgNPs), using polydopamine (PDA) as functionalizing and reducing agent. The results of thermogravimetric analysis show that the amount of deposited PDA is significantly higher onto α-TCP (6.5 wt%) than onto OCP (2.1 wt%), as confirmed by SEM images. AgNPs deposition on the PDA functionalized calcium phosphates can be revealed through XRD analysis, since the diffraction patterns show the characteristic reflections of OCP and α-TCP and the most intense peaks of silver. The relative intensity of silver reflections increases with the concentration of the $AgNO_3$ solution used for the deposition. ICP analysis indicates that the amount of AgNPs associated to OCPd and α-TCPd increases with silver concentration in solution up to about 11.6 and 6.8 wt%, respectively. The greater deposition of AgNPs onto OCP might be due to the morphology of huge plate-like crystals of octacalcium phosphate, which favors a more homogeneous deposition of PDA, and, as a consequence, of AgNPs.

Most of the materials developed in this PhD thesis have been submitted to biological in vitro tests, which generally indicated that the peculiar characteristics of the functionalized agents are maintained when incorporated into CaPs, so that these materials can be considered potential candidates for the local treatment of bone defects.

7. Bibliography

[1] Breusch SJ, Kühn KD, *Bone cements based on polymethylmethacrylate*. Orthopade, **32** (2003), 41-50.

[2] Ulery BD, Nair LS, Laurencin CT, *Biomedical application of biodegradable polymers*. J Polym Sci Part B: Polym Phys, **49** (2011), 832-864.

[3] Dee KC, Bizios R, *Mini-review: Proactive biomaterials and bone tissue engineering*. Biotechnology and Bioengineering, **50** (1996), 438-442.

[4] Buma, P, Schreurs W, Verdonschot N, *Skeletal tissue engineering from in vitro studies to large animal models*. Biomaterials, **25** (2004), 1487–1495.

[5] Mistry AS, Mikos AG, *Tissue engineering strategies for bone regeneration*. Advances in Biochemical Engineering/Biotechnology, **94** (2005), 1–22.

[6] Mont MA, Ragland PS, Biggins B, Friedlaender G, Patel T, Cook S, Etienne G, Shimmin A, Kildey R, Rueger DC, Einhorn TA, *Use of bone morphogenetic proteins for musculoskeletal applications. An overview*. Journal of Bone and Joint Surgery, **86** (2004), 41–55.

[7] Boix T, Gómez-Morales J, Torrent-Burgués J, Monfort A, Puigdomènech P, Rodríguez-Clemente R, *Adsorption of recombinant human bone morphogenetic protein rhBMP-2m onto hydroxyapatite*. Journal of Inorganic Biochemistry, **99** (2005), 1043-1050.

[8] Niu X, Feng Q, Wang MG, Zheng Q, *Porous nano-HA/collagen/PLLA scaffold containing chitosan microspheres for controlled delivery of synthetic peptide derived from BMP-2*. Journal of Controlled Release, **134** (2009), 111-117.

[9] Chu TMG, Warden SJ, Turnera CH, Stewart RL, *Segmental bone regeneration using a load-bearing biodegradable carrier of bone morphogenetic protein-2*. Biomaterials, **28** (2007), 459–467.

[10] Otsuka M, Matsuda Y, Fox JL, Higuchi W, *A novel skeletal drug delivery system using self-setting calcium phosphate cement. 9: Effects of the mixing solution volume on anticancer drug release from homogeneous drug-loaded cement*. J Pharm Sci, **6** (1995), 733-736.

[11] Otsuka M, Matsuda Y, Suwa Y, Fox JL, Higuchi W, *A novel skeletal drug delivery system using self-setting calcium phosphate cement. 3: Physicochemical properties and drug release of bovin insulin and bovin albumin*. J Pharm Sci, **83** (1994), 255-258.

[12] Gautier H, Chamblain V, Weiss P, Merle C, Bouler JM, *In vitro characterization of calcium phosphate biomaterials loaded with lidocaine hydrochloride and morphine hydrochloride*. J Mater Sci: Mater Med, **21** (2010), 3141-3150.

[13] Suzuki Y, Tanihara M, Nishimura Y, Suzuki K, Kakimaru Y, Shimizu Y, *A new drug delivery system with controlled release of antibiotic only in the presence of infection*. J Biomed Mater Res, **42** (1998), 112-116.

[14] Salgado AJ, Coutinho OP, Reis RL, *Bone tissue engineering: State of the art and future trends*. Macromol Biosci, **4** (2004), 743-765.

[15] Palmer LC, Newcomb CJ, Kaltz SR , Spoerke ED, Stupp SI, *Biomimetic Systems for Hydroxyapatite Mineralization Inspired By Bone and Enamel.* Chem Rev, **108** (2008), 4754-4783.

[16] Weiner S, Wagner HD, *The material bone: Stucture and mechanical function relations*. Annu Rev Mater Sci, **28** (1998**)**, 271-298.

[17] Feng JQ, Ward LM, Liu S, Lu Y, Xie Y, Yuan B, YuX, Rauch F, Davis SI, Zhang S, Rios H, Drezner MK, Quarles RD, Bonewald LF, White KE, *Loss of DMP1causes rickets and osteomalacia and identifies a role for osteocyte in mineral metabolism*. Nat Genet, **38** (2006**)**, 1310-1315.

[18] Schmidt WJ, *Uber die Kristallorientierung im Zahnschmelz*. Naturwissenschaften, **24** (1936**)**, 361-361.

[19] Manolagas SC, *Birth and death of bone cells: basic regulatory mechanisms and implications for the pathogenesis and treatment of osteoporosis.* Endocr Rev, **21** (2000), 115-137.

[20] Ecarot-Charrier B, Glorieux FH, Van Der Rest M, Pereira G, *Osteoblasts isolated from mouse calvaria initiate matrix mineralization.* J Cell Biol, **96** (1983), 639–643.

[21] Balcerzak M, Hamade E, Zhang L, Pikula S, Azzar G, Radisson J, Bandorowicz- Pikula J, Buchet R, *The roles of annexins and alkaline phosphatase in mineralization process*. Acta Biochim Pol, **50** (2003**)**, 1019-1038.

[22] Lanyon LE, *Osteocytes, strain detection, bone modeling and remodeling*. Calcif Tissue Int, **53** (Suppl. 1) (1993**)**, S102.

[23] Va¨a¨na¨nen HK, Zhao H, Mulari M, Halleen JM, *The cell biology of osteoclast function*. J MJ Cell Sci, **113** (2000**)**, 377-381.

[24] Teitelbaum SL, *Bone resorption by osteoclasts.* Science, **289** (2000**)**, 1504-1508.

[25] Gowen M, Lazner F, Dodds R, Kapadia R, Feild J, Tavaria M, Bertoncello I, Drake F, Zavarselk S, Tellis I, Hertzog P, Debouck C, Kola I, *Cathepsin K knockout mice develop osteopetrosis due to a deficit in matrix degradation but not demineralization*. J Bone Miner Res, **14** (1999), 1654-1658.

[26] Boanini E, Gazzano M, Bigi A, *Ionic substitutions in calcium phosphates synthesized at low temperature*. Actabiomaterialia, **6** (2010), 1882-1894.

[27] Raj PA, Johnsson M, Levine MJ, Nancollas GHJ, *Salivary statherin. Dependence on sequence, charge, hydrogen bonding potency, and helical conformation for adsorption to hydroxyapatite and inhibition of mineralization*. Biol Chem, **267** (1992), 5968-5976.

[28] Lijun W, Nancollas GH, *Calcium Orthophosphates: Crystallization and Dissolution*, Chem Rev, **108** (2008), 4628-4669.

[29] Johnsson MSA, Nancollas GH, *The role of brushite and octacalcium phosphate in apatite formation*. Crit Rev Oral Biol Med, **3** (1992), 61-82.

[30] Lynn AK, Bonfield W, *A novel method for the simultaneous, titrant-free control of pH and calcium phosphate mass yield.* Acc Chem Res, **38** (2005), 202-207.

[31] J.C Elliot, *Structure and chemestry of the apatites and other calcium orthophosphates*, Amsterdam. Elsevier 1994

[32] Posner AS, Perloff A, Diorio AF, *Refinement of hydroxyapatite structure*. Acta Cryst, **11** (1958), 308-309.

[33] McDowell H, Gregory TM, Brown WE, *Solubility of* $Ca_5(PO_4)_3OH$ *in the system* $Ca(OH)_2$–H_3PO_4–H_2O *at 5, 15, 25, and 37°C*. J Res Natl Bur Stand A Phys Sci, **81A** (1977), 273–281.

[34] Featherstone JDB, Mayer I, Driessens FCM, Verbeeck RMH, Heijligers M, *Synthetic apatites containing Na, Mg, and* CO_3 *and their comparison with tooth enamel mineral*. Calcif Tissue Int, **35** (1983), 169–171.

[35] Bigi A, Gazzano M, Ripamonti A, Foresti E, Roveri N, *Thermal stability of cadmium–calcium hydroxyapatite solid solutions*. J Chem Soc Dalton Trans, **26** (1986), 241–244.

[36] Schroeder HE, *Formation and inhibition of dental calculus*, Ed. Has Huber (1969), Berne.

[37] Bodier-Houllé P, Steuer P, Voegel JC, Cuisinier FJC, *First experimental evidence for human dentine crystal formation involving conversion of octacalcium phosphate to hydroxyapatite.* Acta Crystallogr, **D54** (1998), 1377-1381.

[38] Šupová M, *Substituted hydroxyapatites for biomedical applications: A review*. Ceramics International, **41**(2015), 9203–9231.

[39] Mathew M, Brown WE, Schroeder LW, Dickens B, *Crystal structure of octacalcium bis (hydrogenphosphate) tetrakis (phosphate) pentahydrate,* $Ca_8(HPO_4)_2(PO_4)_4 \cdot 5H_2O$. J Cryst Spectrosc Res, **18** (1988), 235-250.

[40] Brown WE, Eidelman N, Tomzaic BB, *Octacalcium phosphate as a precursor in biomineral formation*. Adv Dent Res, **1** (1987), 306-313.

[41] Taves DR, *Similarity of octacalcium phosphate and hydroxyapatite structures.* Nature, **200** (1963), 1312-1313.

[42] Brown WE, *Octacalcium phosphate and hydroxyapatite: crystal structure of octacalcium phosphate.* Nature, **196** (1962), 1048-1050.

[43] Brown WE, Smith JP, Lehr JR, Frazier AW, *Crystallographic and chemical relations between octacalcium phosphate and hydroxyapatite*. Nature, **196** (1962), 1050-1054.

[44] Young RA, Brown WE, Nancollas GH, *Biological Mineralization and Demineralization.* Springer-Verlag; Berlin, (1982).

[45] Mathew M, Schroeder LW, Dickens B, Brown WE, *The crystal structure of* α-$Ca_2(PO_4)_2$. Acta Cryst, **B33** (1977), 1325-1333.

[46] Mackay AL, *A preliminary examination of the structure of* α-$Ca_3(PO_4)_2$. Acta Cryst, **6** (1953), 743-744.

[47] Dickens B, Schroeder LW, Brown WE, *Crystallographyc studies of the role of Mg as a stabilizing impurity in* β-$Ca_3(PO_4)_2$. J Solid State Chem, **10** (1974), 232-248.

[48] Yin X, Stott MJ, *α- and β-tricalcium phosphate: A density functional study*. Physical Rev, **68** (2003), 205205.

[49] Cheng PT, Grabher J, LeGeros RZ, *Effect of magnesium on calcium phosphate formation*. Magnesium, **7** (1988), 123-132.

[50] Moonga BS, Dempster DW, *Zinc is a potent inhibitor of osteoclastic bone resorption in vitro*. J Bone Miner Res, **10**(1995), 453–457.

[51] Fuierer TA, LoRe M, Puckett SA, Nancollas GH, *A mineralization adsorption and mobility study of hydroxyapatite surfaces in the presence of zinc and magnesium ions*. Langmuir, **10** (1994), 4721–4725.

[52] Kanzaki N, Onuma K, Treboux G, Tsutsumi S, Ito A, *Inhibitory effect of magnesium and zinc on crystallization kinetics of hydroxyapatite (0 0 0 1) face*. J Phys Chem B, **104** (2000), 4189–4194.

[53] Bigi A, Foresti E, Gandolfi M, Gazzano M, Roveri N, *Inhibiting effect of zinc on hydroxylapatite crystallization*. J Inorg Biochem, **58** (1995), 49–58.

[54] Miyaji F, Kono Y, Suyama Y, *Formation and structure of zinc-substituted calcium hydroxyapatite*. Mater Res Bull, **40** (2005), 209–220.

[55] Ren F, Xin R, Ge X, Leng Y, *Characterization and structural analysis of zinc substituted hydroxyapatites*. Acta Biomater, **5** (2009), 3141–3149.

[56] Li M, Xiao X, Liu R, Chen C, Huang L, *Structural characterization of zinc-substituted hydroxyapatite prepared by hydrothermal method*. J Mater Sci –Mater Med, **19** (2008), 797–803.

[57] Kalita SJ, Bhatt HA, *Nanocrystalline hydroxyapatite doped with magnesium and zinc: synthesis and characterization*, Mater Sci Eng C, **27** (2007), 837–848.

[58] Tang Y, Chappell HF, Dove MT, Reeder RJ, LeeYJ, *Zinc incorporation into hydroxyapatite.* Biomaterials, **30** (2009), 2864–2872.

[59] Miyaji F, Kono Y, Suyama Y, *Formation and structure of zinc-substituted calcium hydroxyapatite*. Mater Res Bull, **40** (2005), 209–220.

[60] Bigi A, Foresti E, Gandolfi M, Gazzano M, Roveri N, *Inhibiting effect of zinc on hydroxylapatite crystallization*. J Inorg Biochem, **58** (1995), 49–58.

[61] Boanini E, Gazzano M, Bigi A, I*onic substitutions in calcium phosphates synthesized at low temperature*. Acta Biomaterialia, **6** (2010), 1882-1894.

[62] Yeo S, Lee H, Jeong S, *Preparation of nanocomposite fibers for permanent antibacterial effect*. J Mater Sci, **38** (2003), 2143-2147.

[63] Chimentao R, Kirm I, Medina F, Rodrıguez X, Cesteros Y, Salagre P, Sueiras J, *Different morphologies of silver nanoparticles as catalysts for the selective oxidation of styrene in the gas phase*. Chem Commun, **4** (2004), 846-847.

[64] He B, Tan J, Liew K, Liu H, *Synthesis of size controlled Ag nanoparticle*. J Mol Catal A, **221** (2004), 221-126.

[65] Tran QH, Nguyen VQ, Le AT, *Silver nanoparticles: synthesis, properties, toxicology, applications and perspectives*. Adv Nat Sci: Nanosci Nanotechnol, **4** (2013), 1-20.

[66] Zomorodian K, Pourshahid S, Sadatsharifi A, Mehryar P, Pakshir K, Rahimi MJ, Monfared AA, *Biosynthesis and characterization of silver nanoparticles by Aspergillus species*, BioMed Research Int, **5** (2016), 1-6.

[67] Gurav AS, Kodas TT, Wang LM, Kauppinen EI, Joutsensaari J, *Generation of nanometer-size fullerene particles via vapor condensation*. Chem Phys Lett, **218** (1994), 304-308.

[68] Magnusson M, Deppert K, Malm J, Bovin J, Samuelson L, *Gold nanoparticles: production, reshaping, and thermal charging*. J Nanoparticle Res, **1** (1999), 243-251.

[69] Mafune F, Kohno J, Takeda Y, Kondow T, Sawabe H, *Formation and size control of silver nanoparticles by Laser Ablation in aqueous solution.* J PhysChem B, **104** (2000), 9111-9117.

[70] Compagnini G, Scalisi AA, Puglisi O, *Production of gold nanoparticles by laser ablation in liquid alkanes*. J Appl Phys, **94** (2003), 7874-7877.

[71] Chen YH, Yeh CS, *Laser ablation method: Use of surfactants to form the dispersed Ag nanoparticles.* Colloids Surf A: Physico Chem Eng Aspects, **197** (2002), 133-139.

[72] Khomutov G, Gubin S, *Interfacial synthesis of noble metal nanoparticles*. Mater Sci Eng C, **22** (2002), 141-146.

[73] Oliveira M, Ugarte D, Zanchet D, Zarbin A, *Influence of synthetic parameters on the size, structure, and stability of dodecanethiol-stabilized silver nanoparticles*. J Colloid Interface Sci, **292** (2005), 429-435.

[74] Egorova E, Revina A, *Synthesis of metallic nanoparticles in reverse micelles in the presence of quercetin.*Colloids Surf A: Physicochem Eng Aspects, **168** (2000), 87-96.

[75] Lee PC, Meisel D, *Adsorption and surface-enhanced Raman of dyes on silver and gold sols*. J Phys Chem, **86 (**1982), 3391–3395.

[76] Shirtcliffe N, Nickel U, Schneider S, *Reproducible preparation of silver sols with small particle size using borohydride reduction: for use as nuclei for preparation of larger particles.*J Colloid Interface Sci, **211** (1999), 122-129.

[77] Middleton E, Kandaswami C, *The flavonoids: advances in research since 1986*, J. B. Harborne, Ed.,Chapman& Hall, London, 1994

[78] Ricciuti L, Cardini M, *Flavonoidi:profilo farmacologico e terapeutico*, 2001.

[79] Wu T, He M, Zang X, Zhou Y, Qiu T, Pan S, Xu X, *A structure–activity relationship study of flavonoids as inhibitors of E. coli by membrane interaction effect*. Biochim Biophys Acta, **1828** (2013), 2751–2756.

[80] Wattel A, Kamel S, Mentaverri R, Lorget F, Prouillet C, Petit JP, Fardelonne P, Brazier M, *Potent inhibitory effect of naturally occurring flavonoids quercetin and kaempferol on in vitro osteoclastic bone resorption*. Biochem Pharmacol, **65** (2003), 35–42.

[81] Han QQ, Du Y, Yang PS, *The role of small molecules in bone regeneration*. Future Med Chem, **5** (2013), 1671–1684.

[82] Guo C, Hou CQ, Li XD, Xia X, Liu DX, Huang DY, Du SX, *Quercetin triggers apoptosis of lipopolysaccharide (LPS)-induced osteoclasts and inhibits bone resorption in RAW264.7 cells*. Cell Physiol Biochem, **30** (2012), 123–136.

[83] Wattel A, Kamel S, Prouillet C, Petit JP, Lorget F, Offord E, Brazier M, *Flavonoid quercetin decreases osteoclastic differentiation induced by RANKL via a mechanism involving NFkB and AP-1*. J Cell Biochem, **92** (2004), 285–295.

[84] Yamaguchi M, Weitzman MN, *Quercetin, a potent suppressor of NF-kB and Smad activation in osteoblasts*. Int J Mol Med, **28** (2011), 521–525.

[85] Mabry TJ, Markham KR, Tomas MB, *The Systematic Identification of Flavonoids.*Springer–Verlag, Berlin, 1970

[86] Pietta PG, *Flavonoids and natural products*. J Nat Prod, **63** (2000), 1035-1043.

[87] Inczedy J, *Analytical applications of complex equilibria*, Ellis Horwood Ltd., New York, 1976.

[88] Malesev D, Kunti V, I*nvestigation of metal–flavonoid chelates and the determination of flavonoids via metal–flavonoid complexing reactions*. J Serb Chem Soc, **10** (2007), 921-939.

[89] Heim KE, Tagliaferro AR, Bobilya DJ, *Flavonoid antioxidants: chemistry, metabolism and structure-activity relationships*. J Nutr Biochem, **10** (2003), 572-584.

[90] Liu X, Lin K, *Growth of highly oriented hydroxyapatite arrays tuned by quercetin*. Chemestry, **18** (2012), 5519–5523.

[91] Conrad JP, Merlin JC, Boudet AC, Vrielynch L, *Structural Study of Quercetin by Vibrational and Electronic Spectroscopies Combined with Semiempirical Calculations*, 1997.

[92] Borghetti GS, Carini JP, Honorato SB, Ayala AP, Moreira JCF, Bassani VL, *Physicochemical properties and thermal stability of quercetin hydrates in the solid state*. Thermochimica Acta, **539** (2012), 109-114.

[93] Forte L, Torricelli P, Boanini E, Gazzano M, Rubini K, Fini M, Bigi A, *Antioxidant and bone repair properties of quercetin-functionalized hydroxyapatite: An in vitro osteoblast–osteoclast–endothelial cell co-culture study.* Acta Biomaterialia, **32** (2016), 298-308.

[94] Ye W, Wang D, Zhang H, Zhou F, Liu W, *Electrochemical growth of flowerlike gold nanoparticles on polydopamine modified ITO glass for SERS application.* Electrochim Acta, **55** (2010), 2004-2009.

[95] Sureshkumar M, Lee PN, Lee CK, *Stepwise assembly of multimetallic nanoparticles via self-polymerized and polydopamine.* J Mater Chem, **21** (2011), 12316–12320.

[96] Zhang Z, Zhang J, Zhang B, Tang J, *Mussle-inspired functionalization of graphene for synthesizing Ag-polydopamine graphene nanosheets as antibacterial materials.*Nanoscale, **5** (2013), 118-123.

[97] Waite JH, *Surface chemistry: Mussel power.* Nat Mater, **7** (2008), 8-9.

[98] Hong S, Na YS, Choi S, Song IT, Kim WY, Lee H, *Non-Covalent Self-Assembly and Covalent Polymerization Co-Contribute to Polydopamine Formation.*Advanced Functional Materials, **22** (2012), 4711-4717

[99] Ham HO, Liu Z, Lau KHA, Lee H, Messersmith PB, *Facile DNA immobilization on surfaces through a catecholamine polymer*. Angewandte Chemie-International Edition, **50** (2011), 732–736.

[100] Lee H, Rho J, Messersmith PB, *Facile conjugation of biomolecules onto surfaces via mussel adhesive protein inspired coatings*. Adv Mat, **21** (2009), 431–434.

[101] Poh CK, Shi ZL, Lim TY, Neoh KG, Wang W, *The effect of VEGF functionalization of titanium on endothelial cells in vitro*. Biomaterials, **31** (2010), 1578-1585.

[102] Ryu J, Ku SH, Lee H, Park CB, *Mussel-inspired polydopamine coating as a universal route to hydroxyapatite crystallization.* Adv Funct Mater, **20** (2010), 2132−2139.

[103] Long Y, Wu J, Wang H, Zhang X, Zhao N, Xu J, *Rapid sintering of silver nanoparticles in an electrolyte solution at room temperature and its application to fabricate conductive silver films using polydopamine as adhesive layers*. J Mater Chem, **21** (2011), 4875-81.

[104] Wu J, Zhang L, Wang Y, Long Y, Gao H, Zhang X, Zhao N, Cai Y, Xu J,*Mussel-inspired chemistry for robust and surface-modifiable multilayer films.* Langmuir, **27** (2011), 13684-13691.

[105] Yang WJ, Neoh KG, Kang ET, Teo SLM, Rittschof D, *Stainless steel surfaces with thiol-terminatedhyperbranched polymers for functionalization*via *thiol-based chemistry*. Polymer Chemistry, **4** (2013), 3105-3115.

[106] Luo R, Tang L, Wang J, Zhao Y, Tu Q, Weng Y, Shen R, Huang N, *Improved immobilization of biomolecules to quinone-rich polydopamine for efficient surface functionalization*. Colloids Surf B, **106** (2013), 66-73.

[107] Ogaki R, Bennetsen DT, Bald I, Foss M, *Dopamine-assisted rapid fabrication of nanoscale protein arrays by colloidal lithography*. Langmuir, **28** (2012), 8594-8599.

[108] Liu Y, Ai K, Lu L, P*olydopamine and Its Derivative Materials: Synthesis and Promising Applications in Energy, Environmental, and Biomedical Fields.* Chem Rev, **9** (2014), 5057-5115.

[109] Herlem G, Lakard B, *Ab initio study of the electronic and structural properties of the crystalline polyethyleneimine polymer.* J Chemical Physics, **120** (2004), 9376-9382.

[110] Dick CR, Ham GE, *Characterization of polyethylenimine.* J Macromol Sci Chem, **A4** (1970), 1301-1314

[111] Godbey WT, Wu KK, Mikos AG, *Poly(ethylenimine) and its role in gene delivery*. J Control Release, **60** (1999), 149-160.

[112] Schenk R, Merz WA, Muhlbauer R, Russell RGG, Fleisch H, *Effect of twodiphosphonates on bone and cartilage growth and resorption in the tibialepiphysis and metaphysis of rats.* Calcif Tissue Res, **11** (1973), 196–214.

[113] Trechsel U, Stutzer A, Fleisch H, *Hypercalcemia induced with an arotinoid in thyroparathyroidectomized rats: new model to study bone resorption in vivo*. J Clin Invest, **80** (1987), 1679–86.

[114] Rasmusson L, Abthai J, *Bisphosphonate Associated Osteonecrosis of the Jaw: An Update on Pathophysiology, Risk Factors, and Treatment*. International Journal of Dentistry, **48** (2014), 1-9.

[115] Ebetino FF, Russell RGG, *Etidronate, Mechanism of action of etidronate and other bisphosphonate*. Rev Contemp Pharma, **9** (1998), 233-243.

[116] Russell RGG, Rogers MJ, *Bisphosphonate: from the laboratory to the clinic and back again*. Bone, **25** **(**1999), 97-106.

[117] Geddes A, D'sousa, Ebetino FH, *Bisphosphonate : structure activity relationship and therapeutic implication*. Bone Miner Res, **8** (1994), 265-306.

[118] Van Beek E, Lowik C, Oue I, Papapoulos S, *Dissociation of binding and antiresorptive properties of hydroxybisphosphonates by substitution of the hydroxyl with an amino group*. J Bone Miner Res, **11** (1996), 1492–1497.

[119] Ebetino FH, Emmerling P, Barnett B, Nancollas GH, *Differentiation of hydroxyapatite affinity of bisphosphonate analogs for mechanism of action studies*. J Bone Miner Res, **19** (2004), 157-163.

[120] Russell RGG, Watts NB, Ebetino FH, Rogers MJ, *Mechanisms of action of bisphosphonates: similarities and differences and their potential influence on clinical efficacy*. Osteoporos Int, **19** (2008), 733–759.

[121] Nancollas GH, Tang R, Phipps RJ, Henneman J, Gulde S, Wu W, Mangood A, Russell RGG, Ebetino FH, Novel insights into actions of bisphosphonates on bone: differences in interactions with hydroxyapatite. Bone, **38** (2006), 617–627.

[122] Lawson MA, Triffin JT, Ebetino FH, *Potential bone mineral binding differences among bisphosphonates can bedemonstrated by the use of hydroxyapatite column chromatography.*J Bone Miner Res, **20** (2005), 396-402.

[123] Ebetino FH, Barnett BL, Russell RGG, *A computational model delineates differences in hydroxyapatite binding affinities of bisphosphonate*. J Bone Miner Res, **20** (2005), S259.

[124] Deutsch E, Barnett BL, *Synthetic and structural aspects of technetium chemistry as related to nuclear medicine.Inorganic chemistry in biology and medicine.* American Chemistry Society, (1980), 103–119.

[125] Francis MD, Russell RG, Fleisch H. *Diphosphonates inhibit formation of calcium phosphate crystals in vitro and pathological calcification in vivo*. Science, **165** (1969), 1264–1266.

[126] Benedict JJ, *The physical chemistry of the disphosphonates - its relationship to their medical activity.* Donath A, Courvoisier B, editors. Symposium CEMO (Centre d'Etude des Maladies Ostéo-articulaires de Genève).

[127] Ebrahimpour A, Francis MD, *Bisphosphonate therapy in acute and chronic bone loss: physical chemical considerations in bisphosphonate-related therapies*. In: Bijvoet OLM, Fleisch HA, Canfield RE, Russell RGG, editors. Bisphosphonate on bones. Amsterdam: Elsevier. (1995) 125–36.

[128] Masarachia P, Weinreb M, Balena R, Rodan GA. *Comparison of the distribution of 3H-alendronate and 3H-etidronate in rat and mouse bones*. Bone, **19** (1996), 281–290.

[129] Azuma Y, Sato H, Oue Y, Okabe K, Ohta T, Tsuchimoto M, Kiyoki M, *Alendronate distributed on bone surfaces inhibits osteoclastic bone resorption in vitro and in experimental hypercalcemia models.* Bone, **16** (1995), 235–245.

[130] Amin D, Cornell SA, Gustafson SK, Needle SJ, Ullrich JW, Bilder GE, Perrone MH, *Bisphosphonates used for the treatment of bone disorders inhibit squalene synthase and cholesterol biosynthesis*. J Lipid Res, **33** (1992), 1657–1663.

[131] Amin D, Cornell SA, Perrone MH, Bilder GE, *1-hydroxy-3- (methylpentylamino)-propylidene-1,1-bisphosphonic acid as a potent inhibitor of squalene synthase*. Drug Res, **46** (1996), 759 –762.

[132] Luckman SP, Hughes DE, Coxon FP, Russell RGG, Rogers MJ, *Nitrogen-containing bisphosphonates inhibit the mevalonate pathway and prevent post-translational prenylation of GTP-binding proteins, including Ras.* J Bone Miner Res, **13** (1998), 581–589.

[133] Ridley AJ, Hall A, *The small GTP-binding protein Rho regulates the assembly of focal adhesions and actin stress fibers in response to growth factors.* Cell, **70** (1992), 389 –399.

[134] Ridley AJ, Paterson HF, Johnston CL, Diekmann D, Hall A, *The small GTP-binding protein, rac, regulates growth factor-induced membrane ruffling.* Cell, **70** (1992), 401– 410.

[135] Marshall C, *Protein prenylation: a mediator of protein-protein interactions.* Science, **259** (1993), 1865–1866.

[136] Zhang FL, Casey PJ, *Protein prenylation: molecular mechanisms and functional consequences.* Annu Rev Biochem, **65** (1996), 241–249.

[137] Foo KY, Hameed BH, *Insights into the modeling of adsorption isotherm systems*. Chem Eng J, **156** (2010), 2-10.

[138] Kumar KV, Sivanesan S, *Sorption isotherm for safranin onto rice husk: comparison of linear and non-linear methods*. Dyes Pigments, **72** (2007), 130–133.

[139] Limousin G, Gaudet JP, Charlet L, Szenknect S, Barthes V, Krimissa M, *Sorption isotherms: a review on physical bases, modeling and measurement*. Appl Geochem, **22** (2007), 249–275.

[140] Freundlich HMF, *Over the adsorption in solution*. J Phys Chem, **57** (1906), 385-471.

[141] Zeldowitsch J, *Adsorption site energy distribution*. Acta Phys Chim URSS, **1** (1934), 961–973.

[142] Haghseresht F, Lu G, *Adsorption characteristics of phenolic compounds onto coal-reject-derived adsorbents*. Energy Fuels, **12** (1998), 1100–1107.

[143] Sips R, *Combined form of Langmuir and Freundlich equations*. J ChemPhys, **16** (1948), 490-495.

[144] Fogueri LR, Singh S, *Smart polymers for controlled delivery of proteins and peptides: a review of patents Recent Pat.* Drug Deliv Formul, **3** (2009), 40–48.

[145] Ji W, Wang H, Jeroen JJP, Van de Beuken, Yang F, Walboomers F, Leeuwenbourgh S, Jansen JA, *Local delivery of small and large biomolecules in craniomaxillofacial bone*. Adv Drug Delivery Rev, **64** (2012), 1152-1164.

[146] Sharon JL, PuleoDA, *Immobilization of glycoproteins, such as VEGF, on biodegradable substrates*. Acta Biomater, **4** (2008), 1016–1023.

[147] Lin CC, Metters AT, *Hydrogels in controlled release formulations: network design and mathematical modeling,* Adv Drug Deliv Rev, **58** (2006), 1379–1408.

[148] Chen FM, Zhang M, Wu ZF, *Toward delivery of multiple growth factors in tissue engineering.* Biomaterials, **31** (2010), 6279–6308.

[149] Biondi M, Ungaro F, Quaglia F, Netti PA, *Controlled drug delivery in tissue engineering.* Adv Drug Deliv Rev, **60** (2008), 229–242.

[150] Barroug A, Kuhn LT, Gerstenfeld LC, Glimcher MJ, *Interactions of cisplatin with calcium phosphate nanoparticles: in vitro controlled adsorption and release*. J Orthop Res, **22** (2004)**,** 703-708.

[151] Bohner M, Lemaître J, Van Landuyt P, Zambelli PY, Merkle HP, Gander B, *Gentamicin-loaded hydraulic calcium phosphate bone cement as antibiotic delivery system*. Journal of Pharmaceutical Sciences, **86** (1997), 565-572.

[152] Hamanishi C, Kitamoto K, Tanaka S, Otsuka M, Doi Y, Kitahashi T, *A self-setting TTCP-DCPD apatite cement for release of vancomycin*, Journal of Biomedical Materials Research, **33** (1998), 139-143.

[153] Autefage H, Briand-Mésange F, Cazalbou S, Drouet C, Fourmy D, Gonçalvès S, Salles JP, Combes C, Swider P, Rey C, *Adsorption and release of BMP-2 on nanocrystalline apatite-coated and uncoated hydroxyapatite/β-tricalcium phosphate porous ceramics*, Journal of Biomedical Materials Research Part B: Applied Biomaterials, **91B** (2009 a), 706-715.

[154] Lind M, OvergaardS, Soballe K, NguyenT,OngpipattanakulB, BungerC, *Transforming growth factor-beta 1 enhances bone healing tounloaded tricalcium phosphate coated implants: an experimental study in dogs*. J Orthop Res, **14** (1996), 343–350.

[155] Coleman R, *Zoledronic acid*. Expert Opinion on Drug Safety, **10** (2011)**,** 133-145.

[156] Coleman RE, *Risks and benefits of bisphosphonates*. Br J Cancer, **98** (2008), 1736-1740.

[157] Ochiuz, L, Stoleriu I, Moscalu M, Popa G, Adrian S, Popovici I, *Investigations on the in vitro release mechanism of sodium alendronate from hydrophilic matrix tablets.*Farmacia, **58** (2010), 795-805.

[158] Balas F, Manzano M, Horcajada P, Vallet-Regí M, *Confinement and controlled release of bisphosphonates on ordered mesoporous silica-based materials*. Journal of the American Chemical Society, **128** (2006), 8116-8117.

[159] Shi X, *Enhancing alendronate release from a novel PLGA/hydroxyapatite microspheric system for bone repairing applications*. Pharmaceutical research, **26** (2009), 422-430.

[160] Palazzo B, Iafisco M, Laforgia M, Margiotta N, Natile G, Bianchi CL, Walsh D, Mann S, Roveri N, *Biomimetic Hydroxyapatite-Drug Nanocrystals as Potential Bone Substitutes with Antitumor Drug Delivery Properties*. Adv Func Mater, **17** (2007), 2180-2188.

[161] Hijon N, Cabanas MV, Pena J, Vallet-Regi M, *Dip coated silicon-substituted hydroxyapatite films.* Acta Biomater, **2** (2006), 567–574.

[162] Thian ES, Huang J, Best SM, Barber ZH, Bonfield W, *Silicon-substituted hydroxyapatite: the next generation of bioactive coatings*. Mater Sci Eng C, **27** (2007), 251-256.

[163] Xue W, Hosick HL, Bandyopadhyay A, Bose S, Ding C, Luk KDK, Cheung KMC, Lu WW, *Preparation and cell-materials interactions of plasma sprayed strontium-containing hydroxyapatite coating*. Surf Coat Technol, **201 (**2007), 4685-4693.

[164] Socol G, Torricelli P, Bracci B, Iliescu M, Miroiu F, Bigi A, Werckmann, Mihailescu IN, *Biocompatible nanocrystalline octacalcium phosphate thin films obtained by pulsed laser deposition.* Biomaterials, **25** (2004), 2539-2545.

[165] Chiesa R, Sandrini E, Santin M, Rondelli G, Cigada A, *Osteointegration of titanium and its alloys by anodic spark deposition and other electrochemical techniques*. J Appl Biomater Biomech, **1** (2003), 91–107.

[166] Kokubo T, Kushitani H, Sakka S, Kitsugi T, Yamamuro T, *Solutions able to reproduce invivo surface-structure changes in bioactive glass-ceramic A-W*^{3}. J Biomed Mater Res, **24** (1990), 721–734.

[167] Mròz W, Jedynski M, Prokopiuk A, Slosarczyk A, Paszkiewic Z, *Characterization of calcium phosphate coatings doped with Mg, deposited by pulsed laser deposition technique using ArF excimer laser*. Micron, **40** (2009), 140-142.

[168] Yang Y, Kim KH, Ong JL, *A review on calcium phosphate coatings produced using a sputtering process—an alternative to plasma spraying.* Biomaterials, **263** (2005), 27–37.

[169] Luo ZS, Cui FZ, Li WZ, *Low-temperature crystallization of calcium phosphate coatings synthesized by ion-beam-assisted deposition*. J Biomed Mater Res, **46** (1999), 80–86.

[170] Wei M, Ruys AJ, Milthorpe BK, Sorrell CC, *Solution ripening of hydroxyapatite nanoparticles: effects on electrophoretic deposition*. J Biomed Mater Res, **45** (1999), 11–19.

[171] Ishizawa H, Ogino M, *Formation and characterization of anodic titanium oxide films containing Ca and P*. J Biomed Mater Res, **34** (1997), 15–20.

[172] Bigi A, Boanini E, Bracci B, Facchini A, Panzavolta S, Segatti F, Sturba L, *Nanocrystalline hydroxyapatite coatings on titanium: a new fast biomimetic method*. Biomaterials, **26** (2005), 4085-4089.

[173] Chrisey DB, Hubler GK editors, *Pulsed laser deposition of thin films* Wiley (1994), New York.

[174] Mihailescu IN, Gyorgy E, *Pulsed laser deposition: an overview*. In: T. Asakura ed. *Trends in optics and photonics.* Springer series in optical science.Springer-Verlag **201** (1999), Berlin.

[175] Bauerle D, *Laser processing and chemistry*. Springer (1996), Berlin.

[176] McGill RA, Chrisey DB, 2000.*Method of producing a film coating by matrix assisted pulsed laser deposition*. Patent 6025036 A

[177] Axente E, Sima F, Ristoscu C, Mihailescu N, Mihailescu IN, Biopolymer thin films synthesized by advanced pulsed laser techniques. Recent advances in biopolymer. Ed Perveen, 2009.

[178] Stresing V, Daubiné F, Benzaid I, Mönkkönen H, Clézardin P, *Bisphosphonates in cancer therapy.* Cancer Lett, **257** (2007), 16–35.

[179] Favia G, Pilolli GP, Maiorano E, *Histologic and histomorphometric featuresof bisphosphonate-related osteonecrosis of the jaws: an analysis of 31 cases with confocal laser scanning microscopy.* Bone, **45** (2009), 406–413.

[180] Rizzoli R, Åkesson K, Bouxsein M, Kanis JA, Napoli N, Papapoulos S, Reginster JY, Cooper C, *Subtrochanteric fractures after long-term treatment with bisphosphonates: a European society on clinical and economic aspects of osteoporosis and osteoarthritis, and international osteoporosis foundation working group report*. Osteoporos Int, **22** (2011), 373–390.

[181] Williams RJ, Spencer JPE, Rice-Evans C, *Flavonoids: antioxidants or signalling molecules?* Free Radic Biol Med, **36** (2004), 838-849.

[182] Xing N, Chen Y, Mitchell SH, Young CYF, *Quercetin inhibits the expression and function of the androgen receptor in LNCaP prostate cancer cells.* Carcinogenesis, **22** (2001), 409-414.

[183] Slawson RM, Trevors JT, Lee H, *Silver accumulation and resistance in Pseudomonas stutzeri.* Arch Microbiol, **158** (1992), 398–404.

[184] Zhao GJ, Stevens SE, *Multiple parameters for the comprehensive evaluation of the susceptibility of Escherichia coli to the silver ion.* Biometals, **11** (1998), 27–32.

[185] Boanini E, Torricelli P, Gazzano M, Giardino R, Bigi A, *Nanocomposites of hydroxyapatite with aspartic acid and glutamic acid and their interaction with osteoblast-like cells.* Biomaterials, **27** (2006), 4428–4433.

[186] Forte L, Sarda S, Boanini E, Combes C, Gazzano M, Brouillet F, Bigi A, *Hydroxyapatite functionalization as a tool to modulate adsorption and release of risedronate,* manuscript in preparation.

[187] Boanini E, Torricelli P, Gazzano M, Giardino R, Bigi A, *Alendronate-hydroxyapatite nanocomposites and their interaction with osteoclasts and osteoblast-like cells*. Biomaterials, **29** (2008), 790–796.

[188] Bigi A, Boanini E, Borghi M, Cojazzi G, Panzavolta S, Roveri N, *Synthesis and hydrolysis of octacalcium phosphate: effect of sodium polyacrylate*. Journal of Inorganic Biochemistry, **7**5 (1999), 145–151.

[189] Forte L, Torricelli P, Boanini E, Gazzano M, Fini M, Bigi A, *Antiresorptive and anti-angiogenetic octacalcium phosphate functionalized with bisphosphonates: An in vitro tri-culture study.* Acta Biomaterialia (2017) doi: http://dx.doi.org/10.1016/j.actbio.2017.02.040

[190] Bigi A, Boanini E, Botter R, Panzavolta S, Rubini K, *α-tricalcium phosphate hydrolysis to octacalcium phosphate: effect of sodium polyacrylate.* Biomaterials, **23 (**2002), 1849–1854.

[191] Kuljanin J, Jankovic I, Nedeljkovic J, Prstojevic D, Marinkovic V, *Spectrophotometric determination of alendronate in pharmaceutical formulations via complex formation with Fe(III) ions.* J Pharm Biomed Anal, **28** (2002), 1215-1220.

[192] Klug HP, Alexander LE, *X-ray diffraction procedures for polycrystalline and amorphous materials*, Wiley–Interscience (1974), New York.

[193] Gülçin I, *Antioxidant and antiradical activities of l-carnitine*. Life Sci, **78** (2006), 803–811.

[194] Hernandez-Montelongo J, Gallach D, Naveas N, Torres-Costa V, Climent- Font A, García-Ruiz JP, Manso-Silvan M, *Calcium phosphate/porous silicon biocomposites prepared by cyclic deposition methods: spin coating vs electrochemical activation*. Mater Sci Eng C, **34** (2014), 245–251.

[195] Wang W, Sun C, Mao L, Ma P, Liu F, Yang J, Gao Y, *The biological activities, chemical stabilities, metabolism and delivery system of quercetin: a review*. Trends in Food Science and Technology, **56** (2016), 21-38.

[196] Berlier G, Gastaldi L, Ugazio E, Miletto I, Iliade P, Sapino S, *Stabilization of quercetin flavonoid in MCM-41 mesoporous silica: positive effect of surface functionalization.* J Colloid Interface Sci, **393** (2013), 109–118.

[197] Ranilla LG, Genovese MI, Lajolo F M, *Effect of different cooking conditions on phenolic compounds and antioxidant capacity of some selected Brazilian bean (Phaseolus vulgaris L.) cultivars.* Journal of Agricultural and Food Chemistry, **57** (2009), 5734-5742.

[198] Makris DP, Rossiter JT, *Domestic processing of onion bulbs (Allium cepa) and asparagus spears (Asparagus officinalis): Effect on flavonol content and antioxidant status.* Journal of Agricultural and Food Chemistry, **49** (2001), 3216-3222.

[199] Makris DP, Rossiter JT, *Heat-induced, metal-catalyzed oxidative degradation of quercetin and rutin (quercetin 3-O-rhamnosylglucoside) in aqueous model systems.* Journal of Agricultural and Food Chemistry, **48** (2000), 3830-3838.

[200] Igual M, García-Martínez E, Camacho MM, Martínez-Navarrete N, *Changes in flavonoid content of grapefruit juice caused by thermal treatment and storage.* Innovative Food Science & Emerging Technologies, **12** (2011), 153-162.

[201] Buchner N, Krumbein A, Rohn S, Kroh LW, *Effect of thermal processing on the flavonols rutin and quercetin.* Rapid Communications in Mass Spectrometry, **20** (2006), 3229-3235.

[202] Moon YJ, Wang L, DiCenzo R, Morris ME, *Quercetin pharmacokinetics in humans.* Biopharmaceutics & Drug Disposition, **29** (2008), 205-217.

[203] Pekal A, Biesaga M, Pyrzynska K, *Interaction of quercetin with copper ions: Complexation, oxidation and reactivity towards radicals.* Biometals, **24** (2011), 41-49.

[204] Chen W, Sun S, Liang Y, Song J, *Antioxidant property of quercetin-Cr (III) complex: The role of Cr (III) ion*. Journal of Molecular Structure, **918** (2009), 194-197.

[205] Dehghan G, Khoshkam Z, Tin (II) quercetin complex: *Synthesis, spectral characterization and antioxidant activity*. Food Chemistry, **131** (2012), 422-426.

[206] Boanini E, Gazzano M, Rubini K, Bigi A, *Composite Nanocrystals provide new insight on alendronate interaction with hydroxyapatite structure.* Adv Mater, **19** (2007), 2499–2502. [207] Jasmina M,

Dimitri C, Markovi L, *Interpretation of the IR and Raman spectra of morin by density functional theory and comparative analysis*. Vibrational Spectroscopy, **64** (2013), 1-9

[208] Jasmina M, Dimitri C, Markovi L, *Electronic and infrared vibrational analysis of cyanidin–quercetin copigment complex*. Spectrochimica Acta Part A, **62** (2005), 673-680.

[209] Xu J, Butler IS, Gilson DFR, *FT-Raman and high-pressure infrared spectroscopic studies of dicalcium phosphate dihydrate ($CaHPO_4{\cdot}2H_2O$) and anhydrous dicalcium phosphate ($CaHPO_4$).* Spectrochimica Acta Part A, **55** (1999), 2801 – 2809.

[210] Boanini E, Torricelli P, Gazzano M, Fini M, Bigi A, *Crystalline calcium alendronate obtained by octacalcium phosphate digestion: A new chance for local treatment of bone loss diseases?* Adv Mater, **25** (2013), 4605-4611.

[211] Lee WK, Ko JS, Kim HM, *Effect of Electrostatic Interaction on the Adsorption of Globular Proteins on Octacalcium Phosphate Crystal Film.* J Colloid Interf Sci, **246** (2002), 70-77.

[212] Liu D, Kramer SA, Huxford-Phillips RC, Wang S, Della Rocca J, Lin W, *Coercing bisphosphonates to kill cancer cells with nanoscale coordination Polymers*. Polymers Chem Commun, **48** (2012), 2668-2670.

[213] Boanini E, Torricelli P, Gazzano M, Fini M, Bigi A, *The effect of zoledronate-hydroxyapatite nanocomposites on osteoclasts and osteoblast-like cells in vitro.* Biomaterials, **33** (2012), 722-730.

[214] Boanini E, Gazzano M, Bigi A, *Time course of zoledronate interaction with hydroxyapatite nanocrystals.* J Phys Chem C, **116** (2012), 15812-15818.

[215] Brown WE, Mathew M, Tung MS, *Crystal chemistry of octacalcium phosphate*. Crystal growth Characterization, **4** (1981), 59-87

[216] Boanini E, Gazzano M, Rubini K, Bigi A, *Collapsed Octacalcium phosphate stabilized by ionic substitutions.* Cryst Growth Des, **10** (2010), 3612-3617.

[217] Josse S, Faucheux C, Soueidan A, Grimandi G, Massiot D, Alonso B, Laïb S, Pilet P, Gauthier O, Daculsi G, Guicheux JJ, Bujoli B, Bouler JM, *Novel biomaterials for bisphosphonate delivery.* Biomaterials, **26** (2005), 2073-2080.

[218] Roussiere H, Fayon F, Alonso B, Rouillon T, Schnitzler V, Verron E, Guicheux J, Petit M, Massiot M, Janvier J, Bouler JM, Bujoli B, *Reaction of zoledronate with beta-tricalcium phosphate, for the design of potential drug device combined systems.* Chem Mater, **20** (2008), 182-191.

[219] Bigi A, Boanini E, Capuccini C, Fini M, Mihailescu IN, Ristoscu C, Sima F, Torricelli P, *Biofunctional alendronate-Hydroxyapatite thin films deposited by Matrix Assisted Pulsed Laser Evaporation* . Biomaterials, **30** (2009), 6168-6177.

[220] Verron E, Khairoun I, Guicheux J, Bouler JM, *Calcium phosphate biomaterials as bone drug delivery systems: a review.* Drug Discov Today, **15** (2010), 547–552.

[221] Verron E, Gauthier O, Janvier P, Pilet P, Lesoeur J, Bujoli B, Guicheux J, Bouler JM, *In vivo bone augmentation in an osteoporotic environment using bisphosphonate-loaded calcium deficient apatite.* Biomaterials, **31** (2010), 7776–7784.

[222] Panzavolta S, Torricelli P, Bracci B, Fini M, Bigi A, *Functionalization of biomimetic calcium phosphate bone cements with alendronate.* J Inorg Biochem, **104** (2010), 1099–1106.

[223] Errassifi F, Sarda S, Barroug A, Legrouri A, Sfihi H, Rey C, *Infrared, Raman and NMR investigations of risedronate adsorption on nanocrystalline apatites.* Journal of Colloid and Interface Science, **420** (2014), 101–111.

[224] Pascaud P, Gras P, Coppel Y, Rey C, Sarda S, *Interaction between a bisphosphonate, tiludronate, and biomimetic nanocrystalline apatites.* Langmuir, **29 (**2013), 2224-2232.

[225] Pascaud P, Errassifi F, Brouillet F, Sarda S, Barroug A, Legrouri A, Rey C, *Adsorption on apatitic calcium phosphates for drug delivery: interaction with bisphosphonate molecules.* Journal of Materials Science: Materials in Medicine, **25** (2014), 2373-2381.

[226] Eichert, D. Drouet C, Sfihi H, Rey C, Combes C, *Nanocrystalline apatite-based biomaterials: synthesis, processing and characterization*, Biomaterials Research Advances, (2008), 93-143.

[227] Kauppinen JK, Moffatt DJ, Mantsch HH, Cameron DG, *Fourier self-deconvolution—a method for resolving intrinsically overlapped bands.* Appl Spectrosc, **35** (1981), 271–276.

[228] Rui-Qi S, Helmut C, *Mesocrystals—Ordered Nanoparticle Superstructures.* Adv Mat, **22** (2010), 1301–1330.

[229] Song RQ, *Nonclassical Crystals: Crystallographically Ordered Nanocrystal Superstructures.* Elsevier 2016.

[230] Fuzeng Ren, Renlong Xin, Xiang Ge, Yang Leng, *Characterization and structural analysis of zinc-substituted hydroxyapatites.* Acta Biomaterialia, **5** (2009), 3141–3149.

[231] Al-Kattan A, Errassifi F, Sautereau AM, Sarda S, Dufour P, Barroug A, Dos Santos I, Combes C, Grossin D, Rey C, Drouet C, *Medical Potentialities of Biomimetic Apatites through Adsorption, Ionic Substitution, and Mineral/Organic Associations: Three Illustrative Examples.* Advanced Engineering Materials, **12** (2010), B224-B233.

[232] Penel G, Leroy G, Rey C, Bres E, *MicroRaman spectral study of the PO4 and CO3 vibrational modes in synthetic and biological apatites.* Calcif Tissue Int, **63** (1998), 475-81.

[233] Costa P, Sousa Lobo JM, *Modeling and comparison of dissolution profiles*. European Journal of Pharmaceutical Sciences, **13** (2001), 123–133.

[234] Fatnassi M, Jacquart S, Brouillet F, Rey C, Combes C, Girot Fullana S, *Optimization of spray-dried hyaluronic acid microspheres to formulate drug-loaded bone substitute materials.* Powder Technology, **255** (2014), 44–51.

[235] Chaloupka K, Malam Y, Seifalian AM, *Nanosilver as a new generation of nanoproduct in biomedical applications*. Trends in Biotechnology, **28** (2010), 580–588.

[236] Ko E, Yang K, Shin J, Cho SW, *Polydopamine-Assisted Osteoinductive Peptide Immobilization of Polymer Scaffolds for Enhanced Bone Regeneration by Human Adipose-Derived Stem Cells.* Biomacromolecules, **14** (2013), 3202−3213.

[237] Sileika TS, Kim HD, Maniak P,. Messersmith PB, *Antibacterial Performance of Polydopamine-Modified Polymer Surfaces Containing Passive and Active Components.* ACS Appl Mater Interfaces, **3** (2011), 4602–4610.

[238] Boanini E, Torricelli P, Gazzano M, Fini M, Bigi A, *The effect of alendronate doped calcium phosphates on bone cells activity.* Bone, **51** (2012), 944–952.

[239] Goriainov V, Cook R, Latham JM, Dunlop DG, Oreffo ROC, *Bone and metal: an orthopaedic perspective on osseointegration of metals*. Acta Biomater, **10** (2014), 4043–4057.

[240] Webster TJ, *Nanostructured Materials*. Academic Press, New York, Ying JY (Ed.) 2001, 125–166.

[241] Surmenev RA, Surmeneva MA, Ivanova AA, *Significance of calcium phosphate coatings for the enhancement of new bone osteogenesis—a review.* Acta Biomater, **10** (2014), 557–559.

[242] Sharma S, Verma A, Teja BV, Pandey G, Mittapelly N, Trivedi R, Mishra PR, *An insight into functionalized calcium based inorganic nanomaterials inbiomedicine: trends and transitions.* Colloid Surf B-Biointerfaces, **133** (2015), 120–139.

[243] Fowler BO, Markovi´c M, Brown WE, *Octacalcium phosphate. Infrared and raman vibrational spectra.* Chem Mater, **5** (1993), 1417–1423.

[244] Rufino Bezerra Neto J, de Lima Neto P, Adilson Matos Sales F, Eleto daSilva E, Orlando Ladeira L, Nogueira Freire V, Wagner Santos Caetano E, *Phosphate group vibrational signatures of the osteoporosis drug alendronate.* J Raman Spectrosc, **45** (2014), 801–806.

[245] Brenner GS, Ostovic D, *Use of bisphosphonic acids for the treatment of calcium metabolism disorders.* EP 0449405.A2, 1991.

[246] Boanini E, Torricelli P, Forte L, Pagani S, Mihailescu N, Ristoscu C, Mihailescu IN, Bigi A, *Antiresorption implant coatings based on calcium alendronate andoctacalcium phosphate deposited by matrix assisted pulsed laserevaporation.*Colloids and Surfaces B: Biointerfaces, **136** (2015), 449-456.